Cover Page

Universiteit Leiden

The handle http://hdl.handle.net/1887/38734 holds various files of this Leiden University dissertation

Author: López Gonzaga, Noel
Title: The structure of the dusty cores of active galactic nuclei
Issue Date: 2016-04-12

The structure of the dusty cores of active galactic nuclei

Noel López Gonzaga

The structure of the dusty cores of active galactic nuclei

Proefschrift

ter verkrijging van
de graad van Doctor aan de Universiteit Leiden,
op gezag van de Rector Magnificus prof. mr. C. J. J. M Stolker,
volgens besluit van het College voor Promoties
te verdedigen op dinsdag 12 april 2016
klokke 13.45 uur

door

Noel López Gonzaga

geboren op 11 july 1986
te Nezahualcoyotl, México

PROMOTOR: Prof. dr. W. Jaffe

CO-PROMOTOR: Prof. dr. K. Meisenheimer   Max Planck Institute for Astronomy

OVERIGE LEDEN: Prof. dr H. Rottgering
                 Prof. dr B. Brandl
                 Dr. E. M. Rossi
                 Prof. dr R. Morganti   Rijksuniversiteit Groningen
                 Prof. dr R. Petrov   University of Nice-Sophia Antipolis

To my beloved wife
and to my parents.

I

Contents

<div align="right">

CHAPTER 1

INTRODUCTION

</div>

1.1.   A bit of history.

The discovery of Active Galactic Nucleus (AGN) in the cores of many Galaxies occurred early in the twentieth century, when Fath [1909] analyzed the photographic spectra of several 'spiral nebulae' and found that some of the objects in his sample, such as NGC 1068, showed high excitation lines and some peculiar OIII/H$_\beta$ ratios which are not tipically observed in stars. Similar findings or confirmations were later reported by Slipher [1917].

Years later, the systematic study of galaxies with nuclear emission lines began with the work of Seyfert [1943]. Carl K. Seyfert obtained spectrograms of galaxies with nearly point-like nuclei showing emission lines superimposed on solar-type spectra. The emission-line profiles differed from line to line and from object to object, but several patterns emerged, that were to prove typical of this class of galaxies. Firstly, all showed high excitation lines in their spectra. Secondly, several showed very broad permitted Hydrogen lines with widths that correspond to speeds of $\approx 8{,}500$ km/s. And thirdly, several objects showed spectra with less broad forbidden lines (with widths corresponding to ≈ 3000 km/s) which matched the cores of hydrogen lines. Galaxies with high excitation nuclear emission lines are now called 'Seyfert galaxies'.

The next major advance for the study of AGNs was triggered by the developments of radio astronomy. Jansky [1933] conducted a study at $\lambda = 14.6$ m and concluded that significant radio emission came from the entire disk of the Milky Way, being strongest in the direction of the Galactic center. Reber [1944] additionally noted that the ratio of radio radiation to optical light was significantly larger for the Milky Way than the sun, suggesting a different mechanism for the emission at the nucleus of the Milky Way.

Years later, Matthews & Sandage [1963] and Schmidt [1963] reported observations of 3C 48 and 3C 273, respectively. These objects showed broad emission lines at unfamiliar wavelengths that could not be identified with known objects. Photometry showed rapid variability changes and an excess of ultraviolet (UV) emission compared with normal stars. Such objects came to be known as quasi-stellar radio sources (QSRS), quasi-stellar sources (QSS), or quasars. The observed similarities between Seyfert galaxies and QSOs suggested a common physical phenomenon. The discovery of the quasar 3C 273 at a redshift $z = 0.16$ implied an enormous luminosity for this object. The large redshifts of QSOs immediately made them potential tools for the study of cosmological questions.

From that time, astronomers have raised questions about the nature of the energy source, the nature of the continuum source and emission-line regions, and the factors that produce an AGN in some galaxies and not others.

1.2.   The unified model of AGNs

Several explanations for the observed properties of the Active Galaxies were postulated in early years. Woltjer [1959] postulated a separate region of fast moving, possibly gravitationally bound gas to produce the broad Balmer line wings of Seyfert galaxies. The picture of broad lines from a small region of dense, fast moving clouds (Broad Line Region or BLR) and narrow lines from a larger region of slower moving, less dense clouds (Narrow Line Region or NLR) found support from photoionization models [Shields, 1974].

As for the energy source, explanations including a chain reaction of supernovae in the galactic nucleus [Burbidge, 1961], collisions and tidal encounters in dense star clusters [Spitzer & Saslaw, 1966], and starburst models [Terlevich & Melnick, 1985] were proposed in the early years. But the most accepted and current explanation for the heating engine of AGNs comes from gravitational energy released during accretion onto a Super Massive Black Hole (SMBH) [e.g. Salpeter, 1964; Zel'dovich, 1964]. The explanation for the quasar energy production involved some kind of turbulent transport of angular momentum, allowing the matter to move closer to the hole, which would grow in mass during the accretion process. The thermal radiation expected in a disk of gas orbiting a black hole would naturally lead to photoionization and broad line emission. The radio emission arises from magnetic and particle acceleration that we still partially understand.

Observations of AGNs showed a diversity of spectral features that could be explained by using different physical components for every object. But despite their differences, some classes of AGNs showed unexpected similarities. This was most dramatically demonstrated by the detection of polarized broad lines in 3C 234 [Antonucci, 1984] and NGC 1068 [Antonucci & Miller, 1985]. The polarized spectra, most probably caused by electron scattering, revealed the existence of a broad line region (BLR) in objects with dominating narrow lines in their spectra. In order to find a simplified explanation for the diversity of observed spectra for AGNs, about 20 years ago Antonucci [1993]; Urry & Padovani [1995] proposed a unification scheme. In such unification scheme, all AGNs should share the same properties, which means they all should have a similar heating engine, but their observed differences, such as the presence or absence of broad emission lines, are determined by obscuration effects.
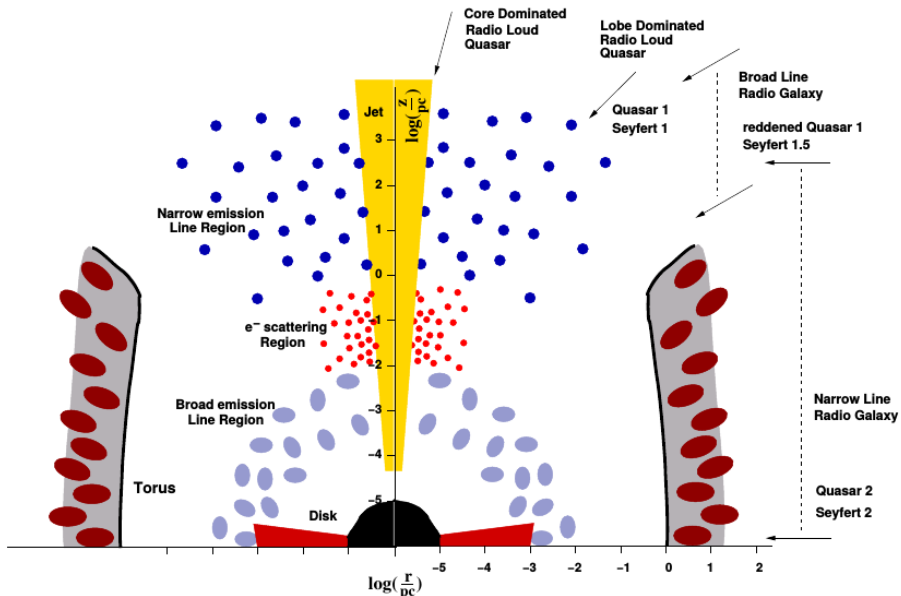
Figure 1.1: *A sketch of the cylindrically symmetric AGN according to Zier & Biermann [2002]. The cut shows the r-z-plane, both axes logarithmically scaled to 1 pc.*

Although there are some exceptions, the standard model states that the nuclear environment of an AGN includes the following components:

- **The super massive black hole (SMBH) and the accretion disk**. The strong gravity around the central black hole attracts matter, some of which finally disappears into the black hole. The enormous release of gravitating energy from the accretion process is emitted at optical/UV/X-ray wavelengths generating the famous Big Blue Bump (BBB) characteristic of AGNs

- **Relativistic jet.** A jet is a phenomenon in astrophysics, where particles are accelerated to speeds almost as great as the speed of light and form a stream typically divided in two narrow beams along the axis of rotation of the black hole. The highly beamed stream of matter propagates from the vicinity of the black hole out to parsec, kiloparsec and, in some objects, megaparsec distances. Because the medium in the accretion disc is highly ionized, the charged particles that are accelerated along the jet (due to magnetic fields) produce synchrotron radiation. The trapped magnetic field is capable in the accretion process to ultimatly give rise to the radio jets.

- **The Broad Line Region (BLR).** Surrounding the accretion disc, there is a region composed of high density ($\sim 10^{10}\,\mathrm{cm}^{-3}$) and highly ionized gravitationally bounded gas clouds with a column density of $\sim 10^{23}\,\mathrm{cm}^{-2}$. Due to their

proximity to the accretion disk, the clouds have typical velocities of order of $3000\,\mathrm{km\,s^{-1}}$ and it is reflected in the observed widths of the emitted emission lines. Because of the high density, forbidden lines are weak or absent.

- **The dusty environment.** At a few tenths of a parsec the strength of the radiation from the central engine drops down sufficiently that the dust can survive. The dust grains absorb the optical/UV radiation produced by the accretion disc and then re-emit the energy at infrared wavelengths, producing the typical observed infrared bumps in the spectral energy distributions (SEDs) of AGNs, which accounts for roughly half of the bolometric luminosity. Additionally, because the dust acts as an obscuring entity in the optical/UV regime, the dusty environment plays a significant role in the classification of AGNs.

- **Narrow Line Region (NLR).** Outside of the broad line region and extending out to a few parsecs, we find a region composed of clouds with low column density ($\sim 10^{20}\,\mathrm{cm^{-2}}$) and with a particle density of about 10^4 per $\mathrm{cm^{-3}}$. The observed spectrum of this component includes intense forbidden lines, because of the low densities. These lines shift the cooling balance in such a way that the semi-forbidden and permitted lines are relatively weaker. Another group of lines that are predicted to be intense in the innermost part of this region are coronal lines, produced by fine-structure transitions and observed mostly in the infrared.

1.2.1. The AGN family

Although many subdivisions exist, the primary classification of AGNs is based on the extent to which the nuclear region is visible. The current classification of AGN includes a diverse number of sub-groups, but the typical division for the sub-groups can be summarized as follows:

1.2.1.1. Type 1 AGNs

The spectra of Type 1 objects show broad ($1000-20{,}000\,\mathrm{km\,s^{-1}}$) permitted and semi forbidden emission lines and a bright, non-stellar, central point source visible at all wavelengths. Almost all low to intermediate luminosity type 1 AGNs show strong, high ionization narrow emission lines, many of which are forbidden lines, while narrow emission lines are missing from the spectrum of many high luminosity type 1 AGNs. Additional sub-division (1.5, 1.8, and 1.9) exist inside this group, most of them based on the relative intensity of the broad and narrow components of the Balmer lines. Objects with broad Paschen lines, usually referred as intermediate objects, are referred to as type 1i. Some of the distinctions of these sub-groups might

not be caused by intrinsic differences in the central engine but they could also be caused by variability effects or obscuration from the host galaxy.

The high-luminosity type 1 objects, where the nuclear light outshines the surrounding galaxy, are often called Quasi-Stellar Objects (QSO's) or quasi-stellar radio sources (quasars). The lower-luminosity objects are called Seyfert 1 galaxies.

1.2.1.2. Type 2 AGNs

This type of objects show strong narrow (300-$1000 \, \mathrm{km \, s^{-1}}$) NIR/optical/UV emission lines that clearly show indication of photo-ionization by a non-stellar source. The absence of optical/UV continuum emission in Type 2 objects is in agreement with the idea that the dust obscures the BBB from the accretion disc. Typical strong lines are [O III] $\lambda5007$, [N II] $\lambda6584$, [O II] $\lambda3727$, [O IV] $\lambda25.9$mum, [Ne V] $\lambda3426$, [C IV] $\lambda1549$ and the hydrogen Balmer and Lyman lines. Type 2 AGNs are further divided into two subgroups: 1) Hidden type 1 sources with broad emission lines seen in polarized light and 2) 'true type 2' AGNs, although this class is less well defined. The latter subgroup members shows similar width and excitation narrow lines but no detectable broad lines and little X-ray absorption. Their mean luminosity is below the luminosity of the type 2 objects with hidden broad lines.

The lower luminosity type 2 objects, often hosted by spiral galaxies, are called Seyfert 2 galaxies, the higher luminosity types, often hosted by elliptical galaxies and discovered because of their radio emission, are typically Radio galaxies (RGs).

1.2.1.3. Low-Ionization Nuclear Emission-line Region (LINERs)

The spectra of these objects show low ionization, narrow emission lines from gas ionized by a non-stellar source and without presence or a relatively low contribution of high ionization emission lines. Typical strong emission lines in this group are [N II] $\lambda6584$, [N II] $\lambda6584$ and [S II] $\lambda6731$, and the Balmer lines. Similar to Seyfert Galaxies, LINERs can be divided into type 1 LINERs with broad emission lines and type 2 LINERs with only narrow emission lines. Some but not all LINERs show point-like X-ray and UV sources and UV and X-ray variations [Maoz, 2007; Hernández-García et al., 2013].

1.2.1.4. BL Lac Objects

These are relatively low luminosity galaxies showing extremely high surface brightness, rapidly variable emission. These are interpreted to be AGNs viewed directly into their relativistic jets, which are responsible for the bright emission.

1.3. Investigating the dusty environment

As discussed in the previous section, dust is one of the main components of the unification theory of AGNs. In the strictest version of this theory, all types of AGNs are surrounded by an optically thick dust torus and are basically the same object but viewed from different lines of sight.

Therefore, the key factors in understanding the structure and nature of AGNs include the determination of the geometry of the nuclear obscuring torus and the obscuration properties of the circumnuclear dust. An accurate knowledge of the dust extinction properties is also required to correct for the dust obscuration in order to reconstruct the intrinsic optical/UV spectrum of the nucleus from the observed spectrum and to probe the physical conditions of the dust close to the nucleus.

Direct evidence for the presence of a dust torus is provided by infrared observations [e.g., Jaffe et al., 2004] but to properly interpret the observed infrared continuum emission and spectroscopy as well as the infrared images of AGNs, we require a good understanding of the absorption and emission properties of the circumnuclear dust. To achieve this goal, we need to know the composition, size, and morphology of the dust in order to compute the absorption and scattering cross sections of the dust from X-ray to far-IR wavelengths, and then calculate its UV/optical/near-IR obscuration as a function of wavelength, and derive the dust thermal equilibrium temperature as well as its infrared emission spectrum. This will allow us to constrain the circumnuclear structure through modeling the observed infrared emission and its spatial structure; which is critical to our understanding of the growth of the central supermassive black hole. However, still many properties of the dust in the circumnuclear torus of AGNs remains undetermined.

1.3.1. Observing the nuclear dusty emission

Although we are able to spectrally isolate the torus emission by observing in the infrared, many studies have shown that the infrared emission generated by the nuclear dust comes from a region of a few parsecs [see e.g., Alonso-Herrero et al., 2011; Asmus et al., 2014]. If we want to answer questions about the geometry of the dusty environment we cannot only rely on low spatial resolution observations. The small angular sizes (a few milliarc seconds) corresponding to the dusty torus are beyond the spatial resolution capabilities of any single telescope.

Neglecting atmospheric or instrumental effects, bigger telescopes produce sharper images. The angular resolution of a telescope is inverse proportional to the diameter D its aperture, $\theta \sim \lambda/D$, where λ is the observed wavelength. Therefore, in order to reach the angular resolution required to resolve the infrared emission from the dusty environment we need single-aperture telescopes with mirrors of about hundreds of
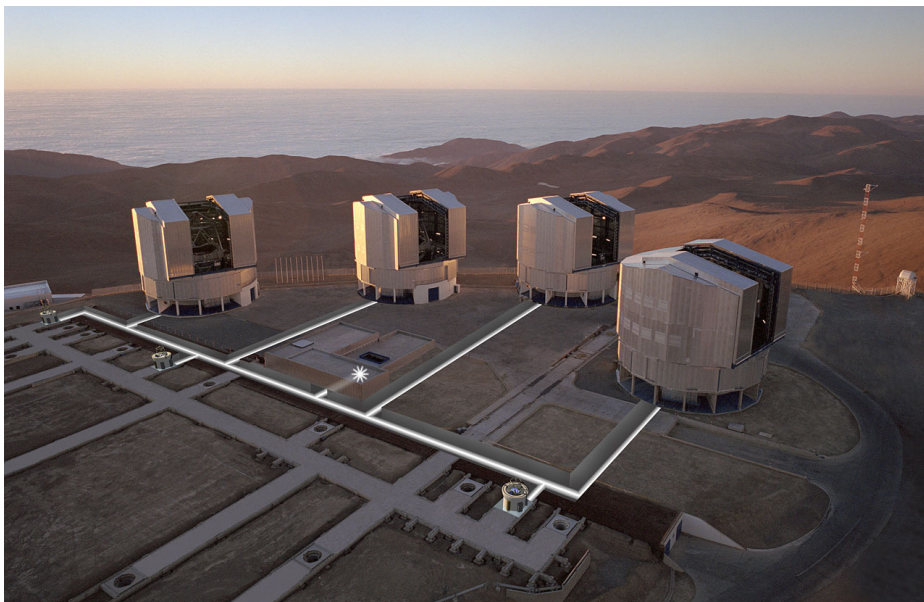
Figure 1.2: *Aerial view of the Very Large Telescope Interferometer (VLTI), Courtesy of ESO.*

meters in diameter. Building such giant telescopes is currently not feasible, but there is an alternative to this problem. Instead of having one single-aperture telescope with a diameter of hundreds of meters we could replace it with two or more telescopes, with much smaller diameters, separated by a hundreds of meters. By combining the light beams from several small telescopes using interferometry, we synthesize a large aperture and achieve the high resolutions required. A brief explanation on how an interferometer works is given in the following subsection.

1.3.2.   Infrared interferometry

An interferometer combines two or more separate parts of the wavefront in order to produce an interference pattern. Since the telescopes are located at different distances, the light will not reach all the telescopes at the same time. Corrections to make the path lengths equal are applied so that the infertefometric fringes are visible. These corrections are usually done by making the light to travel longer distances before combining the light. The crude part of this correction is to allow observations of objects all over the sky, not just those which are directly overhead. This is achieved by delaying one beam which allows to steer the interferometer. Additionally, due to atmospheric changes the length of the path that the light travels changes rapidly and randomly a few tens of microns. To compensate for such changes an allow the

integration of the light for long periods, a fringe tracking system is typically needed. The fringe tracking can be done on the scientific target or on a nearby reference star. Nevertheless the ability to track fringes is a difficult requirement and will usually set the limiting magnitude of the interferometer.

When we observe a distant object in this way, we see an interference pattern or interference fringes. These fringes arise because of the wave nature of light and they contain information about the object being observed. The signal recorded after combining the light is nothing else than the Fourier transform of the sources brightness distribution. The normalized value of the spatial coherence function V is then equal to the normalized Fourier transform of the sky brightness distribution, I, this is formally written as

$$V(u,v) = \frac{\iint I(l,m) \, e^{-2\pi i(ul+vm)} \, dl \, dm}{\iint I(l,m) \, dl \, dm}, \tag{1.1}$$

where, u and v are the components of the baseline vector measured in wavelengths and projected onto the plane perpendicular to the incident wavevector, and l and m are angular co-ordinates on the sky. In interferometry, the distribution of the telescopes (or antennas) is referred to as the '(u,v) plane', where each point on the plane is the projected position of each telescope. The visibility of fringes is a number between zero and one which measures the fringe contrast. It is defined as $V = (I_{max} - I_{min})/(I_{max} + I_{min})$. If the fringes have a visibility of one we say the object is unresolved. If V = 0 there are no fringes and the object is completely resolved.

1.3.2.1. The MIDI instrument

Observations presented in this thesis as well as the data compiled from previous publications, were all observed with the MID-Infrared Interferometric Instrument [MIDI, Leinert et al., 2003] at the European Southern Observatory's (ESO) Very Large Telescope Interferometer (VLTI) located on Cerro Paranal in Chile. For many years, the MIDI instrument probed to be the best and only option to resolve the infrared emission from AGNs

The very large telescope interferometer (VLTI) is composed of four $8.2\,\mathrm{m}$ unit telescopes (UTs), and several $1.8\,\mathrm{m}$ auxiliary telescopes (ATs). The light received by the telescopes travels trough the tunnels to a common location where the beams are combined by the specific instrument used. Since the optical path difference between the telescopes and instrument must be zero, the delay lines are equipped with mobile retroflector carriages which are able to move with a precision of a micron.

After the beam combiner, the beams pass thorough a dispersive element to generate a spectrum. Two available dispersive elements can be used in MIDI: 1) The low resolution *Prism* with spectral resolution $R \equiv \lambda/\Delta\lambda \sim 30$ and the *Grism* with

Principle of MIDI - the MID- infrared Interferometer for the VLTI
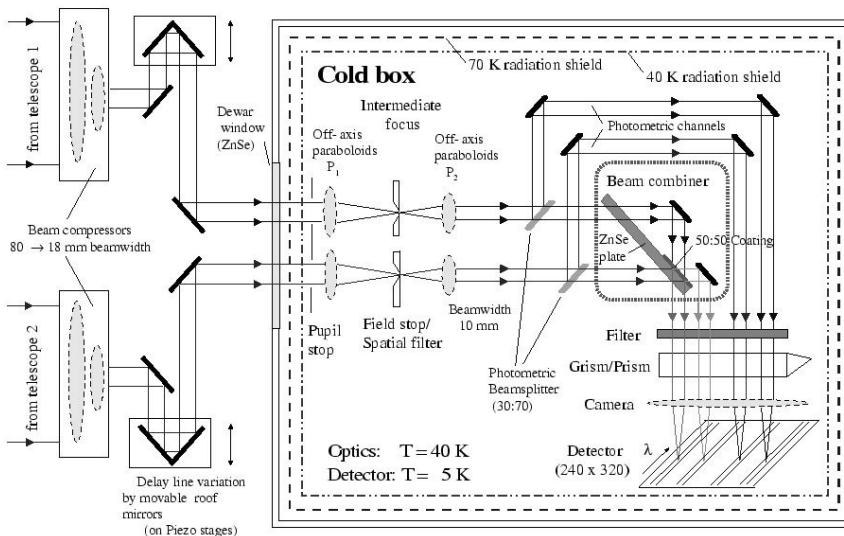
Figure 1.3: *Principle of the MIDI instrument. Image courtesy of ESO.*

R= 230. As most of the AGNs observed with the instrument MIDI are quite faint, the Prism was used for all of them except for a few observations of NGC 1068.

For planning out the observations presented in this work we used the techniques and knowledge developed during previous AGN observations. For a very detailed explanation about the observing strategy, data reduction process, and analysis of the data we referred to Burtscher et al. [2012]. The reduction of the data was performed with the interferometric data reduction software MIDI Interactive Analysis and Expert Work Station [MIA+EWS[1], Jaffe, 2004] which implement the method of coherent integration for MIDI data.

1.3.3.   Dusty models

Because current interferometric observations do not provide true images of the infrared emission we need to build brightness distribution functions that suits the observed visibilities. This can be done by using known brightness distribution functions, such as Gaussians distributions, or build complex brightness distribution functions using radiative transfer methods. For this work we used both simple functions and images computed from complex dusty structures.

---

[1]EWS is available for download from:
http://home.strw.leidenuniv.nl/∼jaffe/ews/index.html.

vertical distribution
(opening angle, τ_v(vert.), $\tau_{cl} \times N_{cl}$(vert.), flaring)

optical depth
(dust mass; τ_v(eq.); $\tau_{cl} \times N_{cl}$(eq.); vol. filling factor; R_{cl})

radial dust distribution

R_{out} R_{in} (or L) R_{in} (or L) R_{out}

Figure 1.4: *Setup of a typical model in a clumpy (right) and smooth (left) case taken from [Hoenig, 2013]*

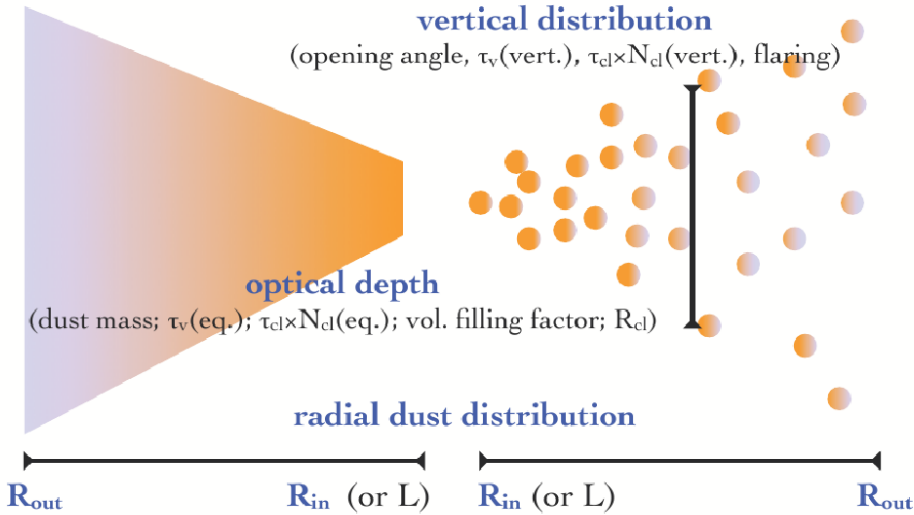Current radiative transfer models of AGN tori are built using arbitrary prescriptions for the distribution of the dust in the model space and a broad family of numerical radiative transfer models has been developed [Schartmann et al., 2005; Dullemond & van Bemmel, 2005; Hönig et al., 2006; Schartmann et al., 2008; Nenkova et al., 2008a,b; Stalevski et al., 2012]. Despite the use of different assumptions or prescriptions, in general, AGN torus models share some fundamental similarities. These similarities are summarized in Figure 1.4. The model space is usually delimited by an inner radius R_{in} and an outer radius R_{out}, where the inner radius is typically determined by the sublimation radius. The distribution of the dust in radial direction is typically defined by a radial power law distribution, $n(r) \sim r^{-\alpha}$ where α is the power-law index that defines compactness or shallowness of the dust or dust-cloud distribution. The typical geometrical thickness of the models which can go from homogeneous vertical distributions with a cut-off height or scale-height to Gaussian or power-law distribution functions. The absolute density or dust mass in the model space is defined by specifying one of these two quantities or by defining an optical depth value along a preferred line-of-sight as a normalization.

The advantage of radiative transfer models is their relative simplicity that makes it easy to simulate model grids. However, they do not contain any physical constraints of the environment. In order to study the dynamics of the gas and dust around the black hole in the region of the torus, a number of hydrodynamic models has

been developed with the goal to reproduce the mass distribution self-consistently [Schartmann et al., 2009; Dorodnitsyn et al., 2011; Wada, 2012; Schartmann et al., 2014]. Since most of them are computationally expensive, the task of providing photometric observations or images for a wide range of parameters still needs to be improved. On the other hand, since both densities and kinematics are predicted, the models provide a physical basis for studying molecular lines on scales of several to tens of parsecs.

1.4.   This Thesis

In this thesis we study the mid-infrared emission produced by the nuclear dusty environment of AGNs. We take advantage of the relevant information provided from infrared interferometric observations to explore the geometry and properties of the dusty region. Here is a brief summary of the contents of each chapter.

Previous interferometric observations of NGC 1068 revealed the existence of a hot disc-like structure in the nuclear dusty environment, but its surrounding environment was not fully revealed due to the lack of low resolution short baseline measurements. We therefore obtained a new series of interferometric measurements to study the missing scales. In **Chapter 2** we present the observations obtained with the instrument MIDI in combination with the 1.8 m Auxiliary Telescopes. We analyze the nuclear dusty environment of NGC 1068 combining the low and high resolution data. We model the observed correlated fluxes and differential phases using offset Gaussian distributions and found that at least half of the mid-infrared emission coming from the central 600 milli arcsecond region is produced at a region at least 7 parsecs away from the region where the nucleus of the AGN should be. We think that the warm offset extended emission is consistent with dust heated along the walls of the ionization cone.

In **Chapter 3** we analyze mid-infrared interferometric observations of 23 objects to retrieve additional geometric information. Individually observed objects have revealed nuclear polar elongated emission attributed to dust instead of the expected equatorial emission. We investigate our ability to identify elongated shapes with respect to (u, v) coverage and the signal-to-noise ratio. In 7 of the 23 objects, we revealed with accuracy their geometrical shape at a first order. 5 objects have elongated mid-infrared emission with its major axis closer to the polar axis of the system than perpendicular to it. The other 2 objects are less elongated and their shape could be consider as circular. A polar elongated emission supports the idea of a dusty-wind environment rather than the classical torus-like structure.

Mid-infrared interferometric observations obtained with the instrument MIDI lack true phase information. Without the phase information, it is difficult or even impossi-

ble to apply image reconstruction techniques. As an alternative, we use the brightness distributions obtained from 3-dimensional clumpy torus models to retrieve information about the dusty environment. In **Chapter 4** we present a statistical analysis of a sample of sources. We find that the differences in type 1 and type 2 objects are too complex to be explained only by inclination effects or statistical variations of the clouds. We are able to explain each Seyfert type separately and the biggest difference between them is in the fraction of volume occupied by the dust. For type 1 objects, the observed interferometric visibilities are better explained by using a low number of clouds. Our findings suggest that at least two possible families of type 1 objects would be required. Although a larger number or a continuous transition between type 1s could also be possible.

In **Chapter 5** we analyze in detail the mid-infrared emission of dusty clouds in order to learn more about the role of the optical thickness, the relative location of the clouds and inclination with respect to the observer. By analyzing the mid-infrared spectral index $(8-12.5\,\mu\text{m})$ and the strength of the silicate feature we are able to provide an explanation for the observed differences in Type 1 AGNs. We find a correlation between the spectral index and the average location of the clouds that is hard to explain with an inclination effect. Our results suggest that the observed differences in Type 1 spectra are caused by size variations in the cloud distribution.

In **Chapter 6** we investigate if there is any signature in the infrared produced as a response for a recent X-ray variability in the nuclear region of NGC 1068. The observed mid-infrared interferometric signal observed before and during the X-ray variations showed no clear changes. This suggests that the mid-infrared environment of NGC 1068 has remained unchanged for the last 10 years and that the X-ray variation detected with *NuSTAR* measurements is due to X-ray emission piercing through the dusty region.

In **Chapter 7** we present a summary of the work done for this thesis. We present a brief discussion where we place our findings in the context of current research. We additionally discuss the implications of this work and the directions to pursue.

CHAPTER 2

Revealing the large nuclear dust structures in NGC 1068 with MIDI/VLTI

N. López-Gonzaga, W. Jaffe, L. Burtscher, K. R. W. Tristram, K. Meisenheimer

Astronomy and Astrophysics, 565, A71 (2014)

Abstract

The aim of this work is o understand the relation in Active Galactic Nuclei (AGNs) between the small obscuring torus and dusty structures at larger scales ($5-10$ pc). The dusty structures in AGNs are best observed in the mid-infrared. To achieve the necessary spatial resolution ($20-100$ mas) we use ESO's Mid-Infrared Interferometer (MIDI) with the 1.8 m Auxiliary Telescopes. We use the *chromatic phases* in the data to improve the spatial fidelity of the analysis. We present interferometric data for NGC1068 obtained in 2007 and 2012. We find no evidence of source variability. Many (u, v) points show nonzero chromatic phases indicating significant asymmetries. Gaussian model fitting of the correlated fluxes and chromatic phases provides a three-component best fit with estimates of sizes, temperatures, and positions of the components. A large, warm, offcenter component is required at a distance approximately 90 mas to the northwest at a position angle (PA) of $\sim -18°$. The dust at $5-10$ pc in the polar region contributes four times more to the mid-infrared flux at $12 \, \mu$m than the dust located at the center. This dust may represent the inner wall of a dusty cone. If similar regions are heated by the direct radiation from the nucleus, then they will contribute substantially to the classification of many Seyfert galaxies as Type 2. Such a region is also consistent in other Seyfert galaxies (the Circinus galaxy, NGC 3783, and NGC 424).

2.1. Introduction.

Active Galactic Nuclei (AGNs) have been intensely studied because they host many interesting physical processes, such as accretion of material and formation of jets. Many subclasses of AGNs have been defined based on observational criteria; the earliest of these was defined by Seyfert [Seyfert, 1943] by the presence of high ionization forbidden lines. They additionally show low ionization lines and very high ionization coronal lines. The similar line ratios from galaxy to galaxy suggest that they are powered by the engines of the same type, but they also show differences that have led to a dual classification: Type 1 galaxies show broad optical permitted lines absent in Seyfert Type 2. The idea that Type 1 and Type 2 share an underlying engine is strongly supported by the detection of polarized broad lines in 3C 234 [Antonucci, 1984] and NGC 1068 [Antonucci & Miller, 1985]. These polarized spectra, most probably caused by electron scattering, revealed the existence of a broad line region (BLR) in Type 2 galaxies.

To explain the different appearances of various types of AGN, the existence of an axisymmetric dusty structure, a *torus*, was proposed in the context of AGN Unified Models [Antonucci, 1993; Urry & Padovani, 1995]. The general concept is that the Type 2 galaxies are absorbed Type 1 galaxies, where the orientation and absorption of the torus play a major role in shaping the apparent properties. The energy absorbed by the torus will be re-emitted mainly in the mid-infrared wavelength regime, giving rise to a pronounced peak in the spectral energy distribution of many AGNs [Sanders et al., 1989]. Resolving the morphology of this mid-infrared radiation is the key to understanding the physical properties of the dust structures. However, they are typically too small to be resolved even with the largest single-dish telescopes. Only with the availability of powerful techniques such as mid-infrared interferometry has further progress been possible. Several interferometric studies in the mid-infrared have been published for individual galaxies. They include the brightest AGNs, the Circinus galaxy [Tristram et al., 2007], NGC 1068 [Jaffe et al., 2004; Poncelet et al., 2006; Raban et al., 2009], and Centaurus A [Meisenheimer et al., 2007; Burtscher et al., 2010], and the brightest Type 1 Seyfert galaxy, NGC 4151 [Burtscher et al., 2009]. Recently, two fainter sources, NGC 424 [Hönig et al., 2012] and NGC 3783 [Beckert et al., 2008; Hönig et al., 2013] were observed with a very well sampled (u, v) coverage. Studies with the intention of getting general properties of the objects have also been published. Kishimoto et al. [2009b] claimed evidence for a 'common radial structure' for the nearby AGN tori. Tristram et al. [2007] demonstrated that weak AGNs can also be observed with MIDI and saw the first evidence for a size-luminosity relation [Tristram et al., 2009]. Burtscher et al. [2013] modeled 23 AGNs and found that there is a large diversity in nuclear mid-IR structures that is not attributable to luminosity of the source or resolution of the observations.

This paper extends our previous work on the near-nuclear, parsec scale dust structures in NGC 1068 in order to investigate the connection with the larger scale structures. We achive this by making use of low spatial frequency interferometric observations. The outline of this paper is the following: in Sect. 2.2 we give a summary of the previous mid-infrared observations of the nuclear dust in NGC 1068. We describe the new observations and data reduction process in Sect. 2.3. In Sect. 2.4 we present the interferometric data with emphasis on the *chromatic phases* that give insights into asymmetric morphologies. We investigate the radial profile of the correlated fluxes and the possibility for variability. In Sect. 2.5 we explain the Gaussian model used to reproduce the interferometric data and the parameters that best fit. We discuss the best models in Sect. 2.6, analyze the properties of the components of the model and identify the dust regions associated with each component. In Sect. 2.7 we study the possible heating mechanism for the two mid-infrared northern components found from the modeling. In Sect. 2.8 we discuss the asymmetry of the mid-infrared nuclear region in NGC 1068 and its implications. Finally, we present our conclusions in Sect. 2.9.

2.2. Previous infrared observations of the nucleus of NGC 1068

The galaxy NGC 1068, at a distance of only 14.4 Mpc, is a prototype Seyfert 2 galaxy that has been intensively studied. Its proximity and infrared brightness make it a suitable target to study the dusty structures that obscure the nucleus. Previous high spatial resolution single telescope studies revealed the existence of an infrared extended emission region around the central engine (Bock et al. 1998, 2000; Tomono et al. 2001; Galliano et al. 2005b in the MIR, and Rouan et al. 1998, 2004; Gratadour et al. 2006 in the NIR). In the mid-infrared regime, single-dish observations indicate that the extended emission has an elongation of about 1" in the north-south direction and is unresolved in the east-west direction [Bock et al., 2000]. The emission shows a strong asymmetry, with a larger emission area extending more to the north than to the south.

Jaffe et al. [2004] demonstrated the existence of a central parsec-sized circumnuclear dust structure in NGC 1068 using mid-infrared ($\lambda = 8 - 13\,\mu$m) interferometric observations from ESO's VLTI/MIDI. Raban et al. [2009] reported additional MIDI observations with a more extensive (u, v) coverage of sixteen baselines which allowed them to investigate the structure of the inner regions of the obscuring disk with greater detail. In both cases, a two-component model, each with a Gaussian brightness distribution, was used to fit the correlated fluxes obtained from MIDI. The size and orientation of the hot component ($\sim 800\,$K), associated with the inner funnel of

the obscuring disk, were well fitted with an elongated Gaussian 1.35 parsec long and 0.45 parsec thick (FWHM) at a position angle (PA) of -42 °. The data strongly suggest that the dusty disk and the optical ionization cones from the jet are misaligned in NGC 1068. The disk is co-linear with the H_2O megamaser disk [Greenhill et al., 1996].

A second, more extended component was also detected. This component was over-resolved by the interferometer and its geometrical parameters were not well constrained. The analysis implied a warm ($\sim 300\,K$) structure of $\sim 3 \times 4\,pc$ in size. While the position angle could not be determined, the authors suggest that a north-south elongated structure could be identified with the elongation of the mid-infrared region of NGC 1068, seen by Bock et al. [2000], who attribute it to re-emission by dust of UV radiation concentrated in the ionization cone. This component is part of the environment surrounding the inner hot dust region, and according to Poncelet et al. [2007] it represents a large fraction of the emission within the MIDI field of view. Using single-dish telescope VISIR data, they find a compact component $< 85\,milliarcseconds$ (mas) in size directly associated with the dusty torus, and an elliptical component of size $(< 140)\,mas \times 1187\,mas$ at PA $\sim -4\,°$. They suggest that the extended environment surrounding the compact $800\,K$ dust region contributes more than $83\,\%$ of the total core emission.

2.3.   The current observations

2.3.1.   Motivation

Since the extended component was overresolved in the observations reported by Raban et al. [2009], little is known about the physical nature of the structures on $5 - 10$ parsec scales and different models could describe this region. The cooler emission on these scales may simply represent an extension of the inner dust accretion disk on larger scales. It may also arise in the intermediate region between the inner dust accretion disk and the outer circumnuclear starforming regions as suggested by the co-evolution scenario of nuclear starbursts and tori from Vollmer et al. [2008] and modeled for the case of NGC 1068 by Schartmann et al. [2009, 2010]. We may also have a region where interactions between the accreting dust structures and infalling material [Müller Sánchez et al., 2009] and winds originating near the nucleus are present. To clarify these questions we obtained a new set of mid-infrared interferometric observations with MIDI/VLTI, using smaller baselines to better map these larger scale components.
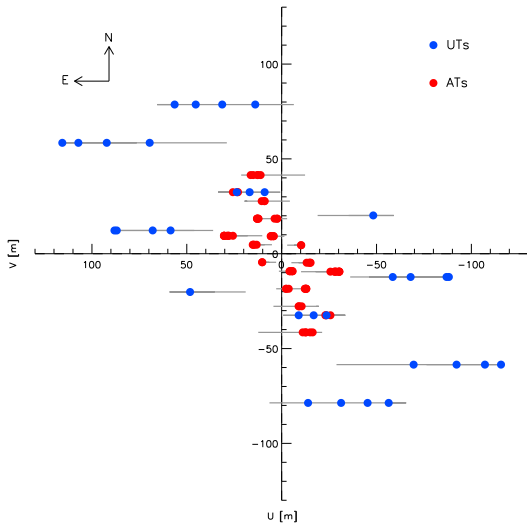
Figure 2.1: *(u, v) coverage for NGC 1068 showing both UT and AT configurations. Blue dots show the measurements taken with the UTs and red dots represent the (u, v) points measured with the ATs in 2007 and 2012.*

2.3.2.   Description of the observations

Our interferometric observations were performed in the N band in a wavelength range from $8\,\mu$m to $13\,\mu$m with the MID-Infrared Interferometric Instrument [MIDI, Leinert et al., 2003] at the Very Large Telescope Interferometer (VLTI) located on Cerro Paranal in Chile and operated by the European Southern Observatory (ESO).

The MIDI instrument is a two beam Michelson interferometer that combines the light from two 8.2-meter unit telescopes (UTs) or two 1.8-meter auxiliary telescopes (ATs). The main observables from MIDI are the single-dish spectra and the correlated flux spectra that are obtained from the interference pattern generated by the two beams. For our new observations we used only the ATs. They are movable, allowing the observation of more and shorter baselines than can be observed with the UTs. Their adequate sensitivity and available baselines from 10 to 50 meters makes them suitable to study the region of $1-10\,$pc of NGC 1068. For our observations we used the low resolution NaCl prism with spectral resolution $R \equiv \lambda/\Delta\lambda \sim 30$ to disperse the light of the beams.

Observations were carried out on the nights of October 7 and 8, 2007, and September 19, 20, and $23-26$, 2012, using guaranteed time observations (GTO). Two nights of observation (September 23 and 26) were discarded because of bad weather conditions. A log of the observations and instrument parameters can be found in Appendix B. Because of the near-zero declination of NGC 1068 the baseline tracks in the (u, v)-plane are parallel to the u-axis (see Fig. 2.1). This figure shows the previous UT observations together with the new AT observations. During our observation

period we also tried the new MIDI + PRIMA fringe sensor unit (FSU) mode [Müller et al., 2010; Pott et al., 2012]. This was done for two main reasons: 1) to stabilize the fringes on the long baselines and 2) to use the FSU to get an estimate of the K-band visibility on new (u, v) points. Previous VLTI/VINCI observations of Wittkowski et al. [2004] are available for one baseline along PA = $45°$. Unfortunately the PRIMA FSU was not sensitive enough to improve upon the self-fringe tracking by MIDI.

2.3.3.   Calibration and Data reduction

The calibrators used were HD10380 and HD18322. We choose them because they were close in airmass to the target with $\Delta(\sec z) \leq 0.25$. We started each observation night using HD10380 as calibrator and when the altitude of the calibrator was less than the altitude of NGC 1068, we changed to HD18322, which at that point was located $10°$ higher than NGC 1068.

We have applied the techniques developed during the MIDI AGN Large Program [Burtscher et al., 2012] to plan our observing strategy, data reduction process, and analysis of the data. Based on their experience we have optimized our observing sequence by switching as quiclky as possible between target and calibrator fringe track. This was done by omitting single-dish observations and also avoiding fringe searches. For each (u, v) point we performed a sequence of CAL-SCI-CAL, i.e., calibration measurements were taken just before and after a science fringe track; this allowed us to have a much better estimate of the correlated flux of NGC 1068 than using standard observing procedures (CAL-SCI). The additional calibration observations allow more reliable estimates of the instrumental visibility and therefore of the calibrated correlated flux. To correct for correlation losses due to atmospheric phase jitter we performed *dilution* experiments similar to those done for the MIDI AGN Large Program [Burtscher et al., 2013]. Correlation losses for our faintest fluxes are less than 10% of the correlated fluxes, which is less than the uncertainties (see Sect. 2.4.1)

The reduction of the data was performed with the interferometric data reduction software MIDI Interactive Analysis and Expert Work Station [MIA+EWS[1], Jaffe, 2004] which implement the method of coherent integration for MIDI data. Calibration of the correlated fluxes was computed by dividing the correlated fluxes of the target by those of the calibrator and multiplying by the known flux of the calibrator. For HD10380 and HD18322 we used the spectral template of Cohen et al. [1999]. In the remainder of this paper we follow the radio astronomical custom of using *correlated* fluxes rather than *visibilities* which are defined as the correlated flux divided

---

[1]EWS is available for download from:
http://home.strw.leidenuniv.nl/~jaffe/ews/index.html.

by the total or *photometric* flux. At short infrared wavelengths visibilities are less susceptible to changes in atmospheric conditions than correlated fluxes, but at longer wavelengths, i.e., in the mid-infrared, the difficulties of measuring photometric fluxes against the fluctuations of the bright sky favor the use of correlated fluxes.

2.4. Results

2.4.1. Correlated fluxes

In total, 40 correlated fluxes measured under good weather conditions were reduced and calibrated[2]. We have divided these visibility points into 11 groups using the criterion that visibility points of the same group be located within the AT diameter (1.8 meters) of each other. Figure 2.2 shows the correlated fluxes for each group, sorted by baseline length. The group number is indicated in the top left corner of each plot as a reference for the discussion below. The plots include (1) spectra of the individual measurements (gray); (2) the average of the measurements in the group (black); (3) the mean formal errors (average of the individual formal errors from EWS) (red); and (4) the formal errors in the means (blue error bars).

To check the consistency of calibrated interferometric fluxes with different baselines or telescopes, under different atmospheric conditions and in different epochs, we have taken multiple, independently calibrated measurements of the target at equivalent (u, v) positions. Fluxes measured at two adjacent (u, v) points cannot differ significantly if $L\Delta u/\lambda \ll 1$, where L is the overall source angular size, and Δu the separation in the (u, v) plane. A single telescope of diameter D is only sensitive to emission within a region of size $L \lesssim \lambda/D$, so we conclude that two points are equivalent if $\Delta u < D$. In our case $D = 1.8$ m. If the source is smaller, $L \ll \lambda/D$, then (u, v) points separated by larger than D should still yield the same flux.

For the spectra shown in Fig. 2.2, we observe that all correlated fluxes fall inside, or very close to, the 1-sigma uncertainty, thus verifying the formal estimates. The flux uncertainties in a single independent measurement at 8.5, 10.5, and 12.5 μm are typically of the order of 13 %, 20 %, and 17 %; uncertainties vary depending on the weather conditions. Even when observations of equivalent (u, v) points were taken on different days and under different weather conditions, the correlated fluxes are consistent with each other. Computing the average of the measurements (see Sect. 2.4.1) should give us a proper estimate of the correlated flux and we can lower the uncertainty of the error by a factor of $\sqrt{N}$, where N is the number of visibility

---

[2]The same stacking method was applied to the fringe tracks as in Burtscher et al. [2013]. Fringe tracks were reduced together when they were less than 30 min apart and were calibrated with the same star.
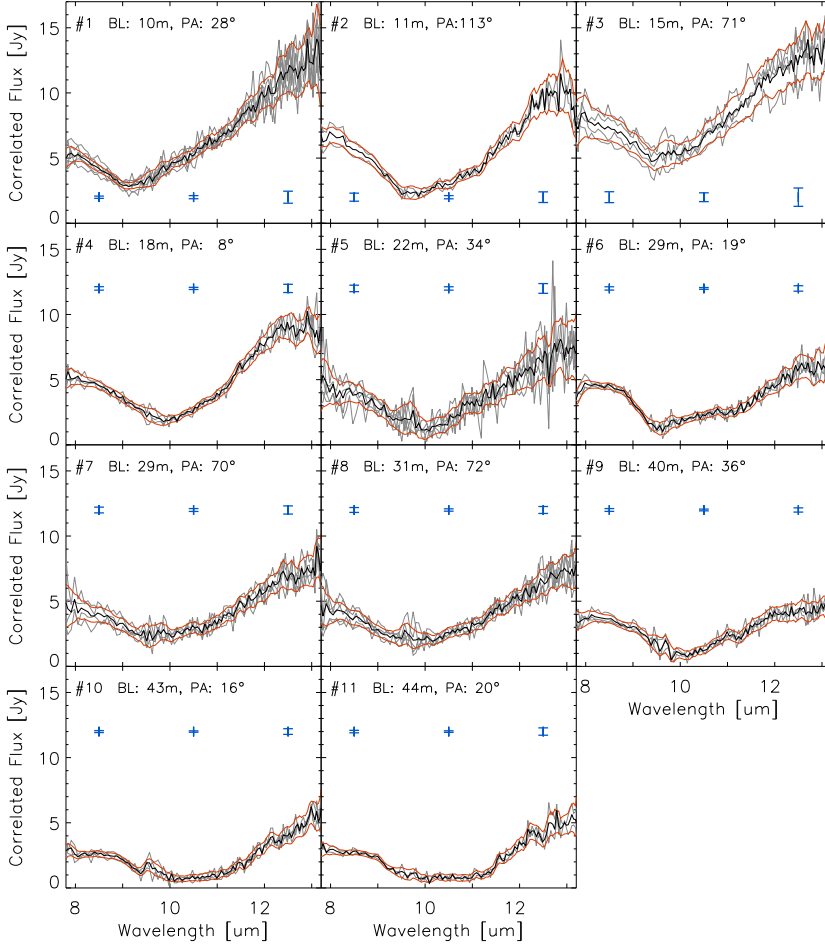
Figure 2.2: *Amplitudes of correlated fluxes measured with ATs and grouped by their separation in the (u, v) plane (see text for the selection criterion). The group numbers are given in the top left corner. The different correlated fluxes are displayed in gray lines and the average computed spectrum is shown with a black line. The red lines represent the region of the 1-sigma uncertainty of a single observation. Blue bars represent the 2-sigma uncertainty of the average computed spectrum at 8.5, 10.5, and 12.5 μm. The region between 9 μm and 10 μm has higher uncertainty because of the atmospheric O_3 absorption feature in this region.*
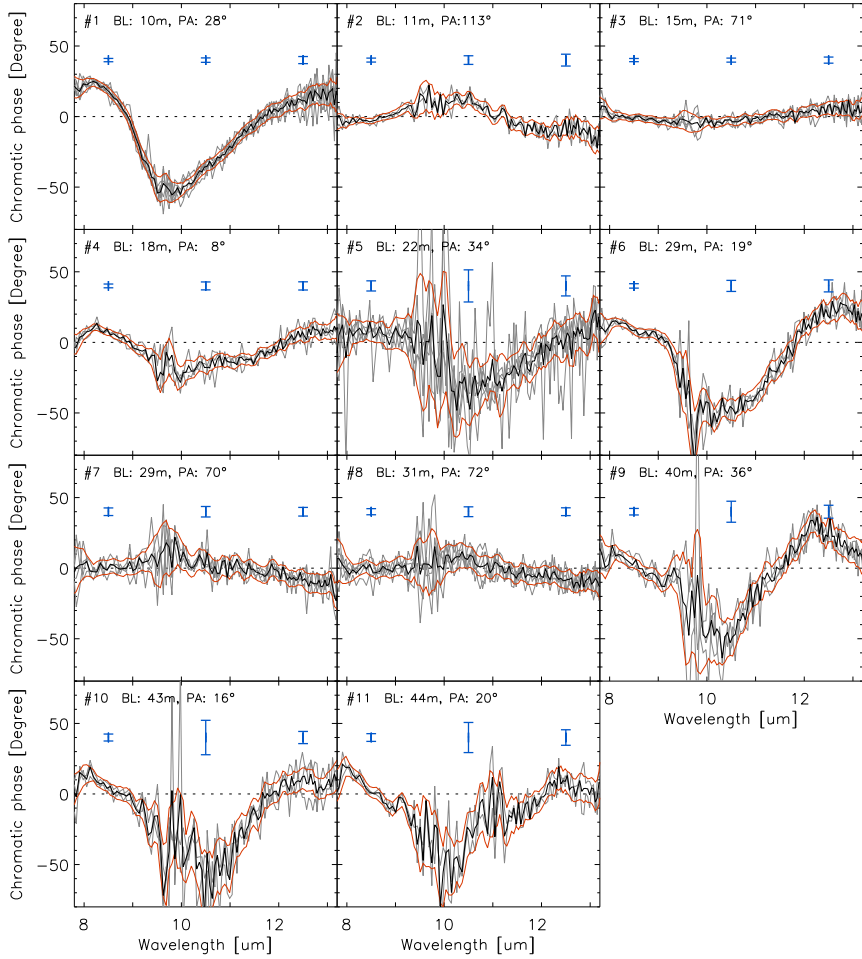
Figure 2.3: *Plots of chromatic phases grouped by their separation in the (u, v) plane. The chromatic phases of each independent observation in the group are given in gray lines and the average computed signal is shown with a black line. The red lines represent the region of the 1-sigma uncertainty of a single observation. Blue bars represent the 2-sigma uncertainty of the average chromatic phase at 8.5, 10.5, and 12.5 μm.*

Figure 2.4: *Comparison of the correlated flux observed with a projected baseline of 40 m and PA=36° using UTs (observed in 2005, Raban et al. [2009]) and using ATs (observed in 2012). The red line with error bars represents the correlated flux obtained with the UTs. The black line with a gray shaded region represents the correlated flux obtained with ATs.*

points used to compute the average. The uncertainties for the average computed flux are of the order of 6 %, 11 %, and 8 % at 8.5, 10.5, and 12.5 μm, respectively.

2.4.2. Chromatic phases

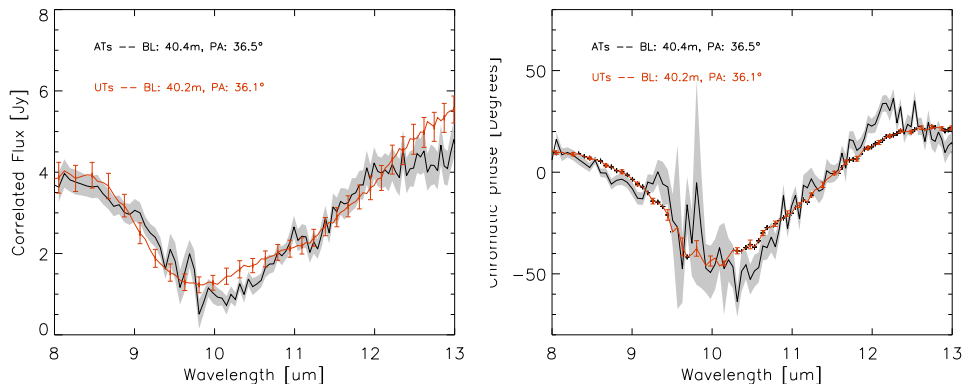The EWS software gives the amplitude of the (complex) source visibilities and the *chromatic phases*. The chromatic phases are identical to the *true* interferometric phases except that the constant and linear dependencies of phase on wavenumber $k \equiv 2\pi/\lambda$ have been removed. This occurs because the fluctuations in the atmospheric refractivity introduce phase shifts that are linear functions of wavenumber. In the absence of a phase-stable external fringe tracker the removal of these atmospheric fluctuations in the reduction process inevitably removes the linear components of the true source phases. This leaves only the second and higher order phase components. Chromatic phases cannot be used directly in image reconstruction, but still constrain the source structure. Most directly, inversion symmetric sources, averaged over the entire wavelength band, will always have zero chromatic phase[3]. Thus nonzero chromatic phases imply asymmetric structures [Deroo et al., 2007].

The grouped chromatic phases of MIDI measurements are given in Fig. 2.3. In each group the chromatic phases of every independent observation fall almost entirely within the 1-sigma region meaning that the observations are consistent with each other. As in Sect. 2.4.1 a similar computation of the average chromatic phase of each

---

[3]This description does not include cases where we have phase jumps of 180 ° at the nulls of the visibility produced by distributions such as uniform disks or rings.

group was calculated in order to obtain a proper estimate. The typical uncertainties for the measured chromatic phases of an independent observation at 8.5, 10.5, and 12.5 are $4\,^\circ$, $10\,^\circ$, and $7\,^\circ$, respectively.

The (u, v) points labelled with the number 2, 3, 7, and 8 located at position angles between $69\,^\circ$ and $114\,^\circ$ show no chromatic phases, while points located between $7\,^\circ$ and $39\,^\circ$ show significant chromatic phases[4]. This is clear evidence for non-symmetric structure. In a first approach this suggests that the asymmetry axis is located close to the north-south direction. We observe that within the range where the chromatic phases are observed ($7\,^\circ$ and $39\,^\circ$), the largest amplitude of the chromatic phases is reached in the lowest projected baseline length; there is a decrease in the amplitude around BL≈20 m and then the chromatic phases increase slightly in amplitude until BL≈40 m. This change in the amplitude indicates that the asymmetries can be found at intermediate and larger scale sizes (relative to the compact central disk). The change in the amplitude of the chromatic phases as a function of baseline length makes it difficult to explain this behavior only using color gradients, i.e., having a chromatic photocenter shift of a brightness distribution, like in the dusty region of the Circinus galaxy [Tristram et al., 2013]. This reasoning motivates us to use asymmetric shifts to explain the behavior of the chromatic phases on NGC 1068.

2.4.3.   Variability

The interferometric data of NGC 1068 was taken over a period of seven years and there is some evidence that the nucleus of this source is variable [Glass, 1997; Taranova & Shenavrin, 2006]. Therefore, we need to investigate whether source variability may influence our measurements before we attempt to model our data. To this end we compare a (u, v) point measured at two different epochs. This can provide us with information about the source evolution and/or the reliability of the instrument itself. In our dataset we have a visibility point measured using the ATs in 2012 at a projected baseline $BL = 40$ m at a position angle of $36°$. This point was measured in 2005 by Raban et al. [2009] using the 8.2-meter Unit Telescopes. Figure 2.4 shows the correlated fluxes and chromatic phases of this point at both epochs. The general trend of the spectra are consistent with each other; we only see some small deviations between the $9.7 - 10.7\,\mu$m and $12.5 - 13.0\,\mu$m, close to the regions with atmospheric absorption. The chromatic phases are mostly similar except for some small deviations around $10.5\,\mu$m and $12\,\mu$m. This (u, v) point includes most of the flux of the small hot region[5]. We expect any variability to arise from the

---

[4]From the 23 sources analyzed in Burtscher et al. [2013] only NGC 1068 and Circinus show clearly visible nonzero chromatic phases. Circinus chromatic phases are analyzed in Tristram et al. [2013]

[5]We refer to the small hot region as the $800\,$K component reported by Raban et al. [2009].
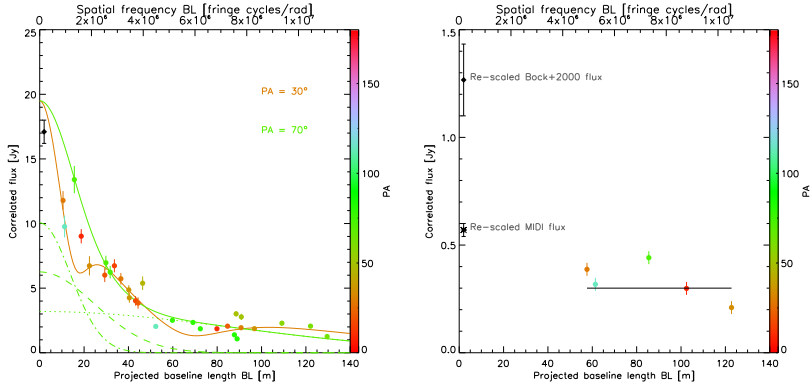
Figure 2.5: *Correlated fluxes of NGC 1068 at $\lambda = 12.5\,\mu m$ as a function of the projected baseline length BL. (Left) The data is colored according to their respectivel position angles. The solid lines represent the correlated fluxes obtained at two different position angles from the Gaussian modeling (model 1). The contribution of each component is represented by different lines: the dotted line represents the first component, the dashed line is the second component, and the dash-dotted line the third component for a PA=70°. (Right) Expected radial plot using the photometry from Bock et al. [2000] for NGC 1068 if the source is placed at a distance $\sqrt{30}$ times farther away than its current position.*

central accretion disk and the effects of a change of luminosity from this heating source to first influence the hot dust located close to the center and only later on the more distant dust. The flux from this component outside the silicate absorption feature is $\sim 5\,\mathrm{Jy}$ (see Fig. 2.4 and the modeling below) and the change in this flux as estimated from Fig. 2.4 is $<0.5\,\mathrm{Jy}$. So we can conclude that the mid-infrared nuclear flux variation in this seven-year period did not exceed $\sim 10\,\%$. Given this upper limit we include all MIDI data, regardless of epoch, in our modeling.

2.4.4.   Radial profile of the correlated fluxes

Figure 2.5 shows the radial profile of the correlated fluxes at $12.5\,\mu m$ as a function of the projected baseline length BL. The total single-dish flux is obtained from the masked total flux obtained with MIDI as reported in Burtscher et al. [2013]. This flux is limited by a mask with a FWHM of $\sim$500 mas and includes the nuclear core emission.

The correlated fluxes show a rapid drop from values around $13\,\mathrm{Jy}$ at $BL \approx 10$ m to less than $3\,\mathrm{Jy}$ at a $BL \approx 50$ m. Longer projected baselines ($50-140$ m) show an almost constant value between $1.0\,\mathrm{Jy}$ and $3.0\,\mathrm{Jy}$. The nearly constant behavior of the correlated flux as we go from 50 m to 140 m projected baseline length means

that the source of emission cannot be resolved and it must consist of one or more regions that are smaller than the resolution limit of the interferometer $\lambda/(2BL)$, i.e., less than 9 mas. On the other hand, we can also set a size limit for the large-scale structures that can be observed with the interferometer. Since our lowest projected baseline length is approximately 10 m, the largest structures that can still be resolved correspond to emission regions with a diameter of $\sim$260 mas.

We observe that 14 % of the MIDI masked flux corresponds to the emission regions with a size smaller than 50 mas in diameter while the remaining 86 % corresponds to the large-scale structures inside the core region with sizes between 50 mas and 500 mas in diameter; the upper limit is given by the resolution limit of the single-dish telescope.

The scatter seen in Fig. 2.5 for similar projected baseline lengths is caused by the position angle dependency of the correlated fluxes. Since the (u, v) coverage of NGC 1068 is not equally mapped in all directions we cannot make a proper analysis to infer information about the source size in different directions. Still at the lowest projected baseline lengths we can find three (u, v) points with a similar length (BL = 10, 11, and 15 m), but observed with different position angles (at 28 °, 72 °, and 113 ° respectively). The point with the longest projected baseline length at PA= 72 ° has the highest correlated flux. This indicates that the source is less resolved in this direction than the others.

2.4.5.   NGC 1068 in the context of the Large Program (LP) study

Results from a large survey of AGNs using mid-infrared interferometry to resolve the small-scale structures of their nuclear regions were presented in Burtscher et al. [2013]. The sources NGC 1068 and Circinus are a factor of 10 brighter than the rest of the sources analyzed in that work and they seem to have significant differences compared to the rest of the sample. A rescaling of these two bright sources was performed in Burtscher et al. [2013] to observe the radial behavior of the correlated fluxes with a resolution and flux similar to the more distant, weak sources. In the case of NGC 1068 the source was placed at a distance $\sqrt{30}$ times farther away than its current location so that its fluxes would match the median flux of the weak sources.

With our new short baseline observations we can more accurately repeat the rescaling experiment and give a quantitative description of the resulting properties when observed under conditions similar to the weak targets. To make this experiment as realistic as possible we only look at the rescaled baseline lengths that are available with the UTs. Figure 2.5 shows the radial plot of NGC 1068 after applying the rescaling at $\lambda = 12.5\,\mu$m.

To completely match the conditions of the observations of NGC 1068 with the

weak sources we have to take a photometric flux with a similar resolution to the rest of the targets. For some of the weak sources the total flux was extracted from MIDI single-dish observations using a window of size 0."5 x 0."52 or by taking high spatial resolution spectra or photometry obtained from the VLT spectrometer and imager for the mid-infrared (VISIR) using a 0."53 window in the spatial direction. If we rescale NGC 1068 to a distance which is $\sqrt{30}$ times farther away, then the 0."53 window corresponds to a ~ 3" window in the normal space. From Bock et al. [2000] we know that the flux at $12.5\,\mu\mathrm{m}$ does not vary too much from a beam of a diameter of 4" to a beam of a diameter of 2", since we need a beam of diameter of 3" we take the value of the 4" diameter beam, $F_{\mathrm{Bock}} = 36\,\mathrm{Jy}$ scaled to $1.2\,\mathrm{Jy}$ to be a reasonable approximation. Although the results from Burtscher et al. [2013] were obtained at $\lambda = 12\,\mu\mathrm{m}$ and we are going to use $\lambda = 12.5\,\mu\mathrm{m}$ for our experiment[6], the results do not vary within this wavelength range since the emission is mostly determined by the continuum and no absorption effects come in to play.

Fitting a radial model to the rescaled data, following Burtscher et al. [2013], by using a two-component model with an unresolved point source and a Gaussian component we find that the point source fraction (f_p), of the total flux is of the order of $24\,\%$ and the FWHM of the Gaussian must be $\gtrsim 36\,\mathrm{mas}$ (the data only provide a lower limit to the size). At the rescaled distance the rescaled limit of the Gaussian component corresponds to structures larger than $14\,\mathrm{pc}$. Figure 2.5 shows that the flux that we attribute to a point source comes from a partially resolved structure showing a position angle dependence that could be attributed to an elongation.

Burtscher et al. [2013] classified NGC 1068 as consisting of a resolved plus an unresolved emitter. In our rescaling experiment, where we match the fluxes and conditions of observation to the other weak sources, we now classify the rescaled version of NGC 1068 as an unresolved plus an overresolved emitter. We can now compare the results of our experiment with the results of Burtscher et al. [2013] (c.f. Figs. 30, 31, 32, and 34), where the principle difference with the earlier work is that f_p has increased from 0.1 to 0.24. This rescale value of f_p is no longer detached from the sample distribution, but appears at the lower edge, similar to Seyfert galaxies NGC 4507 and MCG-5-23-16. Thus in the context of the survey, NGC 1068 has a large but not extraordinary flux fraction in well-resolved structures.

Our experiment shows that the difference between the value of f_p of NGC 1068 and the typical values for Seyfert Type 2 sources in Burtscher et al. [2013] can be attributed in part to resolution effects. This becomes more evident in a plot of the f_p versus intrinsic resolution (see Fig. 32 in Burtscher et al. 2013). However, the new rescaling experiment does not contradict the conclusion of Burtscher et al.

---

[6]Bock et al. (2000) only report values at $\lambda = 7.9, 10.3, 12.5,$ and $24.5\,\mu\mathrm{m}$. This is the reason why we perform our analysis at $\lambda = 12.5\mu\mathrm{m}$.

[2013] that the spread in morphologies observed in the survey is instrinsic and not a resolution effect; NGC 1068 still shows some structural differences from the rest of the LP sample. It shows significantly nonzero chromatic phases at baselines of $10-20$ meters. These correspond to baselines of $60-120$ meters at the rescaled distance. None of the more distant LP galaxies shows nonzero chromatic phases at these baselines. Circinus seems to resemble NGC 1068 in this respect.

2.5. Gaussian fits

2.5.1. Motivation

Direct image reconstruction techniques cannot be applied to our interferometric data for two reasons: the limited (u, v) coverage and the lack of true phases. Still, information can be recovered by using simple analytical forms, such as Gaussians or point sources, to describe the source brightness distribution. The reason for using this approach is to describe the brightness distribution as accurately as possible with a small number of parameters while making few specific physical assumptions. In this section we present model fits for the recent observations, that allow us to specify the mid-infrared geometry of the 1-10 pc region of NGC 1068.

2.5.2. Graybody Gaussian models

Graybody Gaussian models have been used in earlier papers to model the amplitudes of the correlated flux and get estimates of the sizes, temperature, and inclinations for components in different AGN (e.g., NGC 1068, Jaffe et al. 2004; Raban et al. 2009, Circinus, Tristram et al. 2007, 2012, and Centaurus A, Burtscher et al. 2009). So far the modeling only included the amplitude of the correlated flux and thus by necessity assumed that the Gaussian components were concentric and therefore symmetric.

Raban et al. [2009] showed that the hot small emission region can be described by a Gaussian graybody with an absorption screen in front that reproduces the silicate feature. The authors described the larger scale emission region with a second component, but not enough short baseline information was available to constrain the parameters correctly. This concentric two-component model agreed well with the amplitudes of the correlated fluxes, but by definition cannot reproduce the nonzero chromatic phases described here.

For this work we again use a multi-component graybody Gaussian model to fit the mid-infrared interferometric observations of NGC 1068. The model treats the infrared emission as coming from Gaussian graybody components of a fixed size, temperature, and orientation, each one behind a uniform absorption screen, but we

no longer require the components to be concentric. The contribution to the correlated flux of each component for a (u, v) point is given by

$$F^i_{corr}(\lambda, u, v) = \eta_i BB_\lambda(T_i) \frac{\pi \Theta_i \theta_i}{4 \ln 2} V_i(u/\lambda, v/\lambda) e^{-\tau_i C^i_{abs}(\lambda)}, \qquad (2.1)$$

where T_i, τ_i, and η_i are the dust temperature, the optical depth, and the scaling factor of the component i, respectively. The scaling factor η_i can be considered to be a surface filling or emissivity factor, which is independent of the wavelength and limited to values of $0 < \eta \le 1$; V_i is the contribution of the visibility of an elongated Gaussian component, described by a FWHM (Θ_i) along the major axis, a FWHM (θ_i) along the minor axis and a position angle (ψ). The visibility function $V_i(u/\lambda, v/\lambda)$ is obtained by computing the Fourier transform of a Gaussian intensity distribution function described as

$$G_i(\alpha, \delta, \psi) = \exp \left\{ -4 \ln 2 \left[\left(\frac{\alpha'_i}{\theta_i} \right) + \left(\frac{\delta'_i}{\Theta_i} \right) \right] \right\}, \qquad (2.2)$$

where $\alpha'_i = (\alpha - \alpha_i) \cos \psi_i - (\delta - \delta_i) \sin \psi_i$ and $\delta'_i = (\alpha - \alpha_i) \sin \psi_i + (\delta - \delta_i) \cos \psi_i$ are the positional coordinates of the Gaussians, and (α_i, δ_i) is the center of the ith Gaussian component. The absorption curve for the chemical composition associated with the i-component is described by C^i_{abs}. For the dust absorption curves we have selected three dust absorption templates, including $Ca_2Al_2SiO_7$ (gehlenite; Mutschke et al. 1998) which was found as the best fit in Jaffe et al. [2004]; the standard galactic dust as observed towards the center of our Galaxy [Kemper et al., 2004]; and α-SiC [Laor & Draine, 1993] suggested by Köhler & Li [2010] as a better explanation for the anomalous absorption feature present in NGC 1068. The dust template used for each component is made from a linear combination of the three mentioned dust templates. The coefficients for each component are fitted along with the rest of the parameters.

The final form of the complex correlated flux will be given by

$$F(\lambda, u, v) = \Sigma_j F^j_{corr}(\lambda, u, v) e^{-2\pi i (u_\lambda \cdot \alpha_j + v_\lambda \cdot \beta_j)}, \qquad (2.3)$$

where α_j and β_j are the offset in right ascension and declination, respectively, and $u_\lambda = u/\lambda$ and $v_\lambda = v/\lambda$. The total single-dish flux can be recovered by using the coordinates $u = 0$ and $v = 0$, i.e., $BL = 0$ m.

2.5.3.   Offset components

In addition to the amplitude of the correlated fluxes, we have also measured the chromatic phases. As already mentioned in Sect. 2.4.2, these phases are not the true phases, but they still provide some spatial constraints. The properties of the chromatic phases observed in NGC 1068 and their distribution on the (u, v) plane

Model	i	T [K]	τ	η	FWHM major [mas] ([pc])	FWHM minor [mas] ([pc])	P.A. [degree]	α [mas] ([pc])	β [mas] ([pc])	Dust template	Reduced χ^2
						Raban et al. [2009]. Amplitudes of UT data					
0	1	800	1.9	0.25	20 (1.4)	6.4 (0.4)	-42	0 (0)	0 (0)	Fitted composite	-
	2	290	0.42	0.64	56.5 (3.9)	42.4 (2.9)	0	0 (0)	0 (0)	Fitted composite	
	3	-	-	-	- (-)	- (-)	-	-	-	-	
					Data used: Amplitudes of UT + AT data and chromatic phases of AT data						
1	1	660 ±26	1.6 ±0.2	0.31 ±0.03	20.9 ±1.7 (1.46)	7 ±0.8 (0.49)	-45 ±4	0 (0)	0 (0)	50% Gehlenite + 50% Galactic dust	6.24
	2	257 ±15	0.98 ±0.4	$1^{+0}_{-0.23}$	53 ±8.5 (3.7)	23 ±6.8 (1.6)	120^{+15}_{-30}	0 ±8 (0)	19±4 (1.32)	Galactic dust	
	3	360 ±36	0 ±0.3	0.047 ±0.016	185^{+90}_{-50} (12.9)	50^{+60}_{-20} (3.5)	-36 ±7	-30 ±17 (-2.1)	100 ±12 (7)	Galactic dust	
2	1	700 ±30	1.25 ±0.15	0.23 ±0.02	20 ±1.4 (1.4)	6.8 ±0.7 (0.47)	-45 ±4	0 (0)	0 (0)	50% Gehlenite + 50% Galactic dust	6.23
	2	301 ±21	2.8 ±0.8	$1^{+0}_{-0.2}$	42 ±9 (2.9)	29 ±8 (2)	102 ±36	3.7 ±8 (0.25)	-17.4 ±7 (-1.2)	Galactic dust	
	3	370 ±35	0.15 ±0.3	0.05 ±0.017	200^{+80}_{-60} (14)	52^{+65}_{-22} (3.6)	-35 ±6	-24 ±14 (-1.7)	80 ±10 (5.6)	Galactic dust	

Table 2.1: *Parameters found for the graybody Gaussian models. See Sect. 2.5.2 for a description of the parameters.*

excludes the possibility that all major components are concentric. Non-concentric components are required to reproduce the asymmetries observed, which are present for a wide range of projected baselines in our AT observations and there are also a few in longer baselines (see Appendix for plots of the UT data). The longest UT baselines, which respond primarily to the emission from the hot core, show small phases indicating that this core is essentially symmetric. The intermediate and short baselines respond to both the core and the larger structures and in the current models the nonzero phases indicate displacements between these components.

We can use Eq. 2 to calculate the complex correlated flux not only for the computation of the amplitude, but also for the calculation of the chromatic phases. For each modeled visibility point, the constant and linear dependencies on wavenumber are removed from the complex correlated flux. By doing this we lose some information of the exact position of each component in real space, but the information about the positions with respect to each other is preserved. To reduce the degeneracy of solutions we have fixed the position of the smallest component to be at the center of our plane, i.e., $\alpha_1 = 0$ and $\beta_1 = 0$.

We have spectra of the amplitudes and chromatic phases for 30 (u, v) points, which include information from projected baselines between 10 m and 130 m. We have attempted to fit three-component models to these data, but we have not been able to find a reasonable fit to all the data. In these attempts we can find reasonable fits for either the chromatic phases or the correlated fluxes, but not both together. Apparently a more complicated model is necessary. Because our immediate goal was to describe the emission morphology with a limited number of parameters, we have chosen not to add a fourth or additional components to improve the fit.

Instead we will focus our attention on describing only the spatial information contained in the AT observations. This approach ignores the details of the small-scale structures, but describes the relative positions of the three components with respect to each other. The result from this procedure can be interpreted as a low resolution image of the emission of NGC 1068. It is our intention to present at a later date representations of our data using more general image reconstruction techniques constrained by physically motivated emission models.

The parameters reported in this paper are the least-squares solution found using the Levenberg-Marquardt technique to fit all 30 amplitude spectra and the 11 chromatic phase spectra from AT observations reported here. The reason for not using the chromatic phases measured with the UTs is to give an equal weight to the chromatic phases in all the scales, otherwise the fitting routine would focus more on the intermediate scale regime while the aim of this work is to disentangle the large structures from the small scales. Additionally, we do not try to fit the single-dish MIDI masked flux since it was measured using the UTs. As mentioned in Sect. 2.4.4,

the masked flux could also be capturing part of the emission coming from regions farther than 250 mas away.

There is a difference in the field of view of the UTs and ATs, which means that the region observed by the ATs might include regions which are not captured by the UTs. This does not seriously affect the interferometric observations since the UTs observe the small scales and in Sect. 2.4.3 we showed that the UTs and ATs observe the same structures on the small size regime (>30 mas). The large-scale structures are over-resolved with the UT baselines and thus depend only on the information obtained from the AT baselines.

To estimate the errors in the parameters, we fixed the value of all but one parameter at a time. The uncertainties that we report represent the range of variation of each parameter sufficient to cause a significant change in the quality of fit. We saw that parameters with a reduced chi-square larger than 15 % of our best reduced chi-square begin to show significant differences.

We first attempted to fit a two-component model as Raban et al. [2009] but relaxing their assumption of concentricity. We were unable to get a reasonable fit of our data. We then tried three-component models.

We found two sets of parameters which can describe the source brightness distribution and the chromatic phases to a reasonable degree; these two sets of parameters can be seen in Table 2.1. Both models consist of two warm components using a standard galactic dust template and one hot small component using a mixture of gehlenite and galactic dust as the dust template. Contrary to what Köhler & Li [2010] report from their study, we find that the contribution of SiC in the dust templates is at most very small. Köhler & Li [2010] used the spectra of only one (u, v) point in their modeling, and the optical depth of the SiC feature can be chosen to fit well this one point, but it cannot fit the ensemble of observations. In Figs. 2.9 and 2.10 of the Appendix we also plot best-fit curves obtained for a model using only SiC as the template. The poor match to most of the data indicates why the least-squares routine avoided this component to the fits.

The size of the major and minor axes, and position angle of the hot component for both models agree with the parameters previously reported by Raban et al. [2009]. This is not surprising since we left out the chromatic phases measured with the UTs, i.e., long projected baseline; therefore the hot small emission region will be treated as a symmetric Gaussian component. The 660 K temperature for one of our models is clearly lower than the one reported by Raban et al. [2009]; the differences might be attributed to the dust absorption templates used in each model.

The two best fitting models differ primarily in the position of the intermediate-sized component. In our first model (see Fig. 2.7) we find this component to be associated with emission of dust around 257 K with a size of 3.7 x 1.6 pc elongated
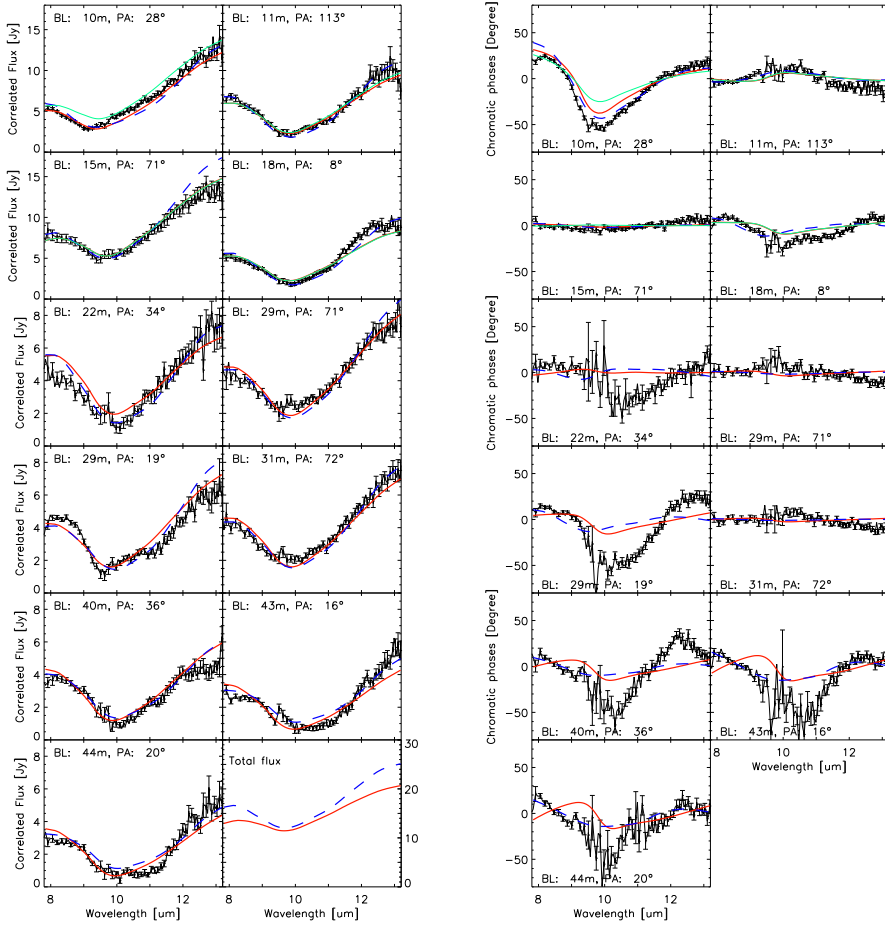
Figure 2.6: *Plots showing the best-fit model for the (u, v) points observed with the ATs. (Left) Correlated fluxes and (Right) Chromatic phases. The red line shows the corresponding correlated fluxes and chromatic phases for our non-concentric model no. 1 while the blue dashed line represent our non-concentric model no. 2. Light green lines (only on the first four plots of each panel) show the curves obtained by taking the parameters of our first-best model, and taking the lower limit of the uncertainty in the offset declination for the third component, we observe some significant deviations in some of the plots.*

at a position angle of 120 °. The position of its center is 19 mas to the north of the hot component. The third component is a large emission region with a temperature around 360 K. The center of the Gaussian which represents this large region is ∼ 100 mas to the north of the hot component and at an angle of -18 ° (measured from north to east). It is a highly elongated structure with an axis ratio of ∼ 1 : 3.7 and a position angle of −36°.

Model no. 2 also has an intermediate- and large-sized Gaussian component. The second component for this model consists of emission at 300 K with an intermediate size of 2.9 x 2 pc elongated at a PA of 102 ° and located 17 mas south of the hot component. It is absorbed by a screen with a larger optical depth close to 3. The third and biggest component with a temperature around 370 K has a FWHM of 200 mas along the major axis and a FWHM of 52 along the minor axis. The position angle of this large component is similar to the one for our first model, −35°. The center of this large emission region is also located to the northwest of the small hot component, but with a slightly different position from our first model, it can be found at a distance of ∼ 80 mas from the center and 16 ° in the NW direction. The ratio between the major and minor axis is also close to ∼ 1 : 4.

The main differences between our best-fit models lie in the parameters of the intermediate size component. In the second model this component lies to the south rather than to the north, and it has a much larger absorption optical depth. The degeneracy of the modeling, i.e., the existence of two equally good fits is caused by the limitations of using chromatic phases. The contribution of this component to the phases changes sign when it is moved to the south, but this effect is cancelled, after removal of the linear phase gradient, by the absorption-diminished emission of this component near 10 μm. This ambiguity would be removed if true phase or closure phase observations were available. These possibilities should be available with future VLTI instruments, e.g. MATISSE [Lopez et al., 2008].

The fitted correlated fluxes and the chromatic phases for both models can be seen in Fig. 2.6. The correlated fluxes fit well; deviations are mainly caused by the assumption of a Gaussian shape. The largest deviations are seen in the mid- and long- baseline range where the resolved structures are probably more complex. This is also seen in the chromatic phases; the shortest baselines are fitted well with our model. In the long baseline regime (see Appendix for plots of UT chromatic phases) the chromatic phases are mostly zero and thus our model is consistent in that regime, while in the intermediate regime the model fits poorly.
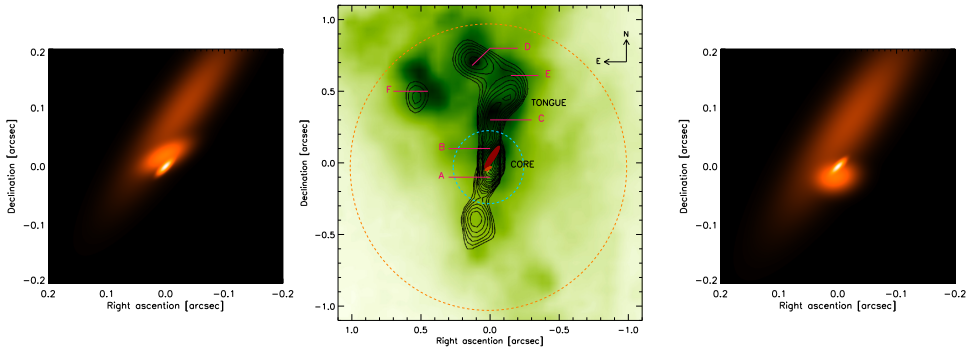
Figure 2.7: *Images of the three component models for the mid-infrared emission at 12.0 μm of the nuclear region of NGC 1068 corresponding to model 1 (Left) and model 2. (Right). The image was scaled using the square root of the brightness. (Center) Comparison between our first best model and the 12.5 μm image of Bock et al. [2000], taken with the 10m Keck telescope. The dashed circles represent the FWHM of the field of view for MIDI using the UTs (blue) or the ATs (orange). The letters indicate the positions of the [OIII] clouds according to Evans et al. [1991]*

2.6. Discussion

2.6.1. Summary of modeling

Our three graybody models provide us with a general image of the main emission regions of NGC 1068 using information from the short baselines and chromatic phases. The main differences between our models and the work by Raban et al. [2009] are the new short spatial frequency observations and the use of chromatic phases to get spatial information of the nuclear mid-infrared region. A sketch of the emission region can be seen in Fig. 2.7. Although our models are not able to reproduce the chromatic phases completely, especially in the intermediate baseline regime, we observe a reasonable consistency in the lower and higher baseline regime which fit much better than purely concentric models. The poor fits observed in the intermediate baseline regime would suggest that the link between the small scales and the large scales is more complex than can be fitted with a limited number of Gaussians and has to be modeled more carefully in order to understand the relations between the various size scales. Still, our 3-Gaussian model represents reasonably well the global variation of surface brightness with position in the nuclear region of NGC 1068. The resolution of these variations into discrete components may be an artefact of the modeling. More sophisticated image reconstruction techniques may remove these artificial transitions, but reliable multiwavelength image reconstruction algorithms that can accommodate the chromatic phase information are not yet

available.

Both models show that the maximum separation, in the north-south direction, between the center of the Gaussian components must be approximately 100 mas. Since we identify the component at $(0,0)$ with the radiation from near-nuclear dust (see Sect. 2.6.3), the large flux from the northern offset component must come from the regions located near the narrow line ionization region. This northern component is large relative to the other components in both models and the absorption optical depth and scaling factor are small. The total flux of this component reaches 10 Jy at $12\,\mu$m. Figure. 2.8 shows the total flux of each component as a function of wavelength, the ratio of the total fluxes of each component varies depending on the wavelength. We observe a ratio of the fluxes of 1 : 0.4 : 1.2 for the first, second and third components, respectively at $8\,\mu$m, 1 : 1.6 : 7 at $10\,\mu$m, and 1 : 2 : 3.5 at $12\,\mu$m. Thus, our third (the largest component) contributes with 46 %, 73 %, and 55 % of the total flux of structures with sizes below 260 mas in diameter, i.e., the ones that are resolved with the interferometer[7].

The position and absorption profile of the intermediate component are ambiguous in our models. The foreground absorption required in the second model ($\tau \sim 3$) is larger than that in front of the central component. This is counter-intuitive, but cannot be excluded in models where the dust is distributed in irregular clumps [Nenkova et al., 2008a; Schartmann et al., 2008]. This ambiguity can be removed if additional (u, v) coverage at intermediate baselines is obtained. Still, it is interesting to see that when comparing our two best models, the general trend seems to be consistent with a gradient in the silicate absorption, which decreases when going from south to north. Tristram et al. [2013] used this gradient in the silicate absorption to explain the behavior of the phases observed in the Circinus galaxy in the low spatial frequency regime. In NGC 1068, the lowest spatial frequency regime also seems to be consistent with a gradient in the silicate absorption while the chromatic phases observed in the intermediate spatial frequency regime are caused by offset components that together form a non-Gaussian shape region.

We conclude this summary by reiterating that the resolution of the emission from the galaxy into three distinct components, as seen in Fig. 2.7, is an approximation to the actual brightness distribution of the mid-infrared nuclear region of NGC 1068. If the *a priori* assumption of Gaussian components is relaxed, the components may blend into one continuous feature. The brightness distribution function for model no. 1 can be approximately represented by a continuous distribution where the brightness decreases as $r^{-\gamma}$, with r being the distance from the center of the first component and $\gamma \approx 1$.

---

[7]This information was extracted using our model no. 1. Similar results are obtained for model no. 2

2.6.2. The tongue

Single-dish mid-infrared images of NGC 1068 display a primarily N-S elongation dominated by a specific feature that Bock et al. [2000] have named the Tongue. This coincides with the regions IR-1/1b seen by Gratadour et al. [2006] in short wavelength infrared single-dish images, and component C in the VLBA radio maps of Gallimore et al. [2004]. This region extends to the north of the core, bends to the west about 0.2" above the core, and then bends to the east. It seems to be associated with part of the [OIII] emission [Evans et al., 1991] and the radio continuum emission [Gallimore et al., 1996]. According to Galliano et al. [2005b], the Tongue region (identified as the NE1) has a flux of 11.2 ± 2 Jy at $12.8\,\mu$m and is thus the second brightest mid-infrared region in NGC 1068 after the core region. Because at least part of this feature lies within the AT/VLTI field of view, we need to explore its relationship to our measurements and models. The 1.8 m diameter ATs have a field of view (FOV) of radius ~ 1.14 arcsec at $12\,\mu$m while the 8m UTs have a FOV of ~ 250 mas. From the images in Galliano et al. [2005b] and Poncelet et al. [2007] we estimate the NE1 component to be $400-500$ mas from the core. The existence of NE1 within our FOV raises two questions: (1) is component 3 in our model fits in fact identical with NE1, but incorrectly positioned due to our limited (u, v) coverage and (2) even if component 3 is distinct from NE1, do our observations place useful constraints on the morphology of NE1?

We have investigated whether positions of component 3 near NE1 are consistent with our AT data. There are such solutions, but we have discarded them as unphysical because (1) the third component then requires very high temperatures (> 800 K) to fit the short baseline spectra and (2) the total flux of the third component exceeds the values reported by Galliano et al. [2005b] and also the ones reported by Poncelet et al. [2008] at the two closest northern quadrants (3.4 Jy, 4.8 Jy, and 7.5 Jy at $9.0\,\mu$m, $10.8\,\mu$m, and $12.8\,\mu$m for their 1NO region and 1.2 Jy, 1.8 Jy, and 3.1 Jy at the same wavelengths for the 2NO region). Evidence in favor of the existence of a near-in third component is that the first two interferometric components do not provide the large flux (25 Jy) measured by these authors inside the 0.6" diameter central aperture.

We conclude that a third component < 100 mas from the core is necessary to fit the spectra at the shortest projected baselines. We now investigate whether a new extra component at the position of the Tongue could improve the fits. To avoid adding an excessive number of degrees of freedom to our model we have fixed *a priori* several Gaussian parameters of the fourth component. From the flux values reported by Poncelet et al. [2008] we think it is reasonable to fix the temperature of this component to 300 K with a very small optical depth and place it 400 mas to the north of the hot core. From the mid-infrared images reported by Bock et al. [2000] we fix the PA of the emission region to $\sim -40\,^\circ$. We allow the modeling routines
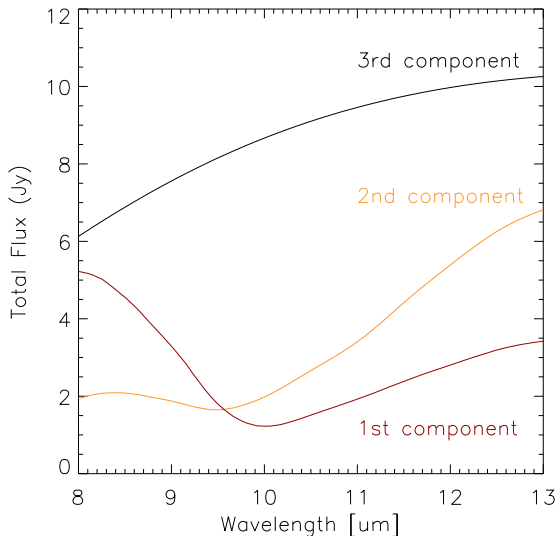
Figure 2.8: *Total flux of the three best-fit model components as a function of wavelength.*

to fit the major and minor axes, and adjust the scale factor of this component to fit the single-dish fluxes. We found that including this fourth component with these characteristics does not improve the fits. A component with a large offset (more than 100 mas) and with similar or smaller size than our component 3 would produce phase steps in the $8-13\,\mu$m region that are not observed in the data. The existence of this component is consistent with the short baseline data only if it is so large as to be essentially resolved out by the interferometer. This places lower limits of ~ 160 mas and ~ 200 mas for the minor and major axes, respectively.

2.6.3.   Cross-identification of the components

Previous single-dish observations [Bock et al., 2000] have clearly revealed an elongated region of the mid-infrared emission which extends up to 1" to the north, but their resolution was not sufficient to resolve the central emission of the core. From our interferometric observations we inferred that the emission of the core can be divided into two distinct regions: one consistent with a hot emission surrounded by warm dust (first and second components) and a large warm diffuse region approximately 100 mas (~ 7 pc) away from the other. We do not have absolute astrometric information about these components and cannot identify one with the nucleus without further assumptions.

We identify the first, most compact component with the nucleus for the following reasons: the hot temperature obtained for the small component is consistent with the temperatures obtained from dust in thermal equilibrium close to the sublimation

radius in dusty clump tori [Schartmann et al., 2008] and also consistent with the temperature of the warm ($> 600\,\mathrm{K}$) molecular dust that is expected to embed the water masers [Neufeld et al., 1994]. If we attempt to locate the nucleus in components 2 or 3 it is difficult to explain the high temperature of component 1 without invoking a new, powerful heating source. Additionally, the size and orientation of component 1 closely match those of the water maser, which must be orbiting the nucleus.

With this identification we note that at lower resolution, the peak of the mid-infrared emission will not be at the position of the small hot dust component, but near our third component, whose flux exceeds that of the nucleus by a factor of 3.5 at $12\,\mu$m. In Fig. 2.7 we sketch the positions of our components on the contour map of [Bock et al., 2000]. We observe that the inclination of our large component is roughly similar to the bend that is located to the north of the $12\,\mu$m image. Our components 1/2/3 cannot be resolved in this image. Gratadour et al. [2006] show deconvolved adaptive optics images of this region taken with the NAOS-CONICA instrument at the K-, L- and M-bands. It is possible that our component 3 is identical with the component labelled IR-CN on their Figure 4a, but the limits of the resolution and dynamic range of this data make this identification uncertain.

Our estimates of the total flux for the large component show a similar behavior to the results of Poncelet et al. [2007] who found that part of a large north-south component enters the MIDI field of view and contributes $83\,\%$ of the emission of the MIR from the core (within $500\,\mathrm{mas}$). The ratios of the $12\,\mu$m emission for our components can be summarized approximately as $1 : 2 : 3$ for the first, second, and third components respectively, meaning that the flux due to the large component should be $55\,\%$ of the core emission. The differences in percentage is possibly due to the additional components outside the central MIDI field of view that contribute to the component found by these authors.

This is not the first time that a large MIR emission along or close to the polar region is observed in AGNs. Recently, interferometric observations of Circinus [Tristram et al., 2012], NGC 424 [Hönig et al., 2012], and NGC 3783 [Hönig et al., 2013] indicate the presence of mid-IR emission along the outflow direction with a fairly big contribution to the total flux. In Hönig et al. [2012] a radiatively-driven dusty wind scenario was proposed to explain the large contributions to the mid-IR flux by polar dust.

2.7.   The energetics of the mid-infrared emission

The primary scientific results from these observations are the detection of the intermediate components 2 and 3 at 1.3 and 7 parsec north of the core, and the non-detection of the Tongue at about 35 parsec to the north of the core. In this section

we consider the possible heating mechanisms for the dust in these components.

The usual suspects are radiative heating and shock heating. These mechanisms collaborate. The hot gas in a strong shock will destroy the local dust by sputtering and conductive heating, but it will also emit ultraviolet light that efficiently heats dust in the surrounding environment. The morphology of the emission from the Tongue region supports this combined scenario. The VLBA radio images, [Gallimore et al., 2004], show a small bright component (C) with a sharp edge near this position, suggesting a shock. Most of the radio emission comes from a region less than 30 mas in diameter. Our data, and the images from Gratadour et al. [2006] indicate that the dust emission comes from a much larger region, probably displaced from radio component C. In particular the MIDI data excludes a narrow ridge morphology that might be associated with a shock. This extended emission presumably arises from radiatively heated dust.

Wang et al. [2012] describe a similar scenario based on relatively high-resolution (300 mas) Chandra X-ray data. The X-ray and radio bright region HST-G about 1" north of the nucleus shows an X-ray spectrum containing both photoionized and high-density thermal components. Detailed X-ray spectra for the other X-ray components in the region are not available, but the ratio of [OIII] to soft X-ray continuum indicates that some (labelled HST-D, -E, and -F) are radiation heated, while others (HST-G, -H, and the near-nuclear regions HST-A, -B, and -C) contain shocked gas. The HST-A, -B, and -C regions contain the nucleus (to the extent not blocked by Compton scattering), our components 1, 2, and 3, and the Tongue. Unfortunately the spatial resolution of the X-ray and [OIII] data cannot distinguish between these sub-components. The very high-resolution VLBA data of Gallimore et al. [2004] show a flat-spectrum nuclear component, presumably coinciding with our component 1, but no emission at our positions 2 or 3. They find strong synchrotron emission at the Tongue and at their NE component, which curiously shows no enhanced X-ray, [OIII], or infrared emission. There are several regions (e.g., HST-D, E, F in Evans et al. 1991) that show X-ray, [OIII], and infrared emission, but where there is no sign of shock enhancement of the synchrotron jet [Gallimore et al., 2004]. Regions NE-5, 6, and 7 of Galliano et al. [2005b] show the same features. There is no evidence at these positions of direct interaction with the radio jet, although they lie at the edge of a radio cocoon [Wilson & Ulvestad, 1983].

This summary indicates the complexity of the region and suggests that different mechanisms dominate at different positions. The data from the Tongue region seems to support the shock plus radiative heating in this area. On the other hand, our region 3 shows no signature of shocks in the radio. This and the proximity to the nucleus favor heating by UV-radiation from the nucleus.

We can examine whether the infrared spectral information in the region is consistent with this hypothesis. The luminosity produced by the nucleus is sufficient to obtain the dust temperature measured at this position. The expected temperature of dust (assuming silicate grains) heated directly by the central engine is given by

$$T \simeq 1500 \left(\frac{L_{uv,46}}{r_{pc}^2} \right)^{\frac{1}{5.6}} \text{K}, \qquad (2.4)$$

where $L_{uv,46}$ is the luminosity of the heating source in units of 10^{46} erg s^{-1} [Barvainis, 1987]. For the central source of NGC 1068 we take the UV luminosity $L_{uv} = 1.5 \times 10^{45}$ erg s^{-1} previously used by Gratadour et al. [2003] to reproduce the central K-band flux and continuum. Dust at a distance of $r \sim 7$ pc (100 mas) can be heated to $T = 530$ K. The color temperatures in our wavelength range are lower (~ 400 K).

The spectra of the various infrared components show various, sometime quite high color temperatures, but it is difficult to use this to distinguish radiative from shock heating. The dust in the shock heated Tongue region shows short wavelength fluxes with color temperatures ~ 700 K [Gratadour et al., 2006], but some of the shortest wavelength data may represent scattered nuclear light rather than local thermal emission. The spatial resolution of the data in Gratadour et al. [2006] is not sufficient to unambiguously determine a short wavelength color temperature for our component 3. They report aperture fluxes for the non-deconvolved K-band image of the nucleus that increase from ~ 70 mJy at 80 mas radius to ~ 130 mJy at 130 mas radius and ~ 190 mJy at 270 mas. If we extrapolate our N-band flux of component 3 to the K-band with the same flux ratio as the Tongue region, it would have a flux of ~ 50 mJy, which is consistent with the fluxes just quoted. The speckle data in Weigelt et al. [2004] also give some indication of short wavelength radiation from our component, but the resolution is again marginal, and the same problem of scattered light exists. In conclusion, the infrared data do not exclude N- to K-band color temperatures up to ~ 700 K, which would be difficult to explain by radiative heating from the nucleus.

We anticipate that high-resolution interferometric mapping of NGC 1068 at 3 μm and 5 μm with the MATISSE interferometer [Lopez et al., 2008] will determine accurate infrared spectra for these regions and allow disentanglement of the thermal emission and scattering. Here we assume on the basis of the lack of radio emission in component 3 that it is heated radiatively by the nucleus. This component emits about 60 % of the near nuclear mid-infrared flux. Hence this structure must absorb most of the nuclear UV-emission. Thus, the dust that extinguishes the nuclear emission in this Seyfert 2 galaxy is not distributed in a disk- or torus-like structure, cloudy or otherwise, but in a narrow cylindrical or conical structure generally in the jet direction, which is, however, not symmetric around the jet. Müller-Sánchez et al.

[2011] similarly found that the coronal line ionization cone in NGC 1068 was also quite narrow. They estimate the half-opening angle to the north to be $\sim 27°$. If the simple unified models of Seyfert galaxies is in fact true, and the opening angles for viewing the direct emission from the nucleus were as small as that in NGC 1068, only about $10\,\%$ of Seyfert would be of Type 1, instead of the observed value of $\sim 50\,\%$. A spread in the values for the opening angles was earlier noted by studying the kinematics of the narrow line region using the HST [Fischer et al., 2013] and VLT/SINFONI [Müller-Sánchez et al., 2011], and for the case of NGC 1068 the relatively narrow opening angle of the ionization cone reported in both studies is in agreement with our observations. Thus, there is evidence for a large spread of the opening angles of AGNs, and that the actual difference between Types 1 and 2 may be more complicated than a simple inclination angle effect.

2.8.   The north/south asymmetry

It is noteworthy that the majority of the emission in the immediate circumnuclear neighborhood is highly asymmetric, lying to the north of the nucleus itself. This is the same side where most of the radio, near-infrared emission and optical ionization cone emission is seen. At shorter wavelengths, the asymmetry is usually attributed to foreground absorption from the inclined dust structure, but a similar mechanism in the mid-infrared requires very high dust opacities. If we suppose that an additional component identical to component 3 were present in the south, we would need several optical depths at $12\,\mu$m at a position 7 parsec south of the nucleus to obscure this component. This dust needs to be quite cold, i.e., $< 200\,$K, in order that its own emission not dominate our picture. A similar picture, but with lower forground opacity is presented by Tristram et al. [2013] for Circinus. In view of the complexity of this source, it cannot be ruled out that a cold cloud or disk structure at large radius extinguishes the southern infrared emission. This would not explain the north-south asymmetry of the radio emission, which may represent accidental circumstances of the interception of the jet by clouds.

Tristram et al. [2013] have found a similar picture in the Circinus galaxy. They find non-torus emission aligned with radio jet. The mid-infrared continuum emission is more or less symmetric in these regions, but the $10\,\mu$m silicate absorption is much stronger on the side where optical emission is missing. This may represent a case where the foreground dust thickness is enough to block the center of the silicate band, but not enough to absorb most of the N-band continuum. In this picture the dust column density in NGC 1068 would be at least three times higher, so that both the continuum and the silicate feature are blocked.

2.9.   Conclusions

We present new interferometric data from MIDI/VLTI using the Auxiliary Tele-
scopes that allow us to investigate the structure of the $5 - 10$ pc scale mid-infrared
nuclear emission from NGC 1068. Our observations complement the previous UT
interferometric observations, that trace the small-scales structures, and the single-
dish images of the extended region. The ATs, which have an effective area smaller
by a factor of ~ 20 than the UTs, were able to track fringes for NGC 1068 measuring
fluxes close to the limit of the instrument.

We summarize our results as follows:

- Fits using non-concentric Gaussian components indicate that most of the mid-
  infrared emission is attributed to the large-scale structures. This emission is
  associated with warm dust distributed in two major components, one close to
  the center and one with a distance larger than 80 mas and close to $16° - 18°$
  in the NW direction. The central warm region would mostly be seen as the
  extension of the hot emission region, while the offset region may be attributed
  to dusty clouds located close the northern ionization cone. The parameters
  found for this component indicate a size of ~ 14 parsec, strong elongation
  along a position angle of $\sim -35°$, and a contribution to the total flux at $12\,\mu$m
  which is more than three times that of the central hot region.

- The nonzero chromatic phases on the shorter baselines indicate major asym-
  metries in the emission on the 10 parsec scale, primarily along the north-south
  axis.

- The 3-Gaussian model does not fit well the intermediate baseline data, prob-
  ably because of the complexity of the structures in the equivalent size scales.
  This, combined with the limited information from the chromatic phases, leads
  to uncertainty in the description of the structures on equivalent scales. The dis-
  placement, size, and orientation of the large northern component is determined
  from the data at the shortest baselines, where the quality of the Gaussian fits
  is good.

- The low resolution picture derived from the Gaussian fits indicates that the
  near-nuclear (< 10 pc) emission is strongly asymmetric with respect to the
  nucleus, with the major components to the north agreeing in orientation with
  those seen in near-infrared NACO images. The north-south asymmetric may
  be caused by strong extinction of the southern components, or by intrinsic
  asymmetry of the dust components.

- The warm component 3, located ~ 7 parsec north of the hotter nuclear disk,
  apparently intercepts a large fraction of the nuclear UV emission. Thus there

are several obscuring components at different disk latitudes that can cause Seyfert 2 appearance in AGNs. The volume that is heated by this emission is quite narrow; the viewing angles from which this galaxy would be classified as Seyfert 1 cover only $\sim 10\,\%$ of the sky.

- We do not observe evidence for variability effects in the mid-infrared emission of the small-scales structures in the nuclear region of NGC 1068. Similar (u, v) points observed with a difference of 7 years do not show significant differences (less than $10\,\%$).

- Independently calibrated observations with the ATs over periods of several days show a high level of repeatability.

2.10.   Appendix

2.10.1.   Plots of UT Data and LOG of observations
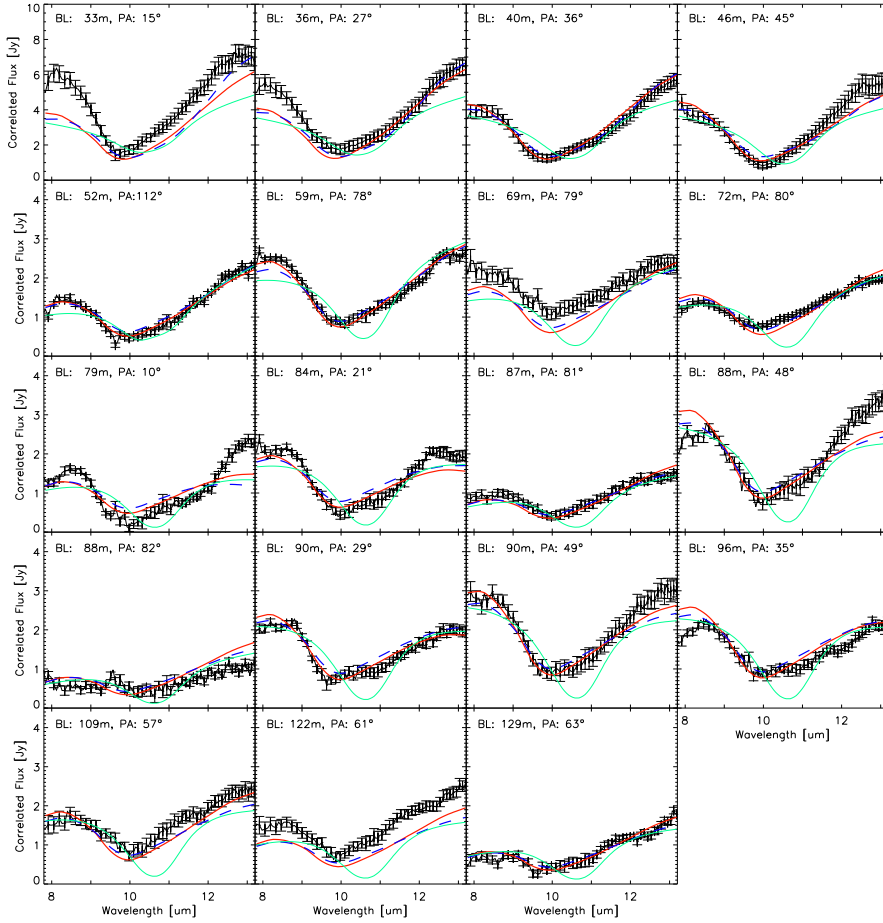
Figure 2.9: *Correlated fluxes of observations taken with UTs. The red and dashed blue lines are the curves obtained with our first and second best-fit models. The light blue curve shows the correlated fluxes of our best-fit model found using SiC as the dust template for all the components. We observe that the main reason of discarding SiC as the best option is mostly due to the shape of the absorption feature.*

Figure 2.10: *The same as Fig. 2.9, but chromatic phases are plotted instead of correlated fluxes.*

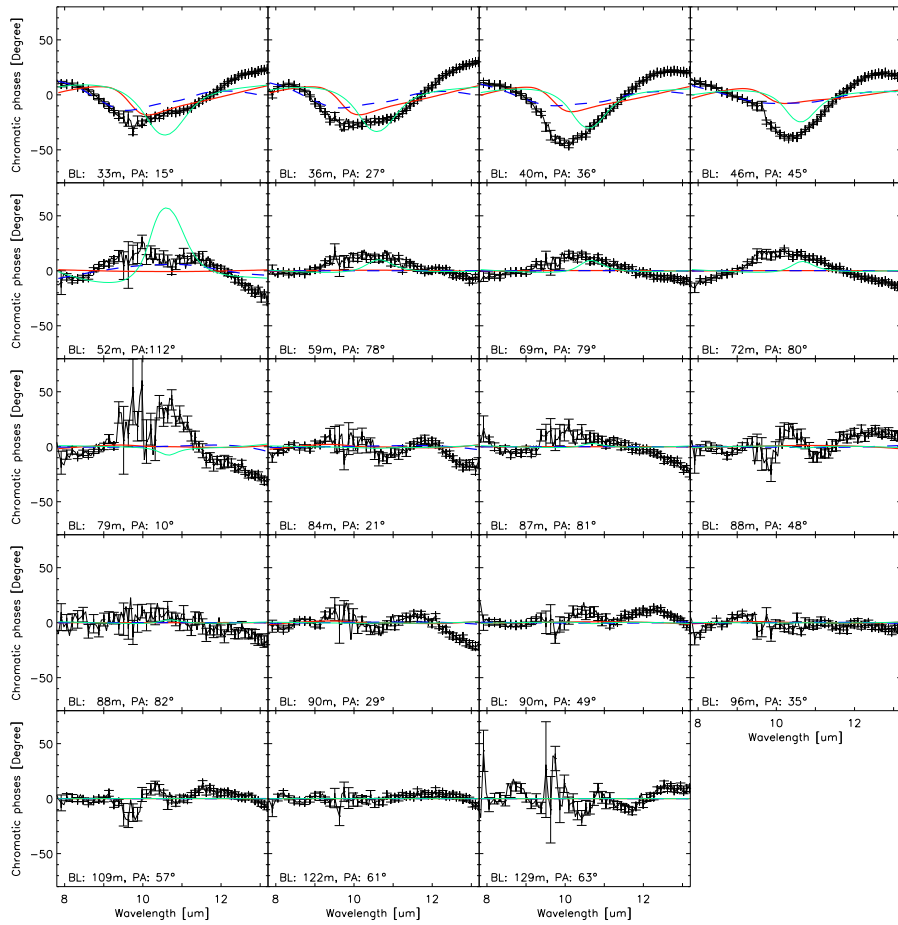| Time	BL [m]	PA [deg]	Calibrator	Caltime	Airmass	Seeing	OK?	St	Group
2007-10-07: E0G0									
06:04:14	15.7	72.4	HD10380	06:37:22	1.1	2.0	1	1	3
06:08:04	15.8	72.5	HD10380	06:37:22	1.1	2.0	1	0	3
07:06:35	16.0	72.7	HD10380	06:37:22	1.1	1.7	1	1	3
07:10:28	16.0	72.7	HD10380	06:37:22	1.1	1.9	1	0	3
08:09:51	15.1	71.8	HD10380	07:45:02	1.2	1.9	1	1	3
08:13:45	15.1	71.7	HD10380	07:45:02	1.3	2.1	1	0	3
08:52:57	14.0	70.2	HD18322	09:18:41	1.4	1.7	1	1	3
08:56:48	13.9	70.0	HD18322	09:18:41	1.4	1.7	1	0	3
09:37:35	12.3	67.4	HD18322	09:18:41	1.7	1.4	0	-	-
2007-10-08: G0H0									
05:09:01	29.4	71.2	HD10380	04:34:38	1.1	1.3	1	0	7
05:13:07	29.6	71.3	HD10380	05:48:11	1.1	1.2	1	1	7
05:17:10	29.8	71.5	HD10380	05:48:11	1.1	1.1	1	1	7
05:21:25	30.0	71.6	HD10380	05:48:11	1.1	1.1	1	0	7
06:12:14	31.7	72.6	HD10380	05:48:11	1.1	1.5	1	1	8
06:15:59	31.7	72.7	HD10380	05:48:11	1.1	1.6	1	0	8
06:20:58	31.8	72.7	HD10380	06:45:43	1.1	1.7	1	1	8
06:31:48	31.9	72.8	HD10380	06:45:43	1.1	1.8	1	0	8
07:03:08	31.9	72.8	HD10380	06:45:43	1.1	1.7	0	-	-
07:07:36	31.9	72.7	HD10380	06:45:43	1.1	1.7	1	1	8
07:11:30	31.8	72.7	HD10380	06:45:43	1.1	1.7	1	0	8
07:15:16	31.8	72.7	HD10380	07:44:12	1.1	1.6	1	1	8
07:19:22	31.7	72.6	HD10380	07:44:12	1.1	1.4	1	0	8
08:01:29	30.5	71.9	HD10380	07:44:12	1.2	1.0	1	1	7
08:05:26	30.3	71.8	HD10380	07:44:12	1.2	0.9	1	0	7
08:09:10	30.1	71.7	HD10380	08:28:09	1.3	1.0	0	-	-
08:12:56	30.0	71.6	HD10380	08:28:09	1.3	1.0	1	0	7
08:16:46	29.8	71.5	HD10380	08:28:09	1.3	1.0	0	-	-
08:57:45	27.4	69.8	HD18322	09:24:25	1.5	0.8	1	1	7
09:01:38	27.1	69.6	HD18322	09:24:25	1.5	0.9	1	1	7
09:05:35	26.8	69.4	HD18322	09:24:25	1.5	0.8	1	0	7
2012-09-19: I1K0									
07:43:13	42.9	15.0	HD10380	07:29:15	1.1	0.9	1	0	10
08:01:30	43.3	16.8	HD18322	07:52:50	1.1	1.0	1	0	10
08:05:16	43.4	17.2	HD18322	08:16:55	1.1	1.1	1	1	10
08:09:03	43.5	17.5	HD18322	08:16:55	1.1	1.0	1	1	10
08:25:04	43.8	18.9	HD18322	08:16:55	1.1	0.8	1	0	10
08:29:02	43.9	19.3	HD18322	08:16:55	1.1	0.7	0	-	-
08:36:16	44.1	19.9	HD18322	08:43:39	1.2	0.7	1	1	11
08:50:25	44.4	21.0	HD18322	08:43:39	1.2	0.7	1	1	11
08:52:46	44.5	21.2	HD18322	08:43:39	1.2	0.7	1	1	11

Table 2.2: *Log of observations: NGC 1068. The columns are:* **Time** *of fringe track observation;* **BL** *projected baseline length;* **PA** *position angle; name of the* **Calibrator***; Time of the calibrator fringe track observation,* **Airmass** *of fringe track;* **Seeing** *during fringe track observation;* **OK?** *Goodness of observation (good:1, bad:0);* **St** *Stacked with the following observation (yes:1, no:0);* **Group** *Corresponding group according to criterion of Sect. 2.4.1.*

Time	BL [m]	PA [deg]	Calibrator	Caltime	Airmass	Seeing	OK?	St	Group
2012-09-19: I1K0									
08:55:14	44.5	21.3	HD18322	08:43:39	1.2	0.6	1	0	11
08:57:31	44.6	21.5	HD18322	09:07:06	1.2	0.6	1	1	11
08:59:48	44.6	21.7	HD18322	09:07:06	1.2	0.6	1	0	11
2012-09-20: G1I1									
06:01:26	39.8	35.3	HD10380	05:51:28	1.2	0.8	1	0	9
06:04:53	40.0	35.8	HD10380	06:16:38	1.2	0.8	1	1	9
06:08:31	40.2	36.2	HD10380	06:16:38	1.2	0.9	1	1	9
06:25:07	41.2	38.0	HD10380	06:16:38	1.1	0.9	1	0	9
06:28:35	41.4	38.4	HD10380	06:39:43	1.1	1.0	1	1	9
06:32:00	41.6	38.7	HD10380	06:39:43	1.1	1.0	1	0	9
2012-09-24: C1D0									
04:28:29	18.6	7.0	HD10380	04:20:28	1.4	0.5	1	0	4
04:32:01	18.6	7.6	HD10380	04:39:44	1.4	0.5	1	1	4
04:51:21	18.8	10.8	HD10380	04:39:44	1.3	0.6	1	0	4
04:54:55	18.9	11.4	HD10380	05:03:59	1.3	0.6	1	0	4
2012-09-24: B2D0									
05:37:00	29.1	17.8	HD10380	05:29:55	1.2	0.6	1	0	6
05:40:32	29.2	18.3	HD10380	05:48:33	1.2	0.6	1	1	6
05:55:07	29.6	20.3	HD10380	05:48:33	1.2	0.6	1	0	6
05:58:42	29.7	20.8	HD10380	06:06:23	1.2	0.5	1	0	6
2012-09-24: B2C1									
06:28:04	10.1	24.3	HD10380	06:20:35	1.1	0.6	1	0	1
06:32:04	10.2	24.8	HD10380	06:39:50	1.1	0.6	1	0	1
06:53:17	10.4	27.0	HD10380	07:04:27	1.1	0.6	1	1	1
06:56:48	10.4	27.3	HD10380	07:04:27	1.1	0.6	1	0	1
2012-09-25: A1B2									
06:35:55	11.3	113.5	HD10380	06:47:45	1.1	0.8	1	1	2
06:39:43	11.3	113.5	HD10380	06:47:45	1.1	0.7	1	0	2
06:59:49	11.1	113.8	HD10380	07:10:26	1.1	0.7	1	1	2
07:03:20	11.1	113.9	HD10380	07:10:26	1.1	0.7	1	0	2
2012-09-25: B2C1									
07:34:39	10.7	30.8	HD18322	07:28:07	1.1	0.6	1	0	1
07:38:25	10.8	31.0	HD18322	07:46:10	1.1	0.7	1	1	1
07:51:59	10.9	31.9	HD18322	07:46:10	1.1	0.9	1	0	1
07:55:31	10.9	32.1	HD18322	08:03:51	1.1	0.9	1	0	1
2012-09-25: C1D0									
08:21:07	22.2	33.5	HD18322	08:15:06	1.2	0.6	1	0	5
08:25:38	22.2	33.6	HD18322	08:35:25	1.2	0.6	0	-	-
08:27:22	22.2	33.7	HD18322	08:35:25	1.2	0.7	1	1	5
08:41:52	22.4	34.2	HD18322	08:35:25	1.2	0.7	1	1	5
08:45:34	22.4	34.4	HD18322	08:35:25	1.2	0.7	1	0	5
09:05:55	22.5	34.9	HD18322	09:00:33	1.3	0.7	1	0	5
09:10:13	22.5	35.0	HD18322	09:17:09	1.3	0.7	1	1	5
09:27:40	22.6	35.2	HD18322	09:17:09	1.4	0.7	1	0	5
09:30:02	22.6	35.2	HD18322	09:40:12	1.4	0.6	1	1	5
09:32:10	22.6	35.2	HD18322	09:40:12	1.4	0.7	0	-	-
09:34:20	22.6	35.2	HD18322	09:40:12	1.4	0.7	1	0	5

Table 2.2: — continued

CHAPTER 3

Mid-infrared interferometry of 23 AGN tori: On the significance of polar-elongated emission

N. López-Gonzaga, L. Burtscher, K. R. W. Tristram, K. Meisenheimer, M. Schartmann

Astronomy and Astrophysics, in press (2016)

Abstract

Detailed high-resolution studies of active galactic nuclei (AGN) with mid-infrared (MIR) interferometry have revealed parsec-sized dust emission that is elongated in the polar direction in four sources. Using a larger, coherently analyzed sample of AGN observed with MIR interferometry, we aim to identify elongated MIR emission in a statistical sample of sources. More specifically, we wish to determine if there is indeed a preferred direction of the elongation and whether this direction is consistent with a torus-like structure or with a polar emission. We investigated the significance of the detection of an elongated shape in the MIR emission by fitting elongated Gaussian models to the interferometric data at $12\,\mu$m. We paid special attention to (1) the uncertainties caused by an inhomogeneous (u, v) coverage, (2) the typical errors in the measurements, and (3) the spatial resolution achieved for each object. From our sample of 23 sources, we are able to find elongated parsec-scale, MIR emission in five sources: three type 2s, one type 1i, and one type 1. Elongated emission in four of these sources has been published before; NGC 5506 is a new detection. The observed axis ratios are typically around 2 and the position angle of the $12\,\mu$m emission for all the elongated sources always seems to be closer to the polar axis of the system than to the equatorial axis. Two other objects, NGC 4507 and MCG-5-23-16, with reasonably well-mapped (u, v) coverage and good signal-to-noise ratios (SNR), appear to have a less elongated $12\,\mu$m emission. Our finding that sources showing elongated MIR emission are preferentially extended in polar direction sets strong constraints on torus models or implies that both the torus and NLR/outflow region have to be modeled together. In addition, models used for SED fitting will have to be revised to include emission from polar dust.

3.1.   Introduction.

In active galactic nuclei (AGN), a dusty toroidal structure is thought to be responsible for obscuring our line of sight onto the accreting super massive black hole (SMBH) for some inclination angles. Obscured ("type 2") AGNs, where only relatively narrow ($\lesssim 1000\,\mathrm{km/s}$) forbidden emission lines are seen and unobscured ("type 1") AGNs, which also show broad ($> 1000\,\mathrm{km/s}$) permitted lines are then unified to the same class of objects simply by orientation [Antonucci & Miller, 1985; Antonucci, 1993; Urry & Padovani, 1995]. This circum-nuclear dust, usually referred to as the "dusty torus", absorbs a fraction of the optical and UV light and re-emits the energy in the infrared regime. The infrared bands are therefore a suitable window to analyze the structure of this dusty region.

Infrared observations at the diffraction limit of $10\,\mathrm{m}$ class telescopes ($\sim$300 mas resolution) allow us to isolate the emission of the circum-nuclear dust spatially from the surrounding starburst emission, but these observations do not usually resolve the structure of the torus [e.g., Siebenmorgen et al., 2008; Raban et al., 2008; Gandhi et al., 2009; Reunanen et al., 2010; Horst et al., 2009; Ramos Almeida et al., 2009, 2011; Asmus et al., 2011; Mason et al., 2012]. Asmus et al. [2014] only detected extended emission on arcsecond scales in some 18% of objects. In those cases, Asmus et al. [2014] found that the extended emission usually coincides with the position angle (PA) of the narrow line region (NLR), supporting the view that warm dust exists there [see also Schweitzer et al., 2008].

In recent years, infrared interferometry became an important tool to observe the dusty nuclear regions of AGNs. With a resolution that can easily be more than ten times better than that of a single-aperture telescope, this technique has allowed to resolve the cores of more than two dozen AGNs by now [e.g., Jaffe et al., 2004; Kishimoto et al., 2009a,b; Tristram et al., 2009; Burtscher et al., 2013]. The analysis of the entire sample has shown that the mid-infrared (MIR) emission comes from a region about $4-20$ times larger than the sublimation radius of dust, but also that the sample is very diverse in the sense that the size and structure is different in each object. To the extent that this allows for statements about the average, no differences between type 1 and type 2 AGNs have been found. For details, we refer to Burtscher et al. [2013], hereafter B13.

Previous interferometric studies of individual objects [e.g., Raban et al., 2009; Hönig et al., 2012, 2013; Tristram et al., 2014; López-Gonzaga et al., 2014], on the other hand, are often able to resolve not only the basic structure, i.e., size and number of components, but also constrain the shape of the resolved emission. In the four objects that have been studied in detail, the dusty emission is always found along the polar direction rather than in an azimuthal configuration as one may naively expect from simple torus pictures [Antonucci & Miller, 1985].

The aim of this work is to coherently analyze the interferometric data of the MIDI AGN Large Programme (LP) sample (B13) to identify intrinsic elongations in the MIR emission of the dusty region of the entire sample. The outline of this paper is the following: Section 3.2 includes a brief explanation of the AGN sample and the interferometric data. In Sect. 3.3 we explain our geometric model and the procedure followed to fit and identify candidates with elongations. Our results are presented and discussed in Sect. 3.4. We summarize our results in Sect. 3.5.

3.2. The AGN sample, observations, and data processing

Here we use the sample first presented in B13. It consists of the MIDI AGN Large Programme and all other extragalactic MIR observations publicly available until the time of publishing. These are 23 AGN, all observed with the MID-infrared interferometric Instrument [MIDI; Leinert et al., 2003] at the European Southern Observatory's (ESO's) Very Large Telescope Interferometer (VLTI) on Cerro Paranal, Chile. The classical Michelson interferometer MIDI combines the beams of two telescopes at a time in the atmospheric N band, i.e., the wavelength region $8-13\,\mu$m. As a result of the high background in the thermal infrared (exacerbated by ~ 20 reflections along the VLTI optical train), severe flux limits apply. Our sample is therefore essentially flux-selected among the brightest and most well-known AGNs. It includes 12 type 1, nine type 2 Seyfert galaxies, one radio galaxy, and a quasar, with a median luminosity distance of $53\,$Mpc. For this work, we additionally collect the published data for the Circinus galaxy [Tristram et al., 2014], NGC 1068 [López-Gonzaga et al., 2014], and NGC 3783 [Hönig et al., 2013], which are three galaxies whose interferometric data showed clear signs of elongated emission. For details about the observation sequence and data reduction, we refer to Burtscher et al. [2012].

All sources were observed with pairs of $8\,$m Unit telescopes (UTs) in at least three different baseline configurations. Additionally, for the two brightest and closest AGNs, Circinus and NGC 1068, observations were also carried out using configurations with the 1.8 m Auxiliary Telescopes (ATs) to cover shorter baselines. These two sources are almost completely resolved out in the interferometric data, while in the other galaxies less than $60\,\%$ of the flux is resolved out. The reason is that the relative resolution, with respect to the dust sublimation radius, is much higher in these two galaxies than for the rest of the sources in the sample. We, therefore, only use the interferometric data obtained from projected baselines $< 40\,$m for the two bright sources to achieve a sample with homogeneous spatial resolution (in multiples of the innermost radius of dust).

The instrument MIDI also provides limited spectral information in the N band.

This information can be used to study several physical properties of the torus, such as temperature profiles or the nature of the silicate feature. As the purpose of our study is to investigate the general geometrical shape of the continuum MIR emission, we restrict ourselves to the $12\,\mu$m (rest-frame) fluxes, following B13. At this wavelength, the sources are best resolved and observations are least affected by instrumental and calibration errors, such as correlation losses, the silicate feature, or atmospheric absorption.

The lack of true phase information from the instrument and the sparse (u, v) coverage due to the time-consuming observations, do not allow us to apply image reconstruction techniques. Instead, we can only forward model simple geometrical brightness distributions and compare them with the observed visibilities. These models need to be kept as simple as possible to avoid degeneracies. While the true brightness distribution of the objects might be relatively complex, it has been shown that simple analytical surface brightness distributions, such as Gaussian or uniform disks, can be used to provide a first order approximation of the shape and size and serve as building blocks for more complex geometries [see, e.g., Jaffe et al., 2004; Poncelet et al., 2006; Burtscher et al., 2009, 2013].

3.2.1. Averaging adjacent (u, v) points

Before modeling the interferometric data, we replaced measurements of adjacent (u, v) points with a weighted average. According to López-Gonzaga et al. [2014], if the size of the emission is smaller or similar to the resolution of the single-aperture telescope, measurements taken with adjacent (u, v) points should not vary too much if the distance Δu between them is $\Delta u \lesssim$ D, where D is the diameter of the telescope. Since all of our objects are essentially unresolved with the single-aperture telescope, we average (u, v) points with $\Delta u \lesssim 8\,$m, except for NGC 1068 and Circinus, where we use a $\Delta u \lesssim 1\,$m as they were observed with the ATs and show significant extension at arcsecond resolutions.

Points within a distance Δu from each other are averaged together using their corresponding uncertainty as a weight. Because the actual changes over the (u, v) plane in terms of correlated flux are small compared to our measurement error, we can assume that the differences in adjacent points is mostly dominated by noise. The averaging process not only serves to obtain more precise visibilities, but it also serves as a way of rebinning the (u, v) plane to reduce the nonuniform sampling.
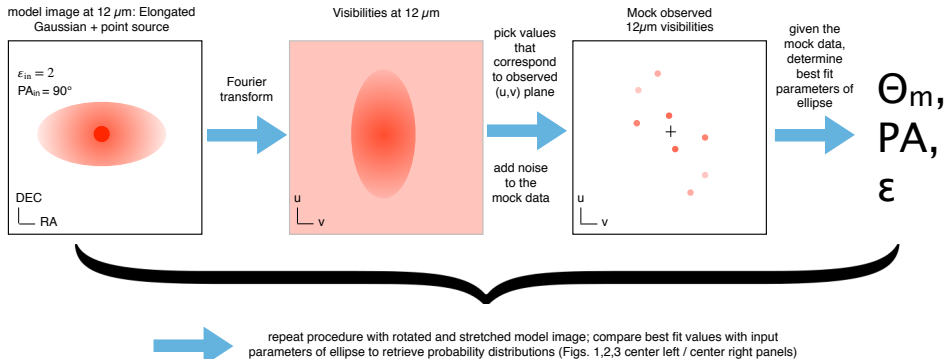
Figure 3.1: *Outline of the test setup to determine the reliability of our model fit for each source. First, we generate a simple model image (left panel) consisting of a point source and an elongated Gaussian of arbitrary axis ratio and position angle. Since the intensity of the point source is largely model independent and well constrained by the observations, its visibility can be set to the actual value of the respective source. Next, this image is Fourier transformed (center left). From these model visibilities we take the values that correspond to the actually observed (u, v) coverage for the specific source (center right panel). After adding appropriate noise, we fit the mock data set with our three-parameter fit (minor axis FWHM θ_m, position angle PA, and axis ratio ϵ) and compare the result with the known input parameters. This procedure is repeated for different axis ratios and position angles and for the specific (u, v) coverage of each source.*

3.3.   Finding elongations

3.3.1.   Elongated model

Previous results from B13 using symmetric distributions, allowed us to determine an average size of the infrared emission for the AGN tori of our sample. However, from the residual plots in Figures $5-27$ of B13 it was already clear that, for some objects, the data contain more information about the shape than just an average size.

The $12\,\mu$m emission of the large program sources observed with MIDI can be described with one or two components: 1) an unresolved emission and sometimes 2) an (over-)resolved component. For every object, the level of unresolved emission (the minimum visibility of point source fraction) is well determined even without any model fitting in most of the sources (see B13), this emission is best described by a point source distribution. If there is evidence for a second component, we can describe it by using an elongated Gaussian component as we did for this work (the circular Gaussian component used in B13 is a particular case of the elongated model).

The correlated fluxes are defined by the following equation:

$$F_{corr}(u, v) = (F_{tot} - F_{pt})V_{gs}(u, v) + F_{pt}, \qquad (3.1)$$

where F_{corr} is the correlated flux, F_{tot} is the total flux measured by the single-aperture telescope, F_{pt} is the flux of the point source, and V_{gs} is the visibility of the elongated Gaussian distribution. The elongated Gaussian distribution is defined by three parameters: the full width at half maximum (FWHM) of the minor axis (θ_m), an axis ratio $\varepsilon = \Theta_M/\theta_m$ defining the ratio between the FWHM of the major axis (Θ_M) and the FWHM of the minor axis (θ_m), and the position angle (PA) of the major axis measured in degrees from east of north.http://www.espnfc.us/scores The analytical description of the correlated fluxes is given by the following formula:

$$V_{gs}(u,v) = \exp\left[-\frac{\left(\pi\,\theta_m\sqrt{u'^2 + \varepsilon^2 v'^2}\,\right)^2}{4\ln 2}\right],\qquad(3.2)$$

where $u' = u\cos(PA) - v\sin(PA)$, $v' = u\sin(PA) + v\cos(PA)$. For most of our objects, the total $12\,\mu$m flux has a relatively low uncertainty, so we ignore this error and in the following we consider the total single-aperture flux as a fixed quantity and treat the correlated fluxes as visibilities.

3.3.2. Reliability of model fits. The role of the (u,v) coverage

Using interferometric measurements to constrain a possibly elongated shape of the emission is not straightforward if the (u,v) coverage is very sparse and inhomogeneous. Beam effects can easily dominate the shape of the reconstructed model image.

Therefore, we need to investigate the influence of the (u,v) coverage in the final determination of the axis ratio and position angle. For this, we set up a series of specific tests to assess the reliability of our fitting routines given the actual (u,v) coverage of every object and the noise levels and known minimum visibility (see Fig. 3.1 for an outline).

For this experiment, we first create models of elongated Gaussians with a few specified axis ratios and all possible position angles ($0-180\,°$ in $0.5\,°$ steps). We set the major axis FWHM such that this component is marginally resolved ($30\,\%$) at the shortest observed baselines. We also explored different size scales for the minor axis FWHM ($15\,\%$, $60\,\%$) and the results regarding the reliability of the fit do not change significantly. For this experiment, we include a point source to the model image with the known parameters. This is important since elongated emission is much easier to detect if the source is well-resolved than if the source is largely unresolved.

We then compute the Fourier transform of this model image and 'observe' the model ten times by taking the visibilities at the same (u,v) positions as the actual observations and adding Gaussian noise to the modeled data so that they are of the same signal-to-noise ratio (SNR) as the actual data. We apply our fitting routines on
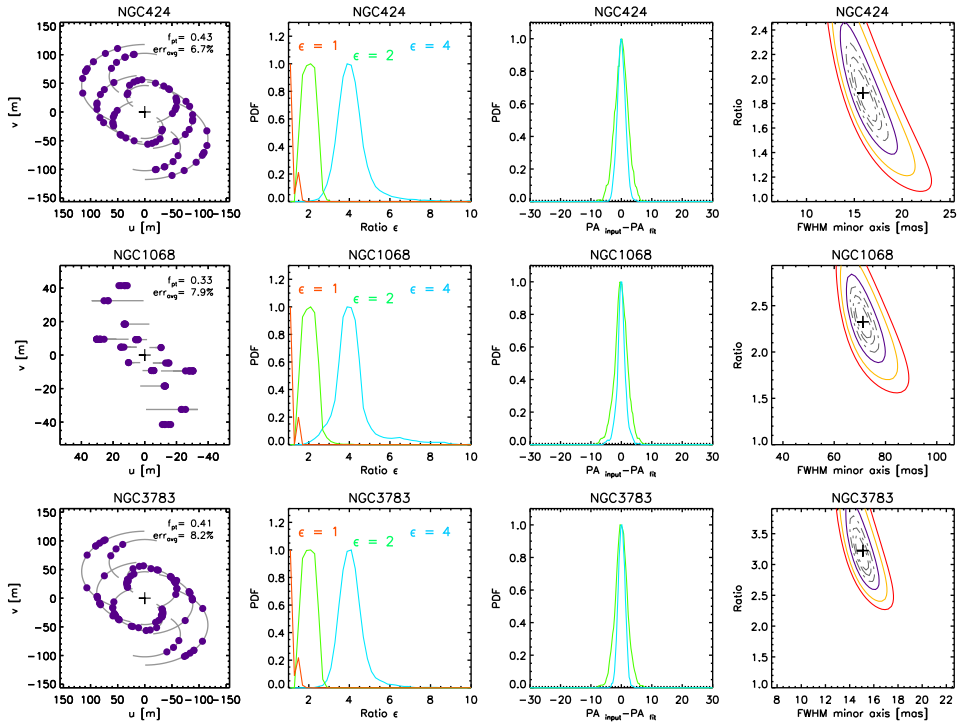
Figure 3.2: *Results of our reliability analysis for sources where an elongation should be detectable given the observed (u, v) coverage, signal-to-noise ratio and minimum visibility.*

First column: (u, v) coverage of the object. The point source fraction (f_{pt}) and typical uncertainty of the interferometric measurements (err_{avg} in percentage) are given for every object.

Second column: Probability density function of the axis ratio for three different input axis ratios: $\epsilon = 1$ in red, $\epsilon = 2$ in green, and $\epsilon = 3$ in blue. For visualization purposes, we normalized the maximum value of the PDF's to a value of one.

Third column: Probability density function of the recovered position angle of the major axis minus the input position angle. The colors are the same as for the second column. Intentionally, we do not plot the resulting PDF for an input axis ratio equal to 1.

Fourth column: Two-dimensional confidence interval for the axis ratio and FWHM of the minor axis from the fits using data from actual observations. The 1-σ, 2-σ, and 3-σ region are delimited by purple, orange, and red lines, respectively.
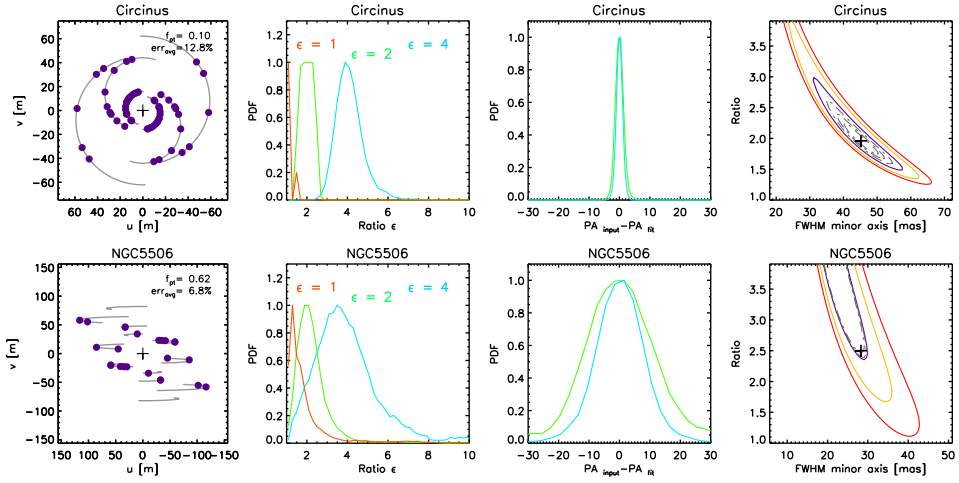
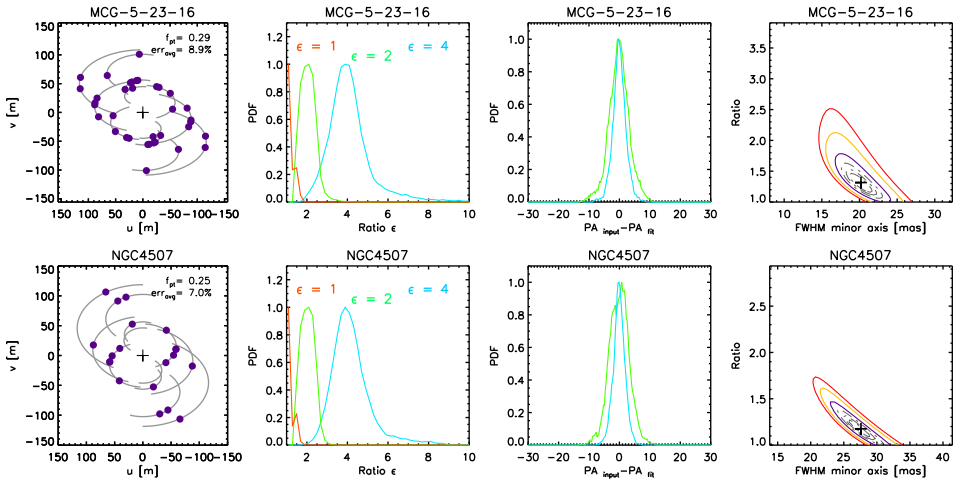**Figure 3.2:** — continued

Figure 3.3: *Similar to Fig. 3.2, but for sources where the mid-infrared emission is consistent with a nearly circular shape.*

these mock observations to derive the best-fit parameters and repeat this experiment for all sources.

As a last step, we compare the best-fit values of axis ratio and position angle with the known model input values and plot the probability of retrieving the correct axis ratio and input position angle for the different realizations of our model image. The (u, v) coverage, the probability density function (PDF) of the axis ratio, and the PDF of the position angle from this experiment are shown for every source in Figs. 3.2, 3.3, and 3.4 along with the χ^2 plane of the fit to the actual data.

These figures allow us to judge for each source the significance of the result of our model fit. As a (somewhat arbitrary) distinction between the reliable (Fig. 3.2 and Fig. 3.3) and less reliable (Fig. 3.4) objects we use as a criterion whether the data would allow us to discriminate between a round source ($\epsilon = 1$) and an elongated source with an axis ratio of 2. This can be easily read off from the center-left plot for each source: If the PDFs for the round ($\epsilon = 1$) and the $\epsilon = 2$ model source do not overlap at 1σ (68.3 %), we consider this set of observations as a reliable means of detecting elongated emission.

The results from this experiment can be summarize as follows:

1) We cannot recover reliable axis ratios or position angles for objects with an (u, v) coverage that consists of measurements along essentially two directions (e.g., ESO 323-77, NGC 5995, see Fig. 3.4) or if the extended emission is over-resolved (e.g, NGC 5128, see Fig. 3.4).

2) It is also not possible to determine the axis ratio or position angle for objects with a point source fraction above 70 % and with typical uncertainties of about 10 % (e.g, NGC 3218, see Fig. 3.4).

3) The position angle can be determined well for the objects shown in Figs. 3.2 and 3.3, in these objects the (u, v) coverage has precise measurements along three or more well-spaced directions in the (u, v) plane. We observe from their respective PDFs that for any direction, the position angle can be recovered with an accuracy of about $10°$.

We only need to test the reproducibility of the axis ratio test to decide whether we can recover elongated emission since all sets of observations with fully recoverable axis ratios also have well-defined position angles, while the inverse is not true.

3.4.   Results and discussion

Based on our reliability analysis (Sec. 3.3.2) and Figs. 3.2 and 3.3, we find seven sources where the existing observations would allow us to reliably detect elongated emission. For these sources, we give the best-fitting parameters for the elongated Gaussian model fits together with auxiliary data in Table 3.1.
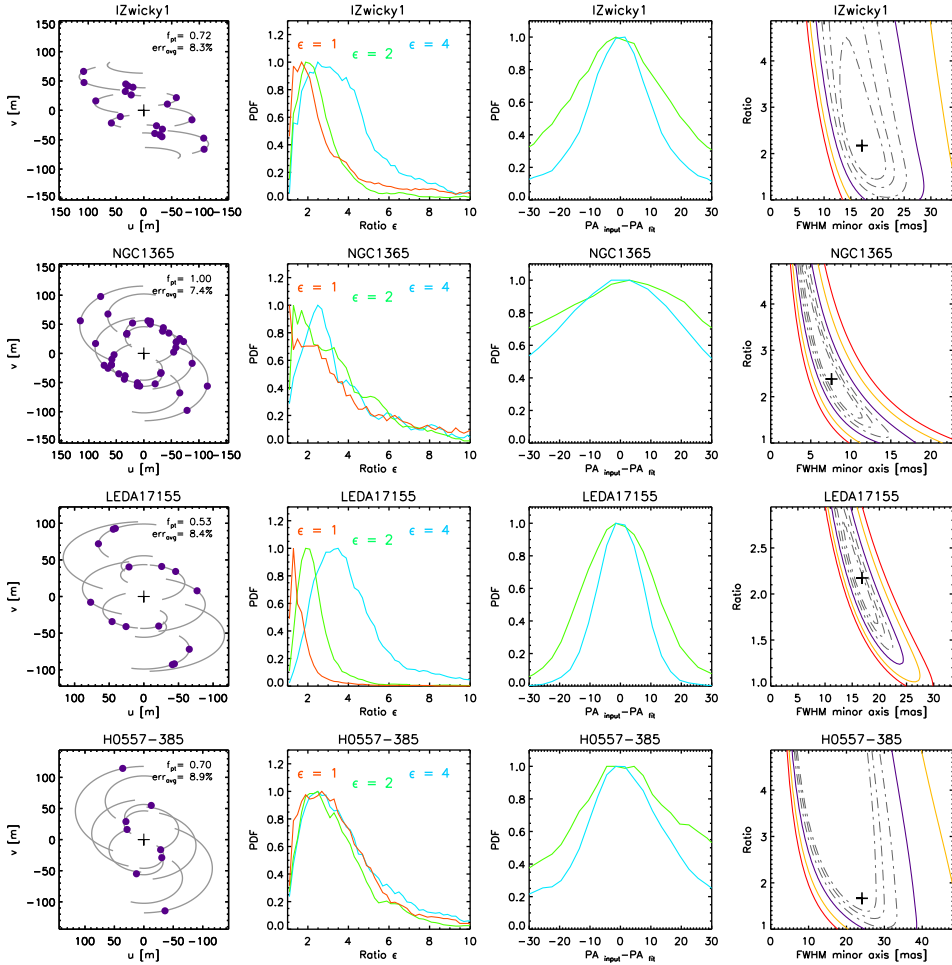
Figure 3.4: *Like Fig. 3.2, but for sources where an elongation is not reliably detectable owing to either bad (u, v) coverage, low signal-to-noise ratio or high minimum visibility (or a combination of these factors).*
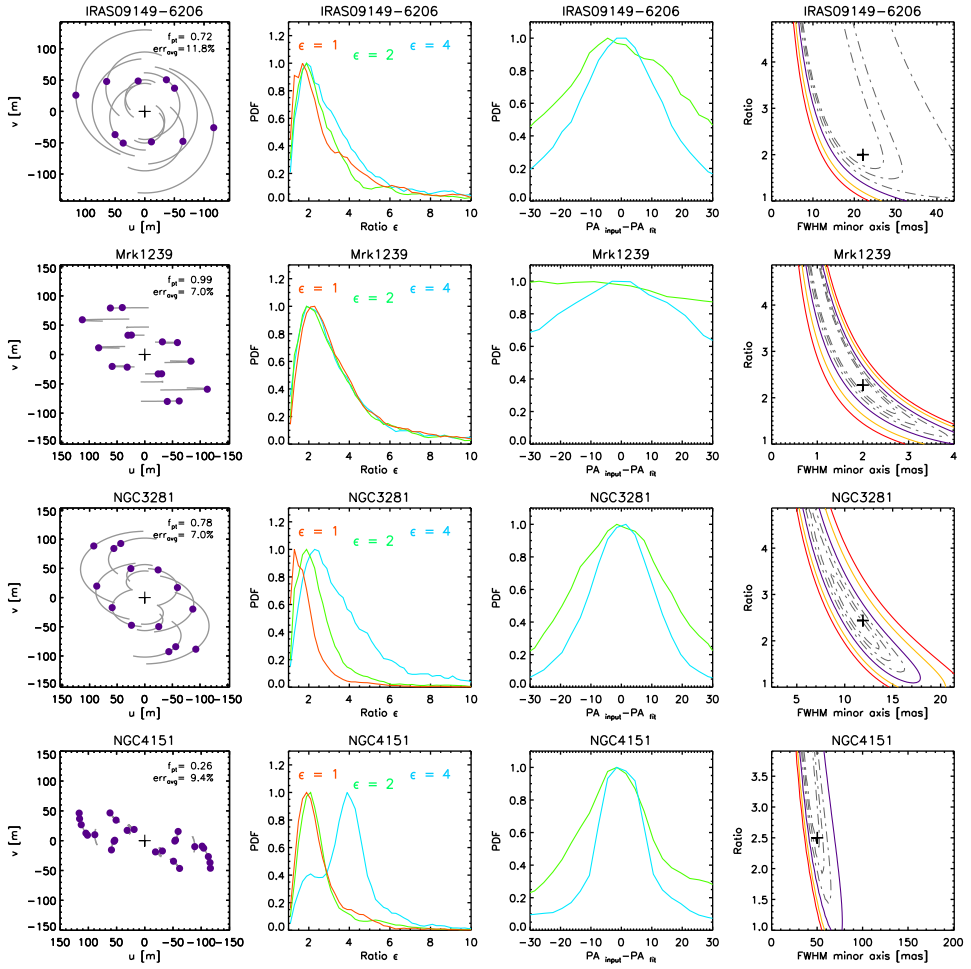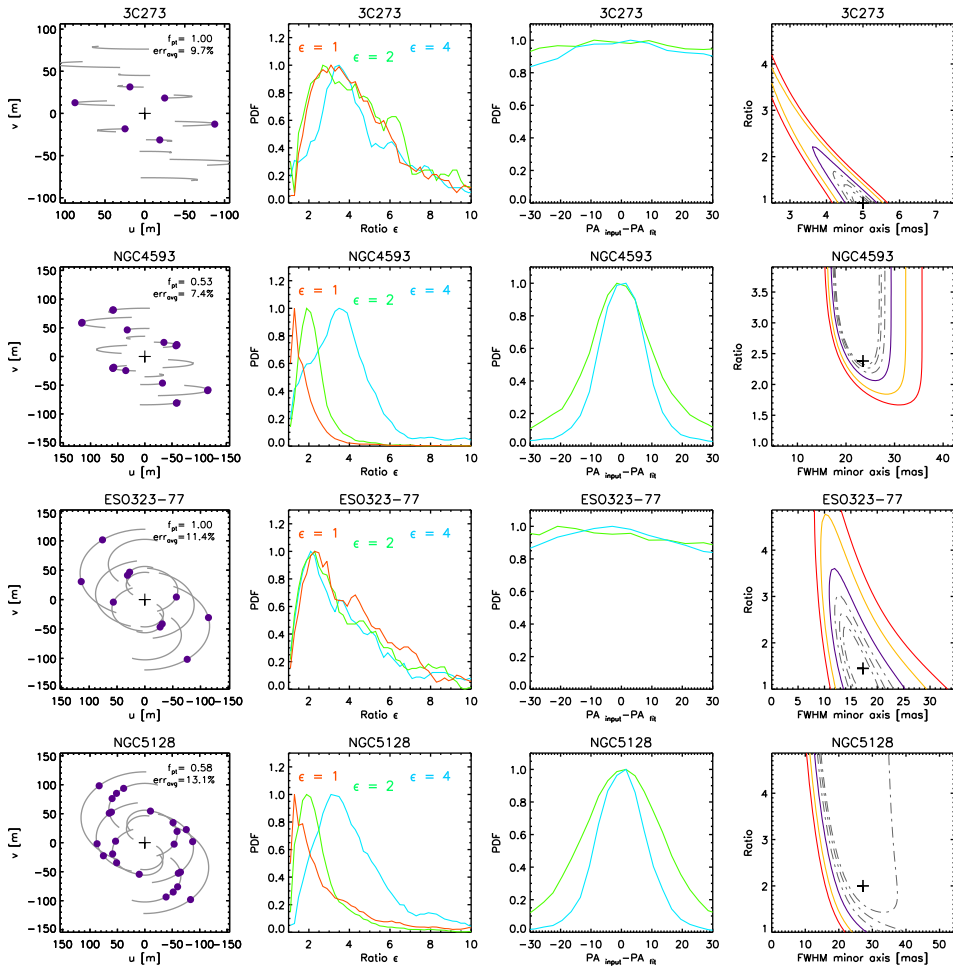
Figure 3.4: — continued
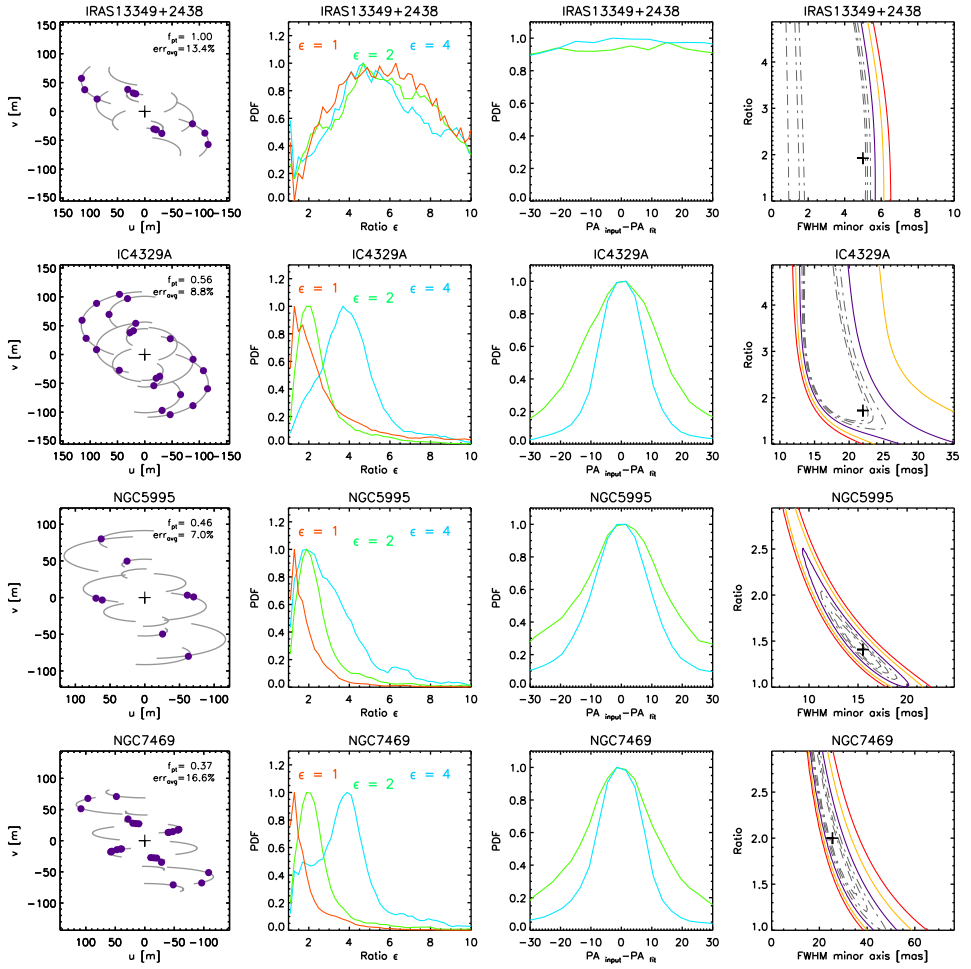
Figure 3.4: — continued

Figure 3.4: — continued

| Source | F_{pt} [Jy] | Parameters of best-fit model | | | | | PA | | |
		minor axis θ_m [mas]	PA [°]	Ratio $\epsilon = \Theta_M/\theta_m$	F_{gs} [Jy]	χ^2_{red}	Polar axis [°]	NLR [°]	Radio jet [°]
				ELONGATED					
NGC 424	0.30 ± 0.01	$15.9^{+3.9}_{-2.6}$ $(3.4^{+0.8}_{-0.6})$	157.4 ± 5.4	$1.9^{+0.6}_{-0.5}$	0.35 ± 0.01	3.13	133 [a]	-	unresolved [e]
NGC 1068	5.23 ± 0.19	$71.2^{+10.4}_{-6.0}$ $(5.0^{+0.7}_{-0.4})$	155.8 ± 2.9	$2.3^{+0.7}_{-0.5}$	10.81 ± 0.19	6.53	5 [b]	30 [c]	0 [d]
NGC 3783	0.19 ± 0.01	$15.7^{+1.3}_{-1.3}$ $(3.2^{+0.3}_{-0.3})$	119.9 ± 3.6	$3.1^{+0.8}_{-0.6}$	0.49 ± 0.01	3.5	135 [b]	160 [c]	unresolved [d,g]
Circinus	1.01 ± 0.11	$47.6^{+13.1}_{-15.0}$ $(1.0^{+0.2}_{-0.3})$	106.6 ± 2.4	$1.9^{+1.1}_{-0.4}$	9.08 ± 0.11	2.41	135 [b]	128 [c]	115 [f]
NGC 5506	0.57 ± 0.01	$28.6^{+3.9}_{-9.4}$ $(4.0^{+0.5}_{-1.3})$	8.3 ± 9.0	$2.5_{-0.4}$	0.47 ± 0.01	3.18	163 [b]	22 [c]	155 [h]
				NEARLY CIRCULAR					
MCG-5-23-16	0.20 ± 0.01	$20.2^{+4.2}_{-3.3}$ $(3.8^{+0.8}_{-0.6})$	88.5	$1.3^{+0.5}$	0.39 ± 0.01	1.48	-	-	169 [i]
NGC 4507	0.16 ± 0.01	$27.6^{+4.6}_{-5.2}$ $(6.9^{+1.1}_{-1.3})$	97.7	$1.2^{+0.3}$	0.48 ± 0.01	7.2	127 [b]	143 [c]	unresolved [j]
				UNDETERMINED					
IZwicky1				NGC 1365 (u)			IRAS05189-2524		H0557-385
IRAS09149-6206				Mrk 1239 (u)			NGC 3281		NGC 4151
3C273 (u)				NGC 4593			ESO 323-77 (u)		NGC 5128
IRAS13349+2438 (u)				IC4329A			NGC 5995		NGC 7469

Table 3.1: *Parameters of the best-fit models. Source: name. F_{pt}: Flux of the point source. minor axis θ_m: Full Width at Half Maximum of the minor axis. PA: Position angle of the major axis of the Gaussian. Ratio (ϵ): Ratio between the major and minor axis. To avoid degeneracies, we only take $\epsilon \geq 1$. Axis ratios with $\epsilon < 1$ produce the same elongation as $1/\epsilon$ but with PA rotated by $90°$. F_{gs}: Flux of the elongated Gaussian component. $\chi^2_{reduced}$: Reduced chi-square value. PA Polar axis: Position angle of the polar axis inferred from optical polarimetry. For Type 2 objects, we add $90°$ to the true position angle given by optical polarization (see text). PA NLR: Position angle of the symmetry axis of the ionization cone. PA Radio jet: Position angle of the radio emission from the jet. Objects with marginally resolved or unresolved $12\mu m$ emission are denoted with (u).* **References:** *a)Hönig et al. [2012]; b) Marin [2014]; c) Fischer et al. [2013]; d) Kinney et al. [2000], e) Mundell et al. [2000]; f) Elmouttie et al. [1998]; g) Orienti & Prieto [2010], h) Xanthopoulos et al. [2010]; i) Mundell et al. [2009]; j) Bransford et al. [1998]*
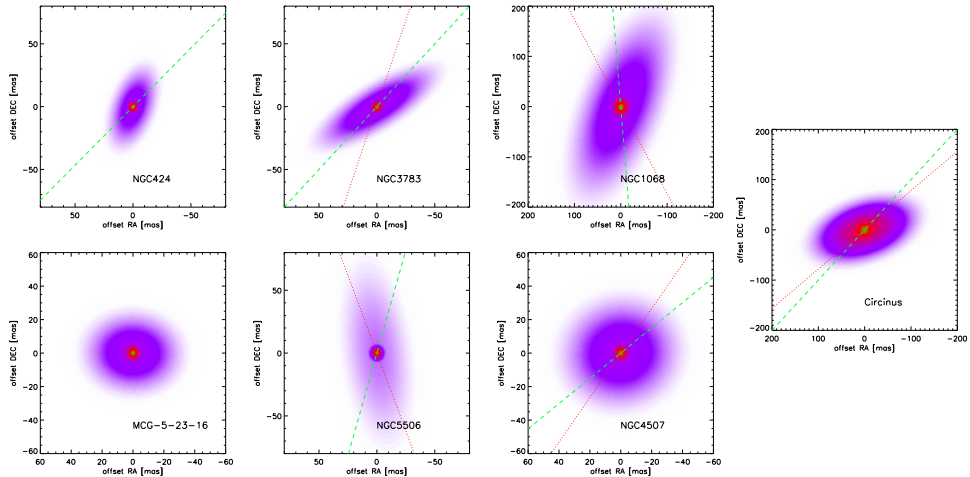
Figure 3.5: *Best-fit models for elongated objects. For every object, we show the 12 μm image obtained from our best-fit model using a square root scale. We add as a reference for the polar axis of the system, when available, the PA obtained from optical polarimetry (green dashed line) and from the symmetry axis of the ionization cone (red dotted line).*

Elongated MIR emission on the parsec-scale was found previously in four of the sources in this sample: NGC424 [Hönig et al., 2012], NGC3783 [Hönig et al., 2013], NGC1068 [López-Gonzaga et al., 2014], and the Circinus galaxy [Tristram et al., 2014]. These are among the brightest and very well-studied sources ($\gtrsim 30$ (u, v) points) where elongation and position angle can be constrained well. Our results (Table 3.1) are in excellent agreement with those previously published, confirming the reliability of the detected elongations. For NGC 1068 and Circinus, higher spatial resolution data show a distinct disk-like structure, which contributes $\sim 20\%$ to the total flux. This disk has a different PA than the large-scale structure that we model here. We ignore the small-scale structure for our large-scale fits since we would not be able to resolve such a structure in any of the other sources because of the lower spatial resolutions achieved here. The FWHM sizes and PAs derived from our large-scale analysis only, are however, very similar to those derived with the more complex disk + large-scale model.

Our reliability analysis has shown that we should also be able to detect elongated emission in MCG-5-23-16, NGC 4507, and NGC 5506. In NGC 5506, our fits indicate that the emission is indeed elongated. The confidence limit of the fit show that the axis ratio is inconsistent with 1 (circular) at 3σ level (Fig 3.2). The best-fit elongated model has an axis ratio of 2.5 with a well-defined lower limit, but with its major axis less well determined. The position angle of the major axis of the elongation is $8.3°\pm9$.

For MCG-5-23-16 and NGC 4507, on the other hand, the 12 μm emission at

subparsec scales is consistent with a near circular shape, see Fig. 3.3. The best-fit axis ratios are $1.3^{+0.5}$ and $1.2^{+0.3}$ for the two sources, respectively. For the remaining 16 objects, the (u, v) coverage and typical uncertainties do not allow us to recover the shape of the input brightness distribution.

3.4.1.   Polar or equatorial emission?

Determining the axis ratio and position angle of the MIR emission provides valuable information about the geometrical shape of the dusty emission, but we need to locate the position angle of the dust emission with respect to a known axis of the system to learn more about its nature. In principle, [OIII] line emission produced along the ionization cone can be used to determine the direction of the polar axis. Fischer et al. [2013] were able to identify the direction of the ionization cones by using biconical outflow models to describe the kinematic information of the NLR, given by long-slit spectra from the Space Telescope Imaging Spectrograph and [OIII] imaging. We can in principle assume that the symmetry axis of such a cone is a reasonable estimate of the polar axis of the system. The values reported for our sources by Fischer et al. [2013] are shown in Table 3.1. Since the axis of the ionization cone might be considered as model dependent[1], we additionally obtain an estimate of the system axis from optical polarimetry. As discussed by Marin [2014], the degree of polarization observed in Type 1 sources is relatively small, but any position angle detected for the optical polarization should be roughly parallel to the polar axis of the system. For Type 2 sources, the degree of polarization should be higher and have a position angle of the polarized light that is roughly perpendicular to the polar axis [e.g., Kishimoto, 1999]. This explanation could be a simplified version of reality since there might also be a transition region between type 1 and type 2 objects, where the position angle follows a different behavior. Keeping this possible ambiguity in mind, we nevertheless use also the polarization measurements to infer a system axis and list them in column 8 of Table 3.1 and plot them in Fig. 3.5 as green dashed lines. We find a reasonable agreement between the system axis determined by the NLR modeling and polarimetry with the largest discrepancy of $39°$ between the two inferred angles in the case of NGC 5506. For our purpose of determining whether the MIR dust emission is rather polar or equatorial elongated, this is sufficient accuracy.

In principle, we could also obtain information about the polar system axis from observing the direction of an existing jet. Synchrotron emission from the jet has been observed intensively at radio bands. We have collected information about the position angle of the jet from the literature and compare them with the values obtained for

---

[1]In the case of NGC 3783, the model reported by Fischer et al. [2013] differs in inclination from the model provided by Müller-Sánchez et al. [2011], although the position angles are rather similar (-20° and -177°, respectively).

the polar axis from optical polarimetry and from the NLR (see Table 3.1). For the objects NGC 4507, NGC 3783, and NGC 424, the emission is unresolved and therefore we cannot obtain any relevant information about the PA. In the case of Circinus, NGC 1068, and NGC 5506, the position angle of the jet agrees very well with the values obtained from optical polarimetry and a bit less well with the values from the NLR.

We observe that in all five objects, where we report an elongation, the position angle of the major axis of the MIR emission is always closer to the inferred polar axis of the system than perpendicular to it; see Fig 3.6. If we assume a marginally elongation for the object NGC 4507 to be true, then the mid-infrared PA for this object is also close to the polar system axis. Additionally, we observe that if the estimates of the polar axis system are indeed representative of the true polar axis system, then there is a lack of axial symmetry of the MIR emission around the polar axis (see bottom plot of Fig 3.6). In all the objects the emission is always leaned slightly toward one side of the polar axis. In the Circinus galaxy, for example, the difference is 20-30 degrees and in this source the positions angles of both the MIR emission and the ionization cone are very reliably determined.

Additionally, the multiple infrared shapes (Elongated: 1 Type I, 3 Type 2s, and 1 Type 1i and nearly circular: 1 Type 2 and 1 Type 1i) almost regardless of the Seyfert Type may be a surprising result if one has a picture in mind of a donut-like torus [e.g., Fig. 1 of Antonucci, 1993].

It has been long realized, however, that such a simple structure cannot represent the actual distribution of dust. Instead, the dust must be in a clumpy configuration [e.g., Schartmann et al., 2008] whose image, as simulated using radiative transfer, is complex and its reduction to an "elongated Gaussian model" is not at all obvious. If we also take hydrodynamical effects into account, even a more or less azimuthal dust configuration can produce images that are polar elongated (e.g., Fig. 8 of Schartmann et al. 2009 and Fig. 5 of Schartmann et al. 2014). In fact, models that produce an infrared emission with a X-shaped morphologies [e.g., Schartmann et al., 2005] also show polar extension to the zeroth order. Slight asymmetries in the density distribution produced by filaments or clouds could then explain the lack of asymmetry around the polar axis system. Additional information, such as kinematics, would be needed to distinguish such a scenario from, for example, a disk wind scenario, which would also produce polar-elongated emission [e.g., Wada, 2012; Gallagher et al., 2013; Schartmann et al., 2014].

While with infrared images alone we cannot provide a complete panorama about the structure of the torus, our result of the polar extended emission should serve as a constraint for dusty models that attempt to provide a description of the dusty environment in AGNs. Current SED fitting studies do not take this into account as

the SED does not provide any geometrical information. Further investigation needs to be carried out to see if derived torus properties, such as covering factors, torus sizes, and cloud numbers from torus models that reproduce the polar-like extended emission, are consistent with the current models used by the community.

3.4.2. Future improvements

In our reliability analysis, we studied how the (u, v) coverage and the SNR influence our ability to measure an intrinsic elongation. From this study, we learned that filling the (u, v) coverage is most relevant to determine an elongation. Without improving the accuracy of the measurements but just by obtaining more equally distributed (u, v) points at different position angles, we would be able to confirm or rule out elongations in at least six objects (LEDA17155, NGC 4151, NGC 4593, IC4239A, NGC 5995, and NGC 7469). These objects have relatively low-to-intermediate point source fractions (< 0.6), but their current (u, v) coverage typically has only measurements at resolutions where the emission is resolved, along two distinct position angles. For the objects IZwicky1, H0557-385, and NGC 3281, owing to their relatively high point source fractions ~ 0.8, an improvement of both the (u, v) coverage and SNR would be needed to learn more about the MIR geometry of these objects. It is worth noting that for the objects NGC 4151, NGC 4593, and NGC 3281 there is evidence for a 100 pc scale elongated structure with an orientation that is also close to the polar axis system [Asmus et al., 2014]. For these three objects, new infrared interferometric observations would be required to filled the missing (u, v) points and be able to investigate the nature of the elongated emission.

The remaining objects NGC 1365, Mrk 1239, 3C273, ESO 323-77, NGC 5128 (Cen A), and other objects with point source fractions ≈ 1 require longer baselines to resolve their compact MIR emission. Results from our reliability analysis should be used to plan future observations with the second generation instrument MATISSE [Lopez et al., 2014] to improve our view of the MIR emission in AGNs.

3.5. Conclusions

We have analyzed the mid-infrared interferometric data of 23 sources observed with the instrument MIDI at the VLTI and investigated in how many objects we should be able to find elongations given the observed (u, v) coverages along with the achieved SNR and the minimum visibilities. We found that we should be able to find elongated emission in seven out of 23 objects and indeed in five of these seven elongated emission is found (four objects are already published, NGC5506 is a new detection). However, we also find two sources (NGC4507 and MCG-5-23-16) that are compatible with nonelongated, i.e., circular emission. In the sources where deviations
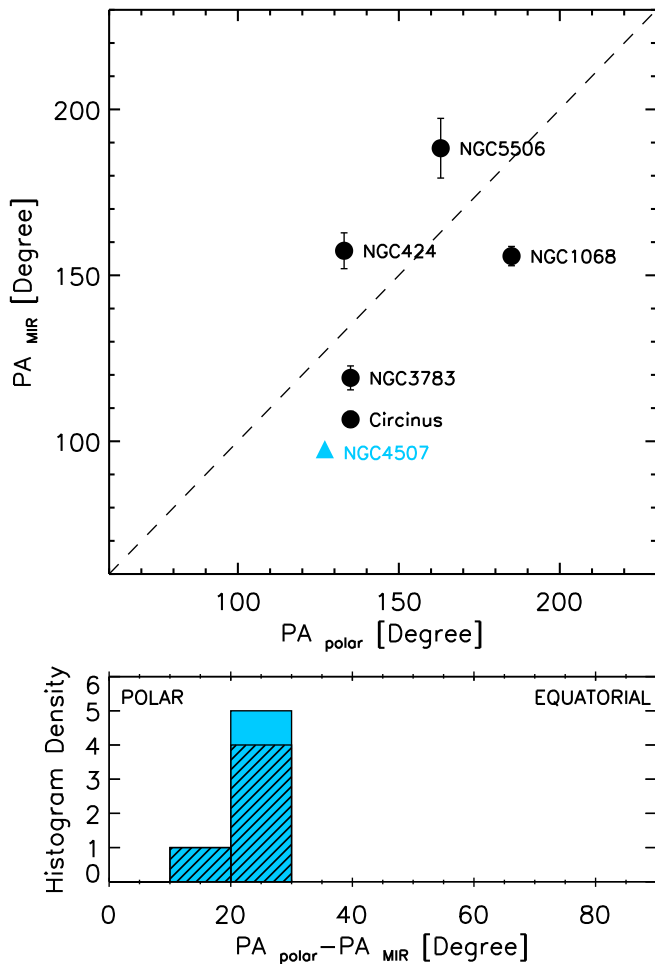
Figure 3.6: *Top) Comparison between the position angle of the mid-infrared emission from the parsec-scale structure (PA_{MIR}) and the inferred position angle of the system polar axis (PA_{polar}) for the elongated objects. For completeness we also include the marginally elongated object NGC 4507 (blue triangle), no error bars are determined for this object. The dashed line represents a one-to-one relation for the position angles. Bottom) Histogram of the difference between the inferred system polar axis and the mid-infrared position angle obtained using interferometry. The histogram including the marginally elongated object NGC 4507 is shown in blue bars, while elongated objects are indicated with black bars. Only objects with elongations obtained from interferometric data have been used here.*

from a circular emission geometry are detected, the elongation is always much closer to the polar than the equatorial direction of the system. The trend of polar elongated emission at parsec scales is compatible with what is observed at 100 pc scales (e.g, NGC 4593, NGC 3281, Asmus et al. 2014; NGC 4151, Radomski et al. 2003; Circinus, Packham et al. 2005; Reunanen et al. 2010; NGC 1068, Galliano et al. 2005b).

This needs to be followed up with higher SNR and more homogeneous (u, v) coverage before further conclusions can be drawn. Most importantly, a complete sample of AGN tori [e.g., selected by hard X-rays such as Davies et al., 2015] should be observed with the upcoming four-beam MIR interferometer MATISSE at the VLTI [Lopez et al., 2014] to assess the shape and sizes of AGN tori in a representative sample.

CHAPTER 4

Mid-infrared interferometry of Seyfert galaxies: Challenging the Standard Model

N. López-Gonzaga, W. Jaffe
Astronomy and Astrophysics, in press (2015)

Abstract

We aim to find torus models that explain the observed high-resolution mid-infrared measurements of active galactic nuclei (AGN). Our goal is to determine the general properties of the circumnuclear dusty environments. We used the mid-infrared interferometric data of a sample of AGNs provided by the instrument MIDI/VLTI and followed a statistical approach to compare the observed distribution of the interferometric measurements with the distributions computed from clumpy torus models. We mainly tested whether the diversity of Seyfert galaxies can be described using the Standard Model idea, where differences are solely due to a line-of-sight effect. In addition to the-line-of sight effects, we performed different realizations of the same model to include possible variations that are caused by the stochastic nature of the dusty models. We find that our entire sample of AGNs, which contains both Seyfert types, cannot be explained merely by an inclination effect and by including random variations of the clouds. Instead, we find that each subset of Seyfert type can be explained by different models, where the filling factor at the inner radius seems to be the largest difference. For the type I objects we find that about two thirds of our objects could also be described using a dusty torus similar to the type II objects. For the remaining third, it was not possible to find a good description using models with high filling factors, while we found good fits with models with low filling factors. Within our model assumptions, we did not find one single set of model parameters that could simultaneously explain the mid-infrared data of all 21 AGN with line-of-sight effects and random variations alone. We conclude that at least two distinct cloud configurations are required to model the differences in Seyfert galaxies, with volume-filling factors differing by a factor of about $5-10$. A continuous transition between the two types cannot be excluded.

4.1.   Introduction.

Active galactic nuclei (AGN) have been extensively studied to understand the possible link between the growth of supermassive black holes (SMBHs) and the evolution of galaxies. The main characteristic of AGNs is their extremely high luminosity. In particular, AGNs are known to emit a large part of their energy in the form of infrared radiation [Neugebauer et al., 1979; Barvainis, 1987; Sanders et al., 1989; Elvis et al., 1994, and references therein]. This infrared excess can be explained by a conversion process where a fraction of the nuclear UV and optical radiation is absorbed by circumnuclear dust at a few parsecs from the central black hole and re-emitted in the infrared regime. This circumnuclear dust, commonly referred to as the dusty torus, not only redistributes the emitted energy of AGNs, but sometimes also blocks our view of the nuclear engine.

According to the Standard Model for AGNs, all Seyfert galaxies are assumed to have a similar nuclear environment, consisting of an accreting supermassive black hole surrounded by ionized clouds moving at high velocities (the broad emission line region: BLR). This nuclear engine is then surrounded by circumnuclear dust. In its most simple form, the Standard Model predicts a bimodal distribution of the Seyfert types [Antonucci, 1993; Urry & Padovani, 1995]: type 1, for which the nuclear engine can be directly viewed, and type 2, for which the view to the central engine is blocked by dust. This idea is supported by the broad emission lines in the spectra of many type 2 sources observed in polarized light [see, e.g., Antonucci & Miller, 1985].

Studying the properties and morphology of the circumnuclear dust is crucial to improve our understanding of the accretion process of AGNs. It is unclear as yet how the gas flows into the accretion disk, but tracing the coexisting dust can help to reveal the morphology of the gas stream. This process of transport to the inner regions is poorly understood, but is relevant for understanding the triggering and evolution of AGNs as well as the energy feedback to the host galaxy.

High-resolution infrared images of the circumnuclear dust are expected to allow tracing the structure of these objects and determining their general properties. But infrared observations of the AGN environment that isolate and resolve the torus emission have been difficult to obtain. Early observations with the *Spitzer* telescope provided studies of AGN samples [see, e.g., Buchanan et al., 2006]. Their sensitivity allowed statistical studies on a large number of detected objects, but their limited spatial resolution did not accurately isolate the AGN emission from sources of contamination, such as star-heated dust and dust in the ionization cones [Bock et al., 2000; Tomono et al., 2001; Packham et al., 2005]. In contrast, large ground-based mid-infrared (MIR) instruments, with their higher resolution power, can distinguish between AGN emission and star formation regions [e.g., Galliano et al., 2005a; Alonso-Herrero et al., 2006, 2011; Horst et al., 2006, 2008, 2009; Haas et al., 2007;

Siebenmorgen et al., 2008; Levenson et al., 2009; Ramos Almeida et al., 2009, 2011; Hönig et al., 2010; Reunanen et al., 2010; van der Wolk et al., 2010; Mason et al., 2012; Asmus et al., 2011, 2014]. However, in the majority of the cases the AGN emission remained unresolved, suggesting either a small size for the nuclear dusty environment or potential nonthermal contributions such as the synchrotron emission observed in the radio galaxy Centaurus A.

Mid-infrared interferometers have enabled a breakthrough by spatially resolving the compact emission of AGNs. Several studies of individual galaxies have revealed the complexity of the nuclear dusty environment. A few examples of these findings are that the nuclear dust environment of the Circinus galaxy shows a two-component structure consisting of a disk-like emission surrounded by an extended emission with its major axis close to the polar axis [Tristram et al., 2014]; the hot and compact dusty disk in the nucleus of NGC 1068 shows extended and diffuse emission along one side of its ionization cone [Raban et al., 2009; López-Gonzaga et al., 2014]; NGC 424 and NGC 3783 show extended thermal infrared emission with major axes close to the polar axes [Hönig et al., 2012, 2013]. In addition, Tristram & Schartmann [2011] analyzed a sample of sources observed with interferometers and suggested a luminosity-size relation for the warm dust. This relation was later challenged by Kishimoto et al. [2011a] using a sample of type 1 sources. It seemed similarly unlikely in the light of results obtained using a larger sample of AGNs, the MIDI AGN Large Programme [Burtscher et al., 2013], which revealed a diversity of complex dust morphologies on subparsec scales. The diversity of sizes suggests that a luminosity-size relation might not be unique for the warm dust as it is in the case of the hot dust observed in the near-infrared [Barvainis, 1987; Suganuma et al., 2006; Kishimoto et al., 2009b, 2011b; Weigelt et al., 2012], where the inner radius of the torus scales with the square root of the AGN luminosity.

From the theoretical point of view, much progress has been made in recent years in reproducing the infrared emission of the dusty torus with radiative transfer models. Early radiative transfer models of AGN dust tori were carried out by Pier & Krolik [1992, 1993] and Granato & Danese [1994] using smooth dust distributions. However, such a smooth dust distribution probably does not survive in the nuclear environment of an AGN [Krolik & Begelman, 1988], but might instead be present in the form of clouds. Pioneer work from Nenkova et al. [2002] presented a stochastic torus model with dust distributed in clumps that is capable of attenuate the strength of the silicate feature. More recently, many torus models, using different radiative transfer codes, techniques, and dust compositions, have been developed to obtain more efficient and accurate solutions of the radiative transfer equations and to improve the assumptions [Nenkova et al., 2002; Dullemond & van Bemmel, 2005; Hönig et al., 2006; Nenkova et al., 2008a,b; Schartmann et al., 2008; Hönig & Kishimoto, 2010; Stalevski et al.,

2012; Heymann & Siebenmorgen, 2012; Siebenmorgen et al., 2015].

However, all the models face one common problem: the dynamical stability of the structure and the process to maintain the required scale height are still debated. Self-consistent models describing both the physical processes that distribute the toroidal gas and dust and the redistribution of the nuclear emission are still under development, but with promising results [see, e.g., Dorodnitsyn et al., 2011, 2015; Wada, 2012; Schartmann et al., 2014, and references therein].

Many authors have fit the spectral energy distributions (SEDs) of Seyfert galaxies with clumpy torus models [see, e.g., Nikutta et al., 2009; Mor et al., 2009; Ramos Almeida et al., 2009; Alonso-Herrero et al., 2011; Ichikawa et al., 2015], but the conclusions from these works must be examined critically. Since the SEDs contain no direct spatial information on the torus, the results are highly degenerate; results from a comparison between clumpy and continuous models indicate that models using different assumptions and parameters can produce similar SEDs [Feltre et al., 2012]. We may expect the degeneracies to be partially broken if we include high-resolution interferometric observations that resolve the structures and provide direct measures of the sizes and shapes of the emission regions.

The aim of this work is to find a family of torus models that fits the interferometric data on a set of AGNs obtained over the past decade. We focus more on the general properties of the acceptable models than on particular characteristics provided by individual fits. The paper is organized as follows: The main goals and motivation are explained in Sect. 4.2. We provide information about the Seyfert sample and describe the data treatment in Sect. 4.3. A brief explanation about the torus models used for this work and the method followed for our comparison is given in Sects. 4.4 and 4.5, respectively. The results are presented in Sect. 4.6. We discuss the general properties in Sect. 4.7. A summary of the results is given in Sect. 4.8.

4.2.   Probabilistic approach

Ideally, multiwavelength high-quality infrared images of several AGNs would determine the most important dust model parameters, such as cloud sizes, disk inner radii, wavelength-dependent extensions, opening angles, and dust chemistry. However, high-fidelity infrared imaging is not yet possible since interferometric techniques are time consuming and lack detailed phase data, and their resolution is not high enough to resolve individual clouds. This situation is expected to improve in a few years when the next generation of interferometers come online, for instance, GRAVITY [Eisenhauer et al., 2011], which will observe in K band, and MATISSE [Lopez et al., 2008], which will observe in L, M, and N band.

Our ability to determine the underlying parameters of clumpy models is also

limited by their stochastic nature; even when all parameters are specified, random variations in the cloud distributions may present markedly different images to the observer.

These limitations necessitate a probabilistic approach to modeling. Our main goal is to investigate whether we can statistically reproduce the data of our whole interferometric sample by using models that have specified global properties, but where the appearance of each source is affected by unknown factors (V_i with $i = 1, 2, 3$): 1) the randomness in the positions of the clouds, 2) the inclination, and 3) the position angle of the source axis on the sky. The stochastic arrangement of the clouds can produce different families of spectra or images of the model even when they are built with the same global parameters [Hönig et al., 2006; Schartmann et al., 2008]. The torus inclination angle is of primary importance because it determines the chance of viewing directly (low inclinations) or indirectly (high inclinations) heated clouds. The position angle is an important unknown when only limited interferometric baselines are available.

We aim to find global properties that the AGNs might have in common and to test with these the existence of any overall unifying model of AGNs. Our procedure is to search for a model that explains all the observations on a statistical basis. If this fails (as it does), we consider the possibility that the model parameters may vary from object to object, or for certain classes of objects. This is the case if our models can fit each galaxy or class individually, but not all of them for one parameter set.

4.3. Observational data

4.3.1. Infrared data

Our sample consists of 21 Seyfert galaxies observed with the MID-infrared Interferometric instrument [MIDI[1] Leinert et al., 2003] at the European Southern Observatory's (ESO's) Very Large Telescope. This flux-limited sample was published by [Burtscher et al., 2013], who required sources with a flux higher than 300 mJy at $\lambda \sim 12\,\mu$m in high-resolution single-aperture observations. For more specific information about the reduction process and observation strategy we refer to Burtscher et al. [2013]. The original set also includes data for the quasar 3C273 and the radio source Cen A, but we omit these two sources as their nuclear MIR emission may not originate in the same way as in Seyfert galaxies. For example, the nuclear MIR flux of Cen A is dominated by unresolved emission from a synchrotron source, while the contribution of the thermal emission of the dust only represents about 40 % of the

---

[1]The instrument MIDI is a two-telescope Michelson-type beam combiner with an operational spectral range in the atmospheric N band ($\lambda \sim 8 - -13\mu$m)

Source	D	z	Type	L_{IR}	L_{xray}
	[Mpc]				
I Zw 1	222	0.0589	Sy 1	44.9	43.7
NGC 424	44.7	0.0110	Sy 2	43.6	43.8
NGC 1068	14.4	0.0038	Sy 2	44.0	43.6
NGC 1365	18.1	0.0055	Sy 1	42.5	42.1
IRAS 05189-2524	167	0.0426	Sy 2	44.6	43.7
H 0557-385	135	0.0339	Sy 1	44.4	43.8
IRAS 09149-6206	222	0.0579	Sy 1	44.9	44.0
MCG-05-23-16	38.8	0.0085	Sy 2	43.5	43.3
Mrk 1239	84.5	0.0200	Sy 1	44.0	43.3
NGC 3281	47.6	0.0107	Sy 2	43.4	43.2
NGC 3783	43.8	0.0097	Sy 1	43.7	43.2
NGC 4151	16.9	0.0033	Sy 1	43.0	42.5
NGC 4507	51.7	0.0118	Sy 2	43.7	43.2
NGC 4593	41.2	0.0090	Sy 1	43.1	42.9
ESO 323-77	64.2	0.0150	Sy 1	43.7	42.8
IRAS 13349+2438	393	0.1076	Sy 1	45.5	43.9
IC 4329 A	68.3	0.0161	Sy 1	44.2	43.9
Circinus	4.2	0.0014	Sy 2	42.7	42.3
NGC 5506	28.7	0.0062	Sy 2	43.4	43.1
NGC 5995	102	0.0252	Sy 2	44.1	43.5
NGC 7469	60.9	0.0163	Sy 1	43.9	43.2

Table 4.1: *Source properties.* **Notes.** *D: angular-size distance derived from redshift, except for Circinus and NGC 1068; z: Redshift (from NED); Type: AGN classification from SIMBAD; L_{IR}: The $12\,\mu$m infrared luminosity is given as $\log(L_{MIR}/erg \cdot s)$ and the values were obtained from Burtscher et al. [2013], uncertainties are typically lower than 5%; L_{xray}: The absorption-corrected $2-10$ keV X-ray AGN luminosity given as $\log(L_x/erg \cdot s)$. The values were collected from Asmus et al. [2015]*
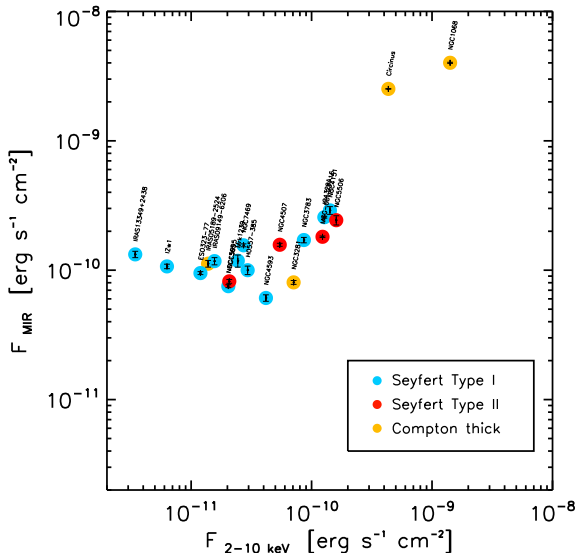
Figure 4.1: *Absorption-corrected $2-10\,keV$ X-ray fluxes versus nuclear $12\,\mu m$ fluxes.*

total emission at $12\,\mu m$ [Meisenheimer et al., 2007]. We exclude the quasar 3C273 because the MIR environment of high-luminosity objects might differ from that of low-luminosity objects (Seyfert galaxies) sources [see, e.g., Stern, 2015].

Each source was observed with pairs of 8 m unit telescopes (UTs), and Circinus and NGC 1068 were additionally observed with pairs of 1.8 m auxiliary telescopes (ATs), in at least three different baseline configurations. The main observable of the instrument MIDI is the correlated flux, which can be seen as the measured fraction of the total flux that is coherent for a particular (u, v) point[2].

To capture the shape of each interferometric spectrum and to reduce the computational time, we used three different wavelengths in our fits. We took the average values at $(8.5 \pm 0.2)\,\mu m$, $(10 \pm 0.2)\,\mu m$ and $(12 \pm 0.2)\,\mu m$ rest frame, whereby we include information about the slope and the amplitude of the silicate feature.

4.4. Clumpy torus models

Since we cannot create images from our MIR interferometric data, we need to make use of models to interpret our observations. The dusty cloud models used for this work are based on the approach followed before by Schartmann et al. [2008]. In this section we briefly explain some of the general aspects of the models, but for more details we refer to Appendix A. These models are built with dense spherical dusty clouds distributed randomly throughout a defined volume. The temperature distri-

---

[2]A (u, v) point can be defined as the coordinates, for a given projected baseline and a position angle, in the Fourier-transform space of the angular distribution of the source on the sky.

butions within these cloud arrangements are quite complex and need to be solved numerically by using radiative transfer codes. The overall dust temperature distribution of the dust and the scaling properties of the torus are essentially determined by the strength of the heating source and the fraction of the UV emission that the dust clouds intercept.

The models used for this work are characterized by the following parameters (P_i): 1) The total average optical depth at $9.7\,\mu$m along the equator, 2) the opening angle defining the dust-free cone, 3) the local fractional volume occupied by the dusty clouds at $1\,$pc given by the filling factor, 4) the radial extension of the dusty torus defining the outer radius, and 5) the density profile index α that defines the radial density profile of the clouds. The modifications to the original model presented by Schartmann et al. [2008] are as follows.

- Isotropic emission of the central source. We omit the $|\cos(\theta)|$ law profile emission of the original model as there is no evidence for a strong anisotropy in the MIR – X-ray relation [see, e.g., Ichikawa et al., 2012].

- We define our filling factor at the inner $1\,$pc region instead of taking the whole volume space. N-band fluxes are sensitive to dust with a temperature near $300\,$K, and for the nuclear luminosities L_{UV} used in our modeling, most of the dust at this temperature is found at a radius of $\sim 1\,$pc.

We used the radiative transfer code RADMC-3D[3] to compute the temperature and the surface brightness distributions of the dusty torus. First the temperature of the system was computed by sending out photon packages using a Monte Carlo approach. Anisotropic scattering was treated using the Henyey-Greenstein approximate formula (Henyey & Greenstein [1941]. After computing the temperature of the dust grains, we used the included ray tracer to obtain the surface brightness maps at the required wavelengths. We computed high-resolution model images for different lines-of-sight (a given ϕ and θ angle in the coordinate system of the model) at three different wavelengths, $8.5\,\mu$m, $10.0\,\mu$m, and $12.0\,\mu$m. To determine the corresponding Seyfert type of the images along a line-of-sight (LOS), we took the respective value of the optical depth in the visual τ_V and classified them as type 1 if $\tau_V < 1$ and type 2 if $\tau_V > 1$, that is, type 1 if there is a direct view of the nucleus and type 2 if the nucleus is obscured. Finally, to obtain the correlated fluxes, we applied a discrete fast Fourier transform to each image.

For every parameter set, we computed at least ten different realizations of the model to estimate the variations that are due to the position of the clouds. For every realization we extracted the images along ten different LOS corresponding to type 1 objects and also ten LOS where the nucleus is obscured (type 2 objects).

---

[3]http://www.ita.uni-heidelberg.de/ dullemond/software/radmc-3d/

INPUT PARAMETERS	
Parameter	Values
Bolometric luminosity accretion disk (L_{disk})	$1.2 \times 10^{11}\, L_{\odot}$
Inner radius of the torus (R_{in})	$0.4\,\mathrm{pc}$
Constant of clump size distribution (a_0)	$0.2\,\mathrm{pc}$
Radial profile density exponent (α)	$-2, -1.5, -1, -0.5, 0$
Radial extension	25, 50, 75, 100 R_{in}
Half opening angle (θ_{open})	$30\,^{\circ},\ 45\,^{\circ},\ 60\,^{\circ}$
Total average $\tau_{9.7}$ along the equator ($\langle \tau_{9.7} \rangle_{\phi}$)	1, 2, 4, 8, 16
Filling factor at inner rim	$0.4, 1.4, 5.3, 20, 40\,\%$
Number of realizations	10
Lines of sight per realization	
type 1:	10
type 2:	10
Distribution of inclination angles	Uniform in a sphere

Table 4.2: *Input parameters. Values of the parameters used as input to build the clumpy torus models. For a full description of how the torus models are constructed see Appendix A.*

4.4.1. Luminosity rescaling

The luminosity of the central engine obviously is a key parameter in determining the appearance of the source. To match our model images with the observational data for any particular source, we required an accurate estimate of the nuclear UV luminosity to scale the size of the observed objects with the size of the model images. Since it is usually not possible to directly measure the UV emission of the accretion disk, we examine here one of the commonly used tracers for the UV luminosity: the absorption-corrected 2–10 keV X-ray luminosity.

Several studies [see, e.g., Lutz et al., 2004; Horst et al., 2008; Gandhi et al., 2009; Levenson et al., 2009; Ichikawa et al., 2012; Asmus et al., 2015] have reported a tight correlation between absorption-corrected $2-10$ keV X-ray and MIR luminosities for Seyfert galaxies, which has been interpreted as a direct connection between the luminosity of the accretion disk and the luminosity of the torus. In Fig. 4.1 we show the MIR fluxes from Burtscher et al. [2013] and the absorption-corrected 2–10 keV X-ray fluxes from Asmus et al. [2015]. We used fluxes instead of luminosities to avoid false correlations induced by the spread in redshifts. The correlation is unclear and the X-ray flux is spread over about one decade for sources with essentially the same MIR flux.

Because the relation of the X-ray and UV as well as the significant scatter in the MIR-Xray is unclear, we decided to avoid using L_X as a proxy for L_{UV}. Instead we

assumed a nominal nuclear isotropic heating luminosity L_m as part of the modeling process and adjusted its value for each model so that the single-aperture $12\,\mu$m predicted by the model matches the observed value. The observed single-aperture fluxes are in general accurately measured. This L_m was used to rescale the model sizes and fluxes, as described below.

The nominal luminosity L_m is the energy emitted from the nucleus that then iluminates the clouds and generates the $12\,\mu$m emission. This luminosity is effectively the same as L_{UV}, although it might differ slightly if the dust at the inner radius is not modeled accurately. Although we cannot strictly check the accuracy of this nominal luminosity because we lack near-infrared (NIR) measurements, we expect the deviations to be only mild as the hot emission is treated consistently in our models. Thus any possible deviation from the true L_{UV} might occur if a completely different prescription for the ensemble of clouds were used in the enviremissiononment close to the sublimation radius.

The images described in the previous section were computed for a nominal model nuclear UV luminosity L_m ($1.2\times10^{11}\,L_\odot$) at a nominal model distance D_m. These must be compared to the MIR observations of sources at an actual distance D_s computed from the redshift and actual nuclear luminosity L_s, which is assumed to be unknown.

For this comparison, we mathematically moved the model to D_s and then adjusted L_m until the total infrared continuum emission toward the observer at $\lambda = 12\,\mu$m equaled the observed $12\,\mu$m single-aperture flux. This adjustment was calculated for each model realization, including the cloud distribution and the inclination angle θ, because these factors affect the fraction of the nuclear luminosity converted from UV into infrared and then projected toward the observer, that is, the observed UV-IR efficiency, η_{UV-IR}.

Adjusting the nuclear luminosity would a priori involve recalculating the radiation transferred through the cloud distribution for each realization. Fortunately, scaling relations in the radiation transfer obviate this computationally expensive step. Assuming that the grain size distribution remains constant, we expect the inner dust sublimation radius r_{in} to scale as $L_s^{1/2}$ because the temperature of dust grains exposed directly to nuclear UV should only depend on the flux, L_s/r_{in}^2. So we may intuitively expect a source with a given L_s to resemble one with L_m, but all emitted luminosities are scaled by L_s/L_m and all dimensions scaled by $(L_s/L_m)^{1/2}$. We directly tested this scaling relation with the RADMC-3D models over variations of a factor of 10 in L_m and found it to apply with high accuracy, even for emission from regions not directly heated by the nucleus. In other words, the spatial distribution of the infrared radiation at all wavelengths considered here scales directly with r_{in}.

For a full description of our procedure we refer to Appendix 4.9.2.

4.5. Description of the method

4.5.1. Stochastic modeling

In Section 4.2 we explained that with our data, studies of individual sources may not determine uniquely the parameters P_i underlying the stochastic models. A statistical method dealing with the entire dataset may give better insight into these parameters.

We sought a statistical method that is robust and relatively familiar, so that bad fits can be easily diagnosed. The second criterion suggests a variant of the χ^2-test method. Several difficulties immediately arose. First, the interferometric dataset is very inhomogeneous; measurements were made of galaxies of different luminosities, at different distances, position angles, and baselines. Second, some of the measures are highly correlated with respect to the stochastic variables V_i. Finally, the actual selection criteria of the sample are also quite inhomogeneous.

We circumvented the first two problems by using the information provided by the models to find transformations that convert the measurements $CF_{uv,n}$ to new un-correlated, zero-mean, unit-variance variables $cf_{uv,n}$. For each model we produced a large number of realizations of the stochastic variables V_i: source orientation, inclination, and cloud positions. For each galaxy the individual measurements $CF_{uv,n}$, that is, the correlated fluxes at each (u,v) position, were simulated for each of the model realizations after adjusting for the source luminosity described in Sect. 4.4.1. These simulations produced a probability distribution of simulated measurements $CF_{uv,n}^{model}$ for the galaxy that were then convolved with the distribution of noise estimates from the actual measurements $CF_{uv,n}$. If the model is correct, the true data values should then lie within the most likely parts of the distributions (65 % of the distribution for a Gaussian-like distribution). A very poor model can be rejected at this phase if the individual measurements $CF_{uv,n}$ lie outside the predicted ranges. But models can also be rejected if the total set of data, per galaxy or group of galaxies, is unlikely, and for this we have to consider the expected correlations between the measurements.

The distributions are characterized by their means and (co)-variances. For a given model we now constructed for each galaxy a new set of variables $cf_{uv,n}$ from the original measurements $CF_{uv,n}$ by first subtracting the mean expectation values predicted from the models and then computing linear combinations of the measurements that diagonalize the cross-correlation matrix to unit values. These new variables therefore have zero mean, unit variance, and zero cross-correlation if the model is correct. In this way we can test for any single galaxy, or any set of galaxies, the acceptability of the model by summing the squares of the transformed variables $cf_{uv,n}$ and comparing the total with that expected from the sum of the same number of normal Gaussian variables, that is, a χ^2-distribution with the given number of degrees of freedom. We

note that models can be rejected if the squared sum is either too large (measurements do not look like the model) or too small (model predicts variances that are larger than the measured values).

4.5.2. Selection effects

We now considered the inhomogeneous selection criteria. The large program sample was chosen from well-known relatively nearby southern Seyfert galaxies, whose nuclear single-aperture N-band fluxes were above 300 mJy. When we test whether a specific model could account for a single (u, v) measurement or for all the measurements on one galaxy, this selection process is not critical to the interpretation. In this case, we only gauge whether there is some mildly probable cloud configuration that matches that data. When instead we test whether the data from all sample galaxies, or a subgroup of these galaxies, can be explained by a single model, we have to consider the selection effects. The data distributions calculated above were found by assuming that all the stochastic variables are uniformly distributed. The selection process may skew these distributions. For example, if a cloud distribution tends to extinguish N-band emission in the equatorial plane, galaxies with dust structures viewed edge-on will be less likely to meet the 300 mJy limit. This would contradict the assumption of a random distribution of inclination angles.

To account for this, we considered the efficiency η_{UV-IR} of converting nuclear UV emission into MIR emission directed toward the observer. Each model cloud realization yields a different calculable value for this efficiency. Low-efficiency realizations require a higher and therefore less probable nuclear luminosity for the MIR flux to exceed the survey limit S_{IR}. Therefore we modeled the effect of the MIR flux selection on the model distributions by reweighting each stochastic realization proportional to the probability that the nuclear luminosity L_{nuc} exceeds $4\pi D_s^2 S_{IR}/\eta_{UV-IR}$. Hard X-ray surveys of Seyfert nuclei [Georgantopoulos & Akylas, 2010] indicate that the integral luminosity function, that is, the probability that the luminosity exceeds a specified value L_{nuc}, scales approximately as $L_{nuc}^{-\gamma}$ with $\gamma \simeq 1$. Thus we can model the effect of the flux selection on the observed distributions by reweighting each realization in proportion to $\eta_{UV-IR}^{+\gamma} \simeq \eta_{UV-IR}^{+1}$.

Similarly, we introduced a reweighting to model the selection of the galaxies as Seyfert AGNs in the first place. The principle Seyfert classifications depend on the escape of hard UV photons from the hot accretion disk to the narrow line region (NLR), which is well outside our modeling region, where they induce high-excitation ionization. We modeled this effect by calculating for each realization the UV-escape efficiency η_{esc} for UV photons to escape the cloud regions and by reweighting the realization proportional to η_{esc}^{γ}.

Best-fit values		
type 1 parameters	Acceptable area	Best fit
Radial profile density exponent	≤ -1.5	-1.5
Radial extension [r_s]	Unconstrained	50
Opening angle [Deg]	Unconstrained	45
Total average $\tau_{9.7}$	≥ 8	16
Filling factor at inner rim [%]	[0.4 - 1.4]	0.4
type 2 parameters	Acceptable area	Best fit
Radial profile density exponent	≤ -1	-2
Radial extension [r_s]	Unconstrained	100
Opening angle [Deg]	[45 - 60]	60
Total average $\tau_{9.7}$	≥ 8	16
Filling factor at inner rim [%]	≥ 5	20

Table 4.3: *Best-fit parameters. Range of the acceptable values and best-fit solution for each AGN subsample. These acceptable solutions were obtained independently for each subsample.*

The effects of these reweighting schemes on the best-fitting model parameters are described in more detail below.

4.6.   Results

It is very time consuming to compute the temperature profile and the respective images of every realization, therefore we explored the parameter space using a discrete set of values. The values taken for each parameter are shown in the top section of Table 4.2, together with other input parameters. To account for a bias that is due to the detection limit of the sample, our results were obtained using a reweight, as stated in Sect. 4.5.2, with a value of $\gamma = 1$.

4.6.1.   The full sample

We first analyzed our entire sample containing Seyfert type 1 and 2s together. We searched for the best combination of parameters P_i that statistically describe our sample. In all our mapping space we did not find any set of parameters P_i that produces models consistent with our entire sample of AGNs. Within our range of parameters, this result suggests that our sample is not consistent with the idea that their observed differences should only be attributed to a LOS effect; this is consistent with the result of Burtscher et al. [2013].
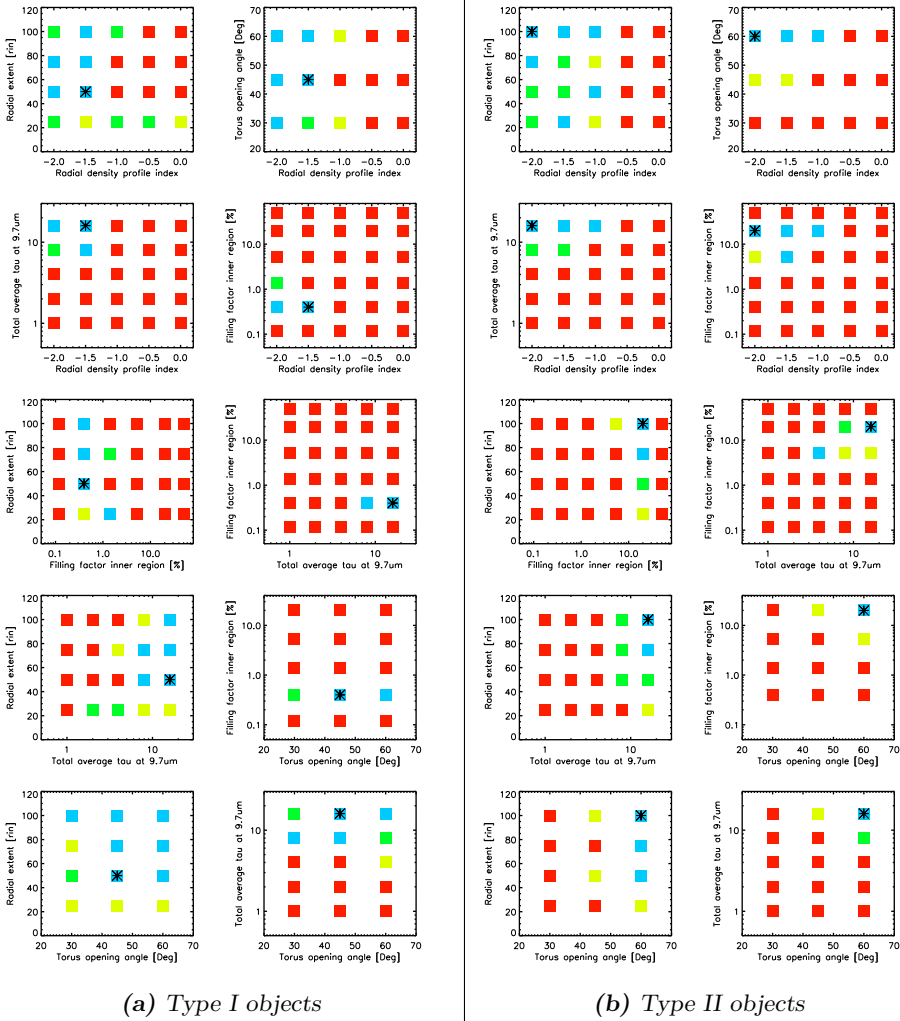
(a) *Type I objects*

(b) *Type II objects*

Figure 4.2: *Discrete maps showing the level of acceptance around the best-fit solution for type 1 sources (first and second column) and type 2 sources (second and third column). In every panel, three of the five parameters of the best solution are kept fixed, while the two parameters shown in the labels of each plot are explored. The best-fit solution is shown with an asterisk. The color of the squares indicates the acceptance value of the parameters based on a χ^2-test. The blue squares indicate the probability of the χ^2-value using the equivalent percentages of a Gaussian distribution at the 1σ level (68 %), green the probability at 95 % confidence, yellow up to 99.5 % and red above 99.5 %.*

Our entire sample cannot be reproduced statistically by a single set of model parameters P_i, while each individual galaxy can be fit by its own set of parameters $P_{i,n}$. This suggests two possible cases. First, AGNs cannot be explained with one fixed set of parameters P_i, but instead we need a broad range of parameters P_i. Alternatively, there are major subgroups within the sample, each of which can be fit with its own set of parameters P_i. When searching for the best set of parameters, we observed that occasionally the type 2 objects and some of the type 1 objects were consistent with each other, but a significant fraction of type 1s seemed to be poorly fit. This motivated us to investigate both types independently to search for their best-fit models. A reasonable set of parameters that describes our subsets would allow us to explain why we failed to fit the two groups together.

4.6.2.   type 1

We continued our search in the parameter space using the type 1 set, that is, sources where our view to the nucleus is not blocked by the dust. In the models, this means taking LOS that penetrate the dust-free volume inside of the opening angle and LOS at high inclinations that by chance do not encounter clouds along its path. For this set of objects we did find combinations of model parameters that produced a distribution of correlated fluxes that is compatible in a probabilistic sense with the observational data. The range of model parameters that shows a best fit with the data are listed in Table 4.3. Additionally, we plot in Fig. 4.2a discrete maps showing the behavior of the level of acceptance when we let two parameters change freely around the best solution. We display these confidence levels as color-coded plots for different pairs of input parameters. This allows the viewer to decide quickly whether the best-fitting parameters are correlated, or in other words, whether particular combinations of parameters are better constrained than the individual parameters themselves.

We observe from Fig. 4.2a that for the type 1 subset the best-constrained parameters are the volume-filling factor, the radial density profile index, and the optical depth. Only model spatial filling factors at $1\,\mathrm{pc}$ radius between $0.4\,\%$ and $1.4\,\%$ fit the type 1 observations at better than the 3σ level. As we explain in more detail in the discussion section, the low percentages for the filling factor are necessary to produce a diverse family of spectra and sources with multiple sizes without using different parameters P_i for every object. Because the clouds are somewhat larger than in other available models [Hönig et al., 2006; Nenkova et al., 2008a], realizations in our models with low filling factors and steep radial density profiles have a very limited number of total individual clouds, between $5-10$ clouds on average.

We also obtain a good estimate for the total radial optical depth at $9.7\,\mu$m. This parameter must be on the order of or higher than $\tau_{9.7\,\mu m} = 8$, corresponding to a value in the optical of $\tau_{0.5\,\mu m} \gtrsim 75$. Lower values for the optical depth all yield fits

equivalent to 4σ or worse for a normal distribution. A combination of high optical depths and inclination effects allows a reduction of the silicate feature. In this case the shadowing effect explained by Schartmann et al. [2008] might not be too strong because there are only a few clouds.

With the low filling factor of the type 1s, we anticipate that the index of the radial density profile for the clouds may be poorly constrained. The low number of clouds may not allow an accurate determination of the density profile. Still, we observe in Fig. 4.2a that only steep radial distributions, with an index lower than -1, agree with our observations, meaning that clouds are more likely to be found at close or intermediate distances (a few tenths of the sublimation radius). Sets of models with a low filling factor at the inner radius but flatter distributions instead produce an excess of cold emission because a many clouds could exist at large distances, while the number of clouds at the smallest distances can be kept low.

The maximum radial extension is poorly constrained in our models because we lack long-wavelength infrared data. In all the plots that show the radial extension the fits are good for all the possible values. Because the best-fit parameters have a steep radial cloud distribution, not many clouds exist at large radius. If present, clouds at large distances will be dominated by cold emission ($< 100\,\mathrm{K}$) and should be detected at (sub-) milimiter wavelengths. The opening angle for a limited number of clouds does not make much sense as the distribution of clouds along the azimuthal direction produces similar results for different opening angles. We observe in the two lower plots of Fig. 4.2a that the opening angle is essentially good in the range used for our search, $30-60$ degrees. This behavior is expected when the number of clouds is low.

4.6.3.   Type IIs

After finding the best-fit parameters for the type 1 objects, we searched for the best-fit parameters for the type 2 objects to see if the deviate from the type 1 sample. Since our models are wedge-like structures, the type 2 LOS are confined within a region outside the opening angle.

We found several sets of parameters P_i that reproduce the type 2 observations. The range of best-fit parameters found for this subset are shown in Table 4.3, and variations of the level of acceptance when changing two parameters around the best-fit solution can be seen in Fig. 4.2b.

For type 2 Seyfert galaxies, the radial slope of cloud distribution is steep, similar to the type 1 sources. The acceptable index for the density profile lies between -2 and -1. Again, because of this steep slope and the lack of long-wavelength infrared data, the maximum radial extension of the torus is poorly defined.

The main difference between Figs. 4.2a and 4.2b is the range of acceptable values
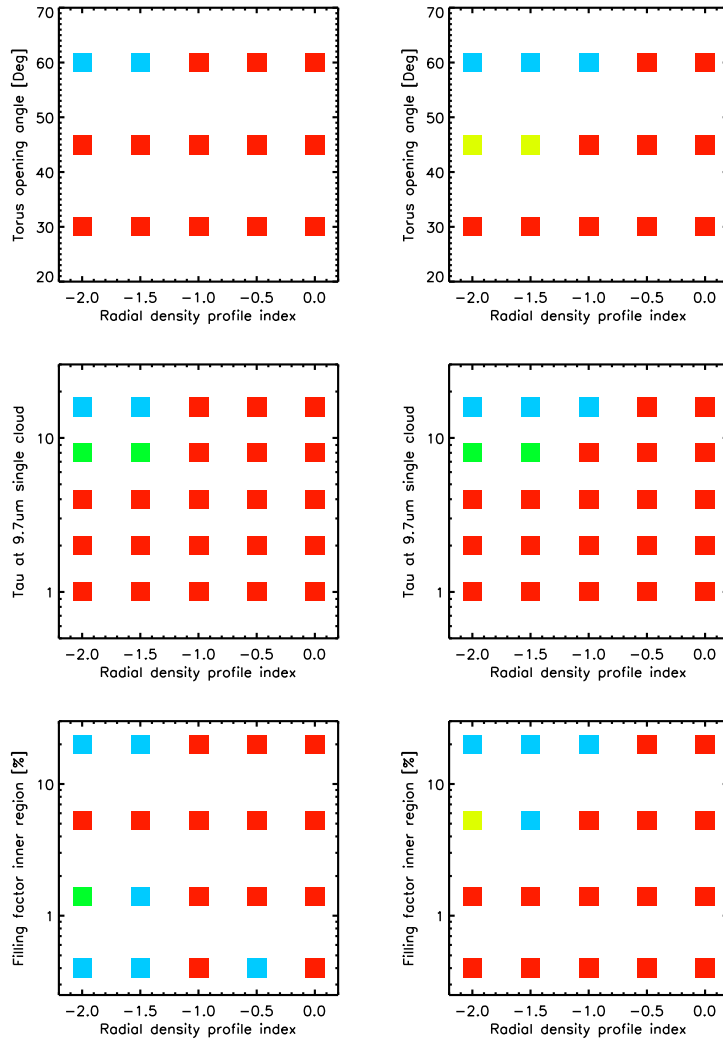
Figure 4.3: *Comparison of the discrete maps for models of type 2s using (left) no luminosity reweighting and (right) a more realistic reweighting with $\gamma = 1$.*

for the filling factor. For the type 2 sources, the number of clouds at the inner regions is significantly larger for than the type 1 sources. The acceptable filling factors for the type 2 sources are larger than ∼5 %. This means that the cloud-filled volume near 1 pc is a factor of 5 or higher than that in the type 1s. This suggests an important intrinsic difference between types 1 and 2.

The average optical depth throughout the whole disk at $9.7\,\mu$m is similar for the type 2 models to that of the type 1 models. Any optical depth value above 8 gives reasonable fits. Increasing the value of τ beyond ~ 8 makes no difference; by this time, all the N-band photons have been absorbed and converted to even longer wavelengths.

A higher filling factor at the inner radius for type 2s and similar density profile index with respect to type 1s means that type 2 objects have a larger total number of clouds. With similar values of the optical depth for both types, but type 2s having a higher total number of clouds means that for type 2s it is more likely to observe dusty clouds along the LOS. The fewer clouds in the type 1 model result in a lower covering fraction and larger (u, v) variations for an individual type 1 with respect to a typical type 2.

The best value for the opening angle lies near $60\,^\circ$. Models with opening angles of $45\,^\circ$ are in the 2σ or 3σ region, those with opening angles of $30\,^\circ$ are quite unlikely since they are in the 4σ area. For small opening angles the images along obscured LOS of these models will look more or less round, while models with large opening angles essentially produce flat disks. A study of the elongations in the Large Program sources suggests an intrinsic ratio of 1:2 [López-Gonzaga et al., 2016]. Therefore, a roundish model might not be a good representation of the dusty structure of sources such as NGC 1068 and Circinus, especially because these two objects both have a disk-like component and a near-polar extended component. These two moderate-luminosity galaxies are so close that the long baseline interferometric measurements represent a physical resolution that is not obtainable for any of the other survey galaxies. To include them in our analysis on a comparable basis to the others, we only included interferometric measurements for these two at projected baselines < 40 m, which only includes information about the extended component and an unresolved component (the disk resolved with higher projected baselines). Therefore, it is likely that due to the arbitrary location of the axis system in our analysis, the best-fit model is influenced by the elongations of the sources, and as a result, fixing the opening angle produces the required elongations (1:2) but with an incorrect system axis.

4.6.4. Line of sight selection

Since the same input bolometric was used for all the models, using a weight means that bright images are more likely to be observed, since the ratio between the infrared
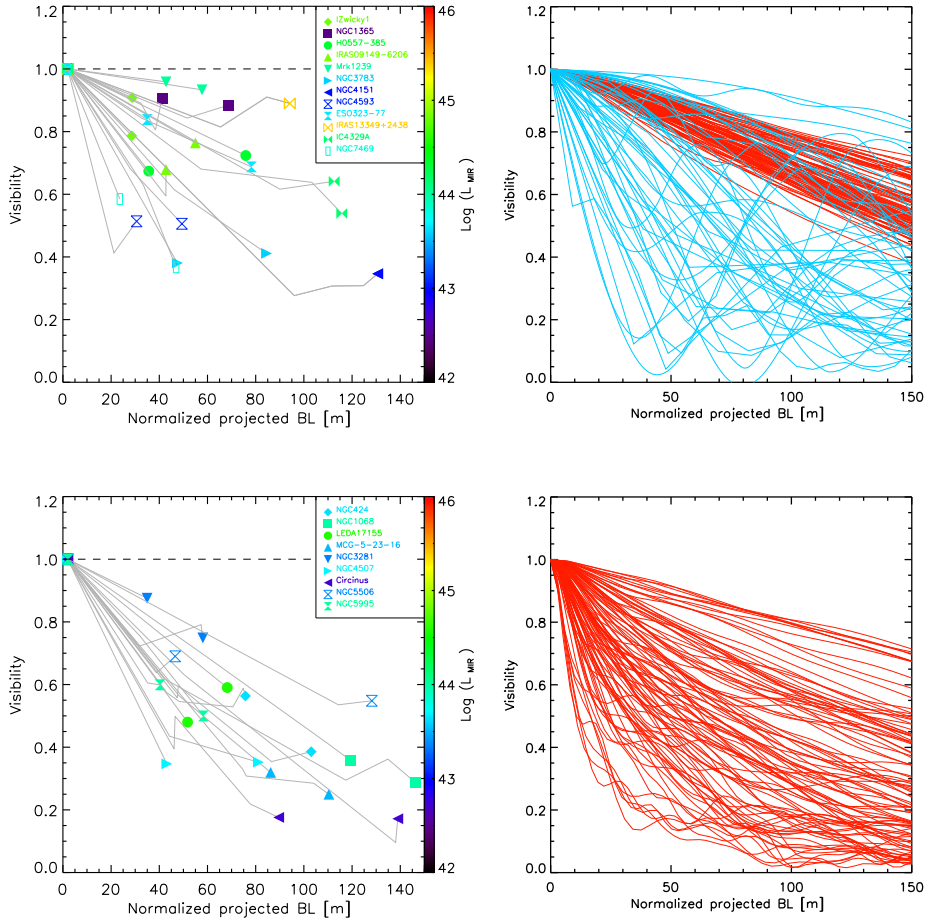
Figure 4.4: *(Left) 12 µm interferometric visibilities of type 1 (top) and type 2 sources (bottom) plotted against the normalized projected baseline. For every object we include visibilities for two different position angles connected by independent lines. The normalized baseline is scaled from the observed baseline for each source to normalize its single-aperture 12 µm flux; cf. Sect. 4.4.1. Each symbol indicates the longest baseline data point available at the given position angle for an individual object. The color of the symbols indicates the value of the infrared luminosity of the source as shown on the scale at the right, data are from by Table 4.1. (Top right) Model normalized 12 µm interferometric radial plots for various lines of sight where the nucleus is exposed, corresponding to type 1 objects, computed from type A models (blue) and from type B models (red). (Bottom right) Model radial plots for various obscured LOS, corresponding to type 2 objects, computed for the best type B models.*

and UV is lower than faint images in the infrared. For high optical depths this causs the images with high self-absorption to be rarer. We applied the same weighting exponent to both type 1 and 2 throughout all our work. Only type 2 sources show a clear difference when using the reweight. The $12\,\mu$m emission of the type 1 sources is less likely to be affected by self-absorption of the dust. The dispersion of the $12\,\mu$m fluxes for a particular model for type 1 objects is not very broad, and therefore the reweighting does not play an important role.

For type 2 objects this reweighting is quite relevant. For high-inclination values, the $12\,\mu$m fluxes can be more affected by the self-absorption of the dust clouds. In Fig. 4.3 we show a comparison for different parameters using a rescaling with $\gamma = 1$ and without weights. The greatest difference is that if we do not use the reweighting, models with low filling factors become likely for type 2 sources. The reason for this is that in these types of models the hot surfaces of the individual clouds produce similar bright spots in the large scales as the surfaces produced by models with high filling factors, where the emission in the large-scale structure is produced by escaping emission through holes. The rescaling we performed to match the fluxes and distances of the real sources modifies the sizes and aligns them with those given by our interferometric measurements. Although the geometry generally looks similar, the problem of not using a reweighting is that for type 2 models with low filling factors the ratio between the bolometric luminosity and the infrared luminosity becomes extremely high, some of ratios are even quite unrealistic, as seen from the luminosity function of Seyfert galaxies.

4.7. Discussion

4.7.1. What does the interferometer see?

In this section we examine the images of the best models to acquire intuitive insight into their structures, and to understand which features in the models cause noticeable differences in the actual observations.

Our work shows that apparent differences in the MIR morphology arise not only from inclination effects, but that statistical variations in the cloud distribution can be relevant as well. When the size of the clouds is large enough and the fraction of the volume occupied by the clouds is relatively low, the appearance of the MIR emission will vary depending on our specific LOS and realization of the models [Hönig et al., 2006; Schartmann et al., 2008]. In the probabilistic models presented by Nenkova et al. [2008a,b], these variations do not appear explicitly because their models are built using average quantities, therefore differences that are due to statistical variations of the clouds are ignored.
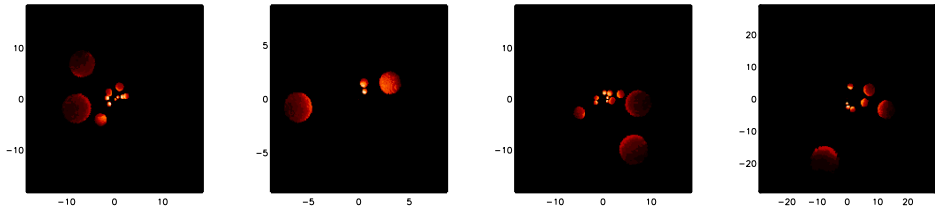
(a) *12 μm images created from one of the best type 1 models (model A). We only show lines-of-sight where the nucleus is exposed. Each plot shows a different realization of the cloud positions. Labels denote the distance to the center in pc.*
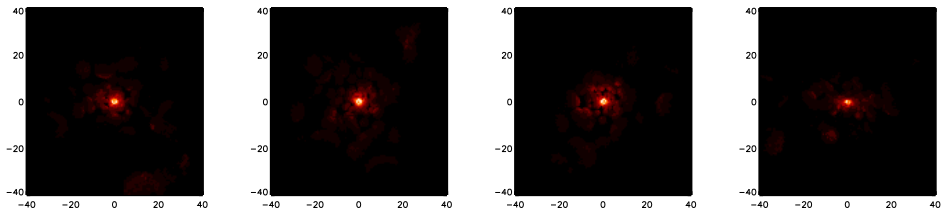
(b) *Same as Fig. 4.5a, but the images are created from the unobscured lines-of-sight from model B, i.e., type 1s with the same filling factor as type 2 objects.*
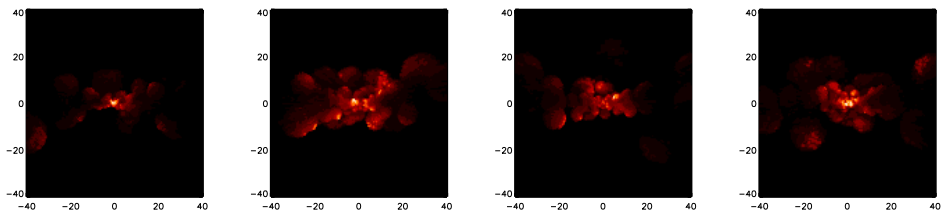
(c) *Same as Fig. 4.5a, but the images are created from the obscured lines-of-sight from model B, i.e., the best type 2 model.*

In Fig. 4.4 (top) we plot the observed interferometric $12\,\mu\text{m}$ visibilities of our objects using measurements along two distinct position angles if available. The baselines are rescaled to compensate for their luminosities and distances, as described in Sect. 4.4.1. To the right of the same figure we plot the model visibilities for different realizations of type A and type B models that would have been classified as a Seyfert 1 galaxy because the nucleus is directly visible. In Fig. 4.5a we show model images of four realizations of type A models and in Fig. 4.5b images of type B models with unobscured nuclei. The lower plots in Fig. 4.4 and the images in Fig. 4.5c represent observations and models of Seyfert 2 galaxies and type B models with obscured nuclei. Except for two objects in the left top plot of Fig. 4.4, when normalized in the infrared, low-luminosity objects seem to be better resolved than high-luminosity objects.

The plot of Fig. 4.4 (top left) shows large variation in visibilities of the Seyfert 1 galaxies, which is reproduced by the low filling factor type A models. The type B unobscured models show much less variation and relatively high visibilities because more clouds in the model are located closer to the inner regions of the torus, making is seem compact and smooth. Figure 4.5a shows that the appearance of the low filling factor models is determined by the positions of a few hot, bright, unobscured clouds around the nucleus. The random variations of the positions of these clouds in the realizations creates the large variations in apparent visibility. This creates the apparently uniform high visibilities in these models. It is clear from the plots that the curves from the high filling factor type B model cannot reproduce the overall distribution of observed visibilities for our full sample of type 1 objects: the variation in visibilities would be too low. Objects such as NGC 3783, IC4239A, and NGC 4593 have large dispersions in their visibilities that cannot be explained with the type B model. Although the aim of this work is not to find the physical explanations for the dusty structure, we note that the three mentioned objects have lower luminositis than the less resolved objects (e.g., IRAS 13349+2438). We cannot, of course, exclude that some of the type 1 galaxies represent unobscured type B geometries, a situation similar to the original Standard Model.

For Seyfert 2 galaxies, images from obscured LOS of type B models are shown in Fig. 4.5c. With the nuclear regions blocked by dust, the emission is dominated by the accidental positions of relatively free LOS through holes in the cool dust to warmer areas at various radii. These accidents produce the variations in visibility seen in the bottom plots of Fig. 4.4. Once again, a few of the observed Seyfert 2 galaxies may arise from type A low-density geometries where the LOS is blocked by a stray cloud.

4.7.2.   Spectral energy distribution.

We only analyzed the N-band data, where the new interferometric measurements include more spatial information than the single-aperture spectral energy distributions (SEDs) alone. Ideally, we should describe the SED and interferometric data simultaneously. We did not attempt this because of the difficulties of consistently calibrating multiwavelength observations, the very different resolutions and fields of view of these observations, possible contamination from other physical sources, and lack of multiwavelength observations for most of our objects.

In spite of these problems, we can produce the SEDs with the radiative transfer code over broad wavelength ranges for our best-fit models with the purpose of displaying the overall predicted behavior of the spectra. The SEDs presented in this work can be further investigated by us or other groups to verify them outside the MIR window. In particular in the near-infrared, the promising technique presented by Burtscher et al. [2015] for isolating the NIR emission of the AGN is expected to provide good constraints for the hot emission.

We show examples of different realizations of the best type 1 model for unobscured inclinations (in Fig. 4.6a) and for obscured inclinations using the best type 2 model (Fig. 4.6c). We also include the SEDs of unobscured inclinations for the best type 2 model in Fig. 4.6b. The SEDs corresponding to different realizations of obscured type 2 objects show a diverse family of spectra with variations of the silicate feature in absorption. Similar to other torus models, the modeled spectra only show a moderate absorption feature in contrast to the deep silicate feature typically present in continuous models. From Fig. 4.6c we observe that it is also possible to obtain SEDs with relatively high emission at short wavelengths from hot dust coupled with small silicate absorption features. It is quite likely that such SEDs correspond to regions with holes in the cloud distribution through which the hot emission from the inner regions is seen, giving rise to a significant contribution of flux in the near-infrared. The small silicate feature in this case could be explained as an average between the absorption feature produced from the back faces of the clouds and the silicate feature in emission that is viewed through the holes of the torus. This could explain the absence of a silicate feature in absorption and the relatively blue spectra of NGC 424 described by Hönig et al. [2012].

The main differences between the SEDs of the true type 1 models and those of the unobscured type 2 models are in the strength of the silicate feature and the slope of the spectrum in the $2-20\,\mu$m wavelength range. The silicate features in true type 1 models vary from weak absorption to moderate emission; the spectral slopes vary from moderately hot (large near-IR contribution) to moderately cool; the warmth of the continuum slope is directly correlated with the strength of the emission feature. For the unobscured type 2 models the silicate feature is always

seen weakly in emission and the continuum spectrum (in units of λL_λ) weakly rising toward shorter wavelengths.

In Fig. 4.7b we zoom into the $8-12\,\mu$m single-aperture spectra for the observed objects, as well as the output spectra from their respective best-fit models. The multiple spectra are generated from different realizations and multiple inclinations of the best-fit model. In the top row we observe that the spectra of type 1 objects agree well with the predictions of the model. The diversity of slopes and the featureless spectra seem to be well described. As a comparison, we additionally include the interferometric spectra from the lowest baseline available. Many of our type 1 objects are slightly resolved with the shortest baseline resolution, so the differences in the shape of the spectra are small. If contamination by surrounding starburst regions is present in the single-aperture spectra, however, the shortest baseline spectrum should be less affected by this. The observed type 2 spectra are also well reproduced by the best-fit modeled spectra. Objects with deep silicate features can be explained with our model, although they are less common.

4.7.3.   Are Type Is different than Type IIs?

The strictest form of the AGN Standard Model explains all differences between the Seyfert types by LOS effects. This model assumes that the dusty tori of all Seyfert galaxies have very similar properties. Our attempts to model the MIR interferometric data indicate that this is not possible. To fit the observed sample we need (at least) two different models, distinguished primarily by different dust-filling factors in the volume radiating in the MIR. For this subsection only we denote for brevity the low filling factor models, consistent with the type 1 galaxies, as type A models and the high filling factor models as type B.

Considering all LOS, approximately $10-30\,\%$ of the type A models would be classified as Seyfert 2 galaxies by optical observers because the LOS happens to hit a cloud. Conversely, for the best-fitting type B model, approximately $40-50\,\%$ would be classified as Seyfert I because the LOS allow a direct view of the nucleus, either because it lies within the torus opening angle or by chance misses all clouds. We also note that although the type 1 and 2 source subsamples as a whole require different models, there are individual sources that can be described with either model. These considerations bring back the Standard Model in a weakened form. While most of the observed Seyfert 2 galaxies have model B structures, some of them have model A structures, but are classified as Seyfert 2 because of the viewing geometry, and vice versa for Seyfert I galaxies.

Our result of the intrinsic differences between type 1 and 2 sources in terms of the filling factor or covering fractions was previously suggested by the results of Ramos Almeida et al. [2011], who used fits on the SEDs of individual galaxies. Recent
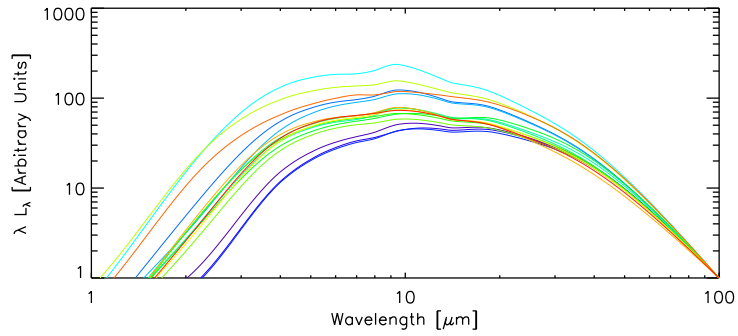
(a) *Using the best-fit model of type 1 objects. Only unobscured lines-of-sight are considered here. The contribution of the accretion disk is not included in the SED.*
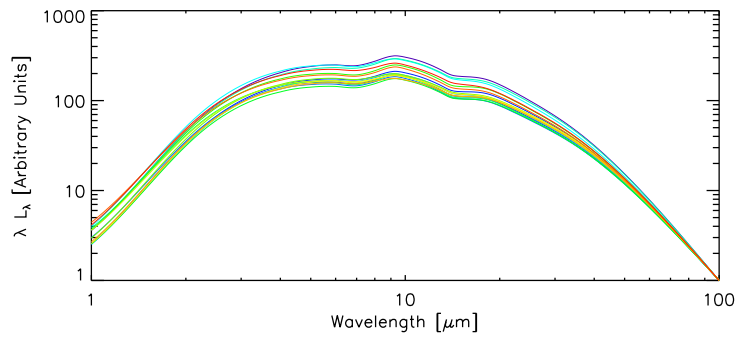
(b) *The same as Fig. 4.6a, but for unobscured lines-of-sight from the type 2 model.*
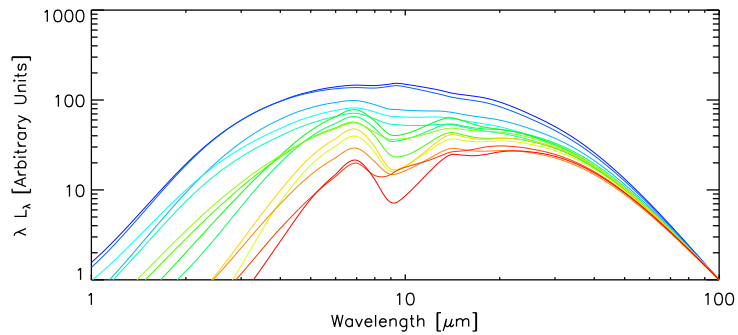
(c) *Same as Fig. 4.6b for obscured lines-of-sight from type 2 models.*

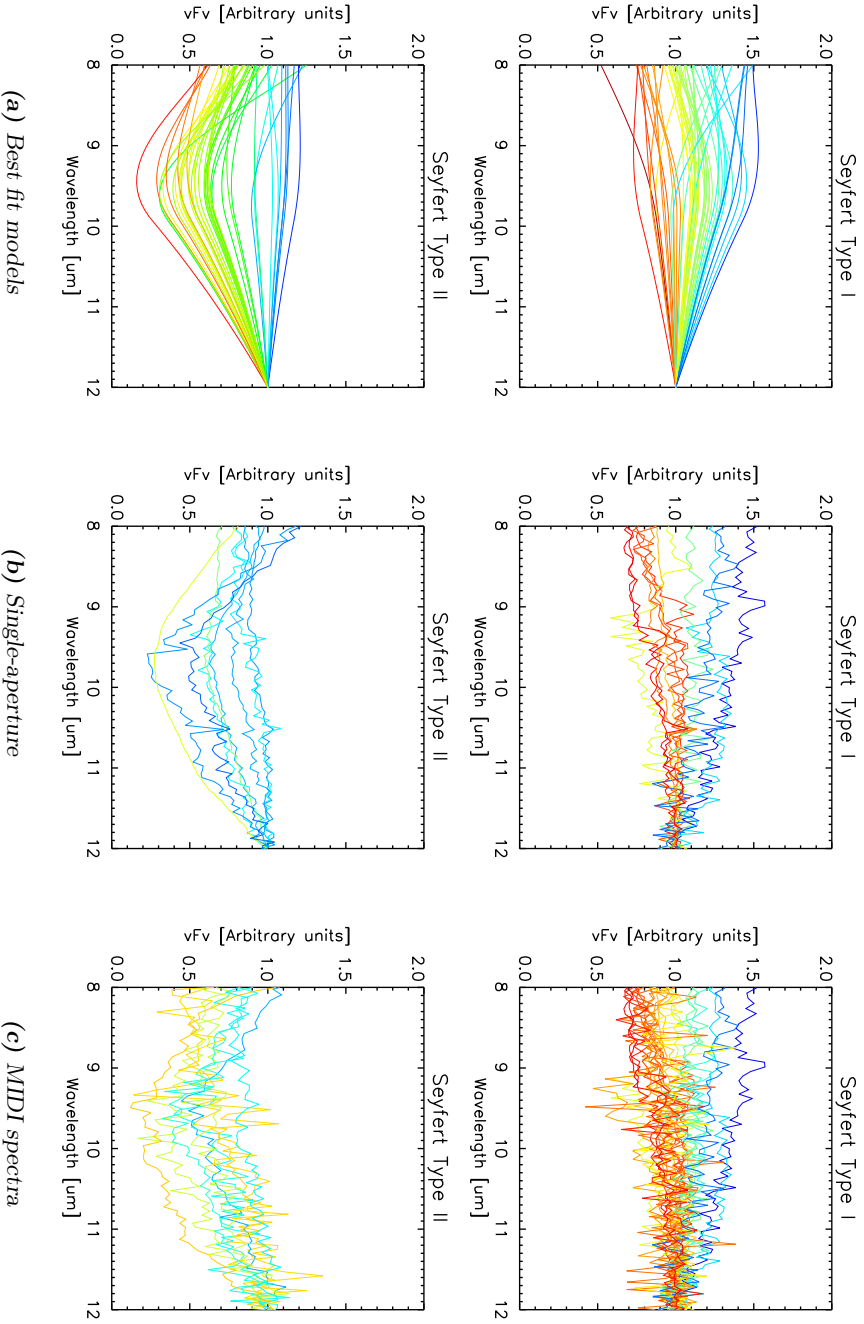**Figure 4.6:** *SEDs for multiple realizations of the best-fit model.*

Figure 4.7: *N-band spectra for type 1 objects (top row) and type 2 objects (bottom row). The spectra have been normalized to the 12 μm flux. Left column) Multiple spectra from the best-fit models. Center column) Observed single-aperture spectra for the objects of our sample. Right column) Observed interferometric spectra obtained with the lowest baseline available. The colors indicate the slope of the continuum, warm spectra are given in blue and cool spectra are given in red.*

(a) Best fit models

(b) Single-aperture

(c) MIDI spectra

findings by Mateos et al. [2016] obtained by modeling the SEDs of a X-ray selected complete sample of 227 AGN, indicate a lower covering fration for type 1s than for type 2s. With our method, we proceed from the usual SEDs studies by using high-resolution data provided by interferometers where the emission is indeed being resolved and by finding models that statistically reproduce the general features of a sample of sources instead of focusing on the details of individual objects. Our results are in agreement with the findings of Ramos Almeida et al. [2011] and Mateos et al. [2016] and all support the statement that the covering fraction of the torus should be lower for type 1s than for type 2s [Elitzur, 2012].

We do not go in detail into the question of the true percentages of high or low filling factor structures in the local Universe because this requires extremely careful consideration of how any observational sample is selected, but we discuss some of the consequences of accepting two different underlying structures. We assume that half of the Seyfert galaxies observed are type 2. If half of the type B structures are classified as type 1 sources (e.g., because they are observed within the opening angle), then the fraction of intrinsic type A structures must be small, otherwise the fraction of galaxies classified as type 1 would exceed 50 %. But this situation is essentially that of the Standard Model and contradicts our main result that the type B models fail to fit globally the interferometrically observed sample of type 1 objects.

If we reduce the fraction of type B structures that are classified as Seyfert Is to below 50 %, then the fraction of true type As among the Seyfert Is of course rises. If we require that >50 % of the Seyfert Is be in fact type A structures (to be consistent with our interferometric measures), the maximum fraction of type B structures that cross over in the observations is 30 – 40 %.

4.7.4. Mid-infrared emission efficiency

In this section we try to find a reasonable estimate of the intrinsic amount of UV flux, emitted by the accretion disk, by using the observed $12\,\mu$m nuclear flux and the efficiency ratio η_{UV-IR}, defined in this case as the ratio between the UV flux and the observed $12\,\mu$m flux. For a dusty medium distributed non-uniformly in a volume, the efficiency ratio is no longer constant, but is dependent on the LOS. The variations of the efficiency ratio η_{UV-IR} depend on the distribution of the medium and in particular become larger when the LOS is optically thick in the infrared, or in other words, when self-absorption of the dust becomes more relevant. The diversity of η_{UV-IR} values should be kept in consideration when computing the UV luminosity from the observed infrared luminosity in Seyfert galaxies.

To obtain a reasonable estimate of UV flux for our objects, we computed for every best-fit model the distribution of the efficiency factors along multiple line-of-sights and with different realizations. For the type 2 objects we computed the distribution

of the efficiency ratio for model B (best type 2 model) reported in Table 4.3, and then we used the infrared flux to obtained an estimate of the UV emission from the accretion disk. We show the computed UV flux in Fig. 4.8 together with the corrected $2-10$ keV X-ray fluxes.

For the type 1 models we used a slightly different approach. We previously showed that our entire sample of type 1 objects cannot be fit with the same model as the type 2s, but it might be possible that a fraction of our type 1s can be consistent with the unobscured LOS of the type 2 model. For objects where our model B fails in describing the interferometric measurements we seem to find a good fit using a low filling factor environment. For our type 1 objects we individually searched for the best-fit models using a low filling factor between $0.4-1.4\,\%$ and also a higher filling factor between $5.3-20\,\%$. In Fig. 4.8 we show for every type 1 object two estimates of the UV flux, one using a model with a low filling factor and the second using a high filling factor. For objects that cannot reasonably be described using a high filling factor model, we only show the estimates from the low filling factor model.

Corrected $2-10$ keV X-ray luminosities are assumed to be related to the UV bump of the accretion disk and are sometimes used to estimate the UV luminosity. From Fig. 4.8 we observe that a correlation might exist if we allow a mixture of objects with a low and a high filling factor. It is also clear that our objects with the low filling factor models do not seem to be outliers despite their general low efficiency ratio η_{UV-IR}.

4.7.5.   Stability of the clouds

Our best-fit low filling factor models are built with a limited number of clouds with high optical depths, typically with $\tau_{9.7} \geq 8$. Clouds with such optical depths should be quite massive, therefore the question arises whether these clouds are physically possible. In particular, we investigate if the thermal pressure is sufficient to keep the clouds from collapsing. To answer this question, we used the Jeans instability criterion. From the virial theorem and assuming a static, spherical, homogeneous cloud, we obtain that the critical mass for a cloud to collapse is given by $M_J \sim 6.64 \times 10^{22} T^{3/2} \rho^{-1/2}\,[g]$. If the mass of our cloud exceeds the value of M_J, the thermal pressure is not enough to keep our cloud from collapsing.

Since for our best type 1 model the clouds are located close to the inner rim, we tested the stability of one such clouds. The typical volume of a cloud close to the inner rim is $V_{cl} = 9.8 \times 10^{53}\,\mathrm{cm}^3$ and the dust mass of the cloud is $M_{dust} = 0.77\,\mathrm{M}_\odot$. To derive the total mass of the cloud we used a dust to gas ratio $\rho_{dust}/\rho_{gas} = 0.01$, which gives a total mass of $M_{tot} = 77\,\mathrm{M}_\odot$. From the radiative transfer computation we obtain an average temperature of the cloud of $T \sim 270\,\mathrm{K}$. The resulting Jeans mass for this configuration is $M_J \sim 361\,\mathrm{M}_\odot$, which is greater than the total mass of

our cloud $M_{tot} = 77 \, \mathrm{M}_\odot$. Although this calculation does not include other effects, such as rotation or shearing effects, we show that in a static situation the thermal pressure can prevent such clouds from collapsing. In fact, our calculation predicts that the cloud might expand since it is not confined by gravity. It might also be possible that the clouds are confined by external gas pressure.

4.8.   Conclusions

We presented results from a statistical method developed to interpret interferometric data with complex radiative transfer models. We applied our method to the interferometric data of AGNs published by Burtscher et al. [2013] and constructed our model images according to the dusty torus models from Schartmann et al. [2008]. We summarize our major findings below.

1. Mid-infrared interferometric data of a combined AGN sample, including both type 1 and type 2 sources, cannot be described by a single stochastic model (using Schartmann et al. [2008] models) under the assumptions of the Standard Model where observed differences are only attributed to inclination and line-of-sight effects.

2. Type 1 and type 2 sources can be well explained by such models if they are taken as two separate subsets with different model parameters for each subset. We found that the greatest difference between the models that describe each subset is in the volume fraction that the clouds occupy in the inner regions.

3. Seyfert type 1 galaxies are best explained by using torus models with low filling factors at the inner regions, between $0.4\,\%$ and $1.5\,\%$ of the volume of a spherical shell. The low filling factor implies a relatively small number of clouds. This small number produces large apparent fluctuations in interferometric measures of the type 1 sources, including a broad range of apparent geometrical sizes. This agrees with the large dispersion in sizes reported by Burtscher et al. [2013].

4. Seyfert type 2 galaxies are best explained with torus models with a filling factor of 5 or larger than those describing the Seyfert type 1s. The torus emission in the type 2 sources seems to be dominated by the warm infrared emission from a very compact region that escapes through the holes created by the clumpy nature of the torus. These random holes might be causing the asymmetrical emission in the large-scale structure.

5. Although two models are necessary and sufficient to explain our observations of the two Seyfert subsets, this represents an oversimplification. By accidents
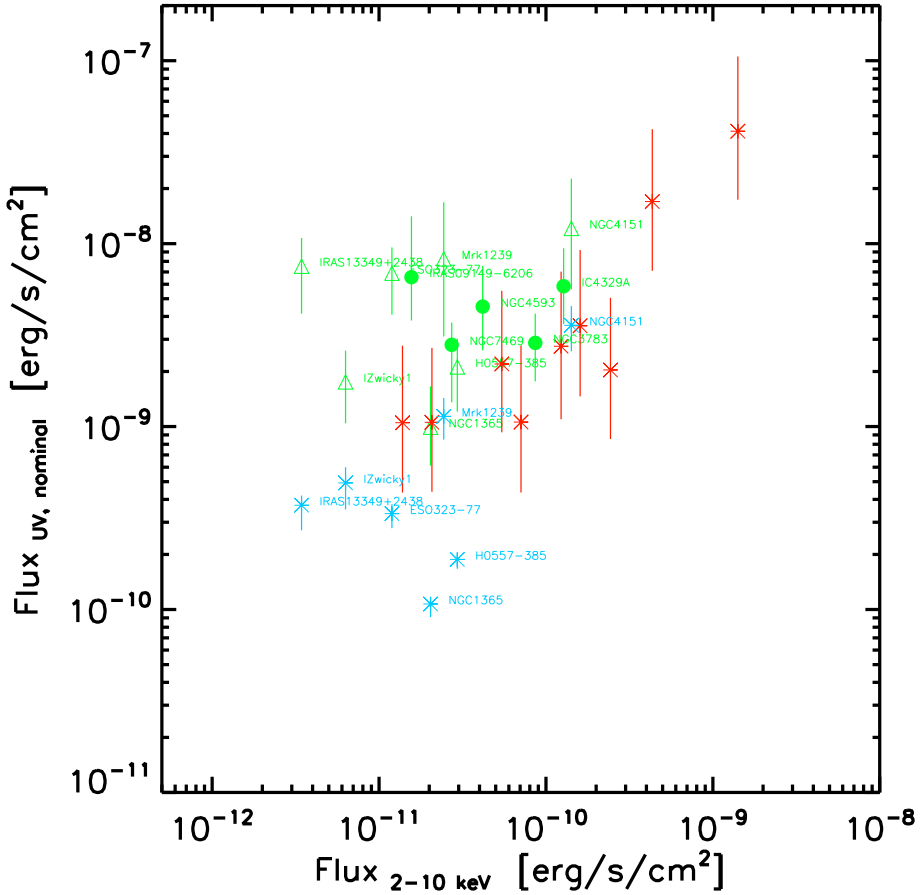
Figure 4.8: *Absorption-corrected $2-10$ keV X-ray flux versus nuclear UV flux estimated from models. The symbols indicate the median value for the estimated UV luminosities from their respective best-fit models, and the lines indicate the dispersion (68 % area) in the possible values. Type I galaxies that can only be fit with type A models (filling factors $0.4-1.4$ %) are given as filled circles. Those that can also be fit by type B models (filling factors $5.3-20$ %) are shown twice, with the model UV-flux values given as triangles (model A) and asterisks (model B). All type 2 galaxies are shown as asterisks.*

of obscuration, some of the observed type 1 sources may arise from high filling-factor geometries and some of the type 2 sources from low filling-factor geometries in a more complicated version of the Standard Model. In addition, of course, more than two geometries may actually be present.

6. The reduction of the silicate feature in our models is mostly caused by the large optical depth of the clouds and to a lesser degree to the shielding effect caused by non-silicate grains. For a low number of clouds, the reduction of the silicate feature is not caused by outer clouds blocking our view to the hot surfaces of the inner clouds.

4.9. Appendix

4.9.1. Models setup

The models used for our database of infrared images are built based on the approach described by [Schartmann et al., 2008]. These wedge-like clumpy torus models are one of many different torus models currently available, but their main advantage is that it is relatively easy to proceed from a model with only a few clouds to models with a large number of clouds that resemble the smooth distribution of continuous models better.

The models are built using spherical coordinates. The dust-free volume is defined by the half-opening angle θ_{op}, where clouds are only allowed to exist within the region of $\theta_{op} < \theta < \pi - \theta_{op}$. The cloud centers are distributed in equal volumes randomly along the azimuthal direction and polar angle in the allowed zone. The radial position of the clouds are randomly distributed and follow a power-law density profile $\rho_r = \rho_0(r/1\,\mathrm{pc})^\alpha$, where α is the density profile index and ρ_0 a normalization constant.

Dust clouds are spherical, homogeneously filled with dust, and all possess the same optical depth. The radius of the clouds is proportional to their radial position $a_{cl} = a_0(r/1\,\mathrm{pc})$, where a_0 is a constant value. The number of clouds of the model is determined by the filling factor. We define the filling factor as the ratio between the volume occupied by the clouds and the total volume of a spherical shell defined by the inner radius of the model and the radius at $1\,\mathrm{pc}$. Finally, the total amount of dust in the model is determined by normalizing the total density in order to obtain a fixed average optical depth at $9.7\,\mu\mathrm{m}$ along the equatorial plane.

Since the true mixture of grains in AGNs is not fully determined, we use a typical mixture of dust grains for the intrastellar medium, consisting of $62.5\,\%$ silicates and $37.5\,\%$ of graphites, where the percentages correspond to the mass fraction. In the case of the graphites, we take two different sets of optical constants: one third of our graphites is represented by graphites whose electric field vector oscillates in parallel to the crystal axis of the grain, and two thirds of the grains have a perpendicular oscillation. For the size distribution we use the classic MRN-model [Mathis et al., 1977]. Following [Schartmann et al., 2008], we use a decoupled computation of the temperature for each dust species and grain size. For each dust species we take five bins of different sizes, so we take in total 15 different dust density grids as input. Since the treatment of the dust temperature is decoupled for each grain size, we also implement the sublimation temperature of each grain type. We take a sublimation temperature of $1500\,\mathrm{K}$ for the graphites and $1000\,\mathrm{K}$ for the silicates.

To approximate the SED of the accretion disk, we use a broken power-law spectrum as described by Hönig et al. [2006], which is derived from quasi-stellar object

spectra [Manske et al., 1998]:

$$\lambda F_\lambda \approx \begin{cases} \lambda & \lambda < 0.03\,\mu\mathrm{m} \\ \mathrm{constant} & 0.03\,\mu\mathrm{m} \leq \lambda \leq 0.3\,\mu\mathrm{m} \\ \lambda^{-3} & 0.3\,\mu\mathrm{m} < \lambda. \end{cases} \qquad (4.1)$$

4.9.2.   Scaling of the observables

Our procedure for stochastically simulating a specific observation according to a specific set of model parameters is the following:

1. Choose a random cloud realization in accordance with the model parameters. Choose also an inclination angle θ and rotation angle ϕ on the sky.

2. Given the nominal model luminosity L_m, compute the cloud temperature distribution and three-dimensional radiation field.

3. Using θ and ϕ, project the emitted radiation at the three chosen wavelengths onto a plane with these inclination and rotation angles at the nominal distance D_m. Take the two-dimensional Fourier transform of these images to evaluate the model-correlated fluxes at all baselines BL_m. Evaluate especially the total zero-baseline $12\,\mu$m flux density $f_m(12)$ and also determine from the optical depth in the visual τ_V whether this realization would be classified as type 1 or 2.

4. Now consider each actually observed galaxy in the sample, with its actual observed values of D_s and $f_s(12)$. If it is the incorrect Seyfert type, skip this realization. Otherwise:

5. Move the model from D_m to D_s. This rescales all model apparent fluxes by $(D_m/D_s)^2$ and all angular sizes by D_m/D_s.

6. Adjust L_m to bring the scaled value of $f_m(12)$ to equal the observed $f_s(12)$; this rescales all angular sizes in proportion to $L_m^{1/2}$. The net effect of operations (5) and (6) is to multiply all the original model fluxes by ϵ, the ratio of $f_s(12)$ to the original value of $f_m(12)$, and all angular sizes by the $\sqrt{\epsilon}$.

7. For each observed baseline BL_s, look up the correlated flux in the 2D transform of the unscaled model at baseline length $BL_m = BL_s * \sqrt{\epsilon}$ (to account for the rescaled angular size) and multiply this value by ϵ (to account for the rescaled fluxes). This flux value can now be directly compared to the measured correlated flux at BL_s.
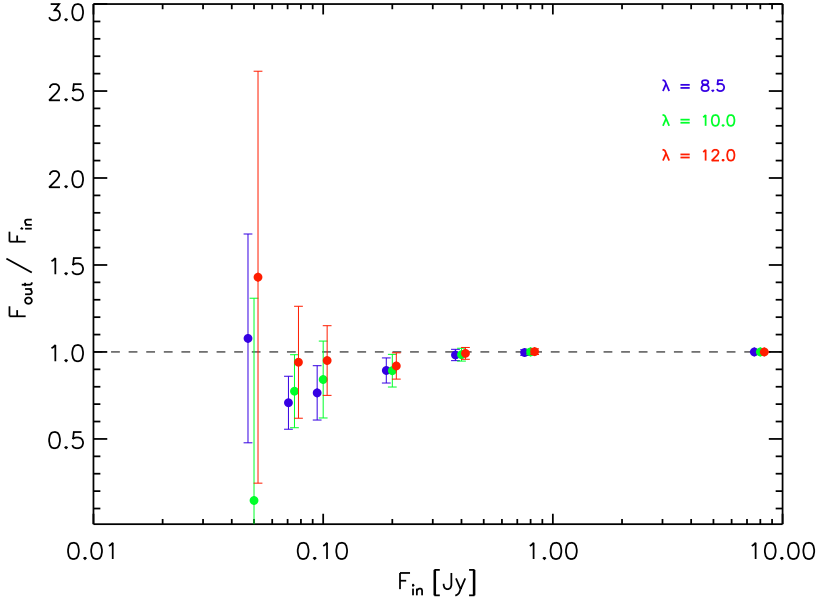
Figure 4.9: *Average fraction of the recovered flux F_{out} and the input flux F_{in} as a function of the input flux for our dilution experiment at different wavelengths (8.5 μm, 10.0 μm, and 12.0 μm. For each value of F_{in} the symbols for the three wavelengths have been shifted slightly for better readability. The average values were computed from the output fluxes obtained from 76 calibrators, and the errorbars represent standard deviation of the output fluxes.*

8. Repeat these steps for each cloud realization and for all the chosen values of θ and ϕ. The set of all the correlated fluxes for a given baseline represents the expected distribution of measured fluxes under the assumption of random distributions of these stochastic variables.

4.9.3. Correlation losses

The atmospheric phase jitter might lead to a reduction of the estimated correlated flux in our measurements. To estimate the amount of correlation losses caused during data reduction, we used a similar strategy as explained by Burtscher et al. [2012]. We simulated an observation of a weak target with a known flux to observe the difference between the input and the output flux. Since the data used for this work were reduced using EWS 2.0[4] and the dilution experiment previously reported by Burtscher et al. [2012] was done using the EWS snapshot version 2012 January 25, we repeated

---

[4]EWS is available for download from http://home.strw.leidenuniv.nl/ jaffe/ews/index.html
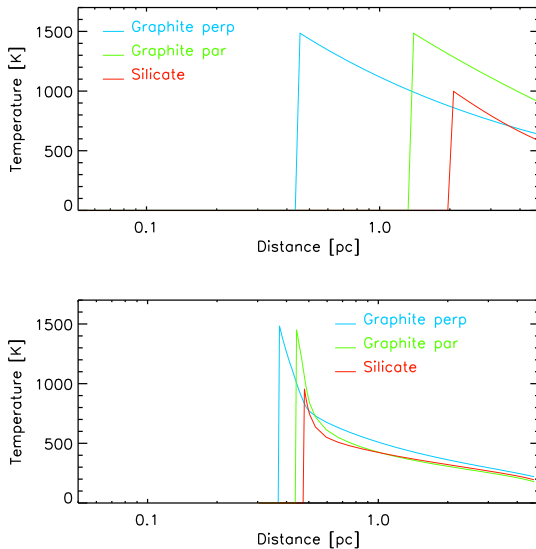
Figure 4.10: *Temperatures for the three smallest grain sizes of each species in a shell with a radial optical thickness of $\tau_{9.7} = 10^{-4}$ (top) and $\tau = 8$ (bottom). The colors indicate the different species of grains: blue - graphites $\perp$, green - graphites $\parallel$, and red - silicates.*

this experiment with the updated version to determine possible changes. For our experiment, we took the raw data of a bright target with known flux, a calibrator in our case, multiplied the input flux by a factor $f < 1$ and added artificial noise to the data. After performing this process several times, we obtained an estimate of the amount of losses in the flux due to correlation losses.

We performed this dilution experiment with 76 calibrators observed in different nights and diluted to simulate weak targets with $50 - 8000$ mJy of correlated flux. The losses relative to the highest flux (8 Jy) were determined at three wavelengths of 8.5, 10.0, and 12.0 μm. Figure 4.9 shows the losses at these three wavelengths, and for the weak sources with fluxes < 400 mJy these losses clearly become more significant at the short wavelength range (closer to 8 μm), while the losses are moderate above the 12 μm. We used this information to correct the average correlated fluxes of the sources for this work. For the source with high correlation losses we took the average correlated flux obtained after the data reduction and multiplied it by the decorrelation correction factor obtained from our dilution experiment.

4.9.4. Dust sublimation

The radiative transfer code RADMC-3D does not include an internal computation to account for dust sublimation. To include dust sublimation in our models, we slightly modified the code. Each time a photon package enters a cell, it increases the energy of the cell and thus increases the temperature of the dust of this cell. When the dust in the cells exceeds the dust sublimation temperature, the dust inside the
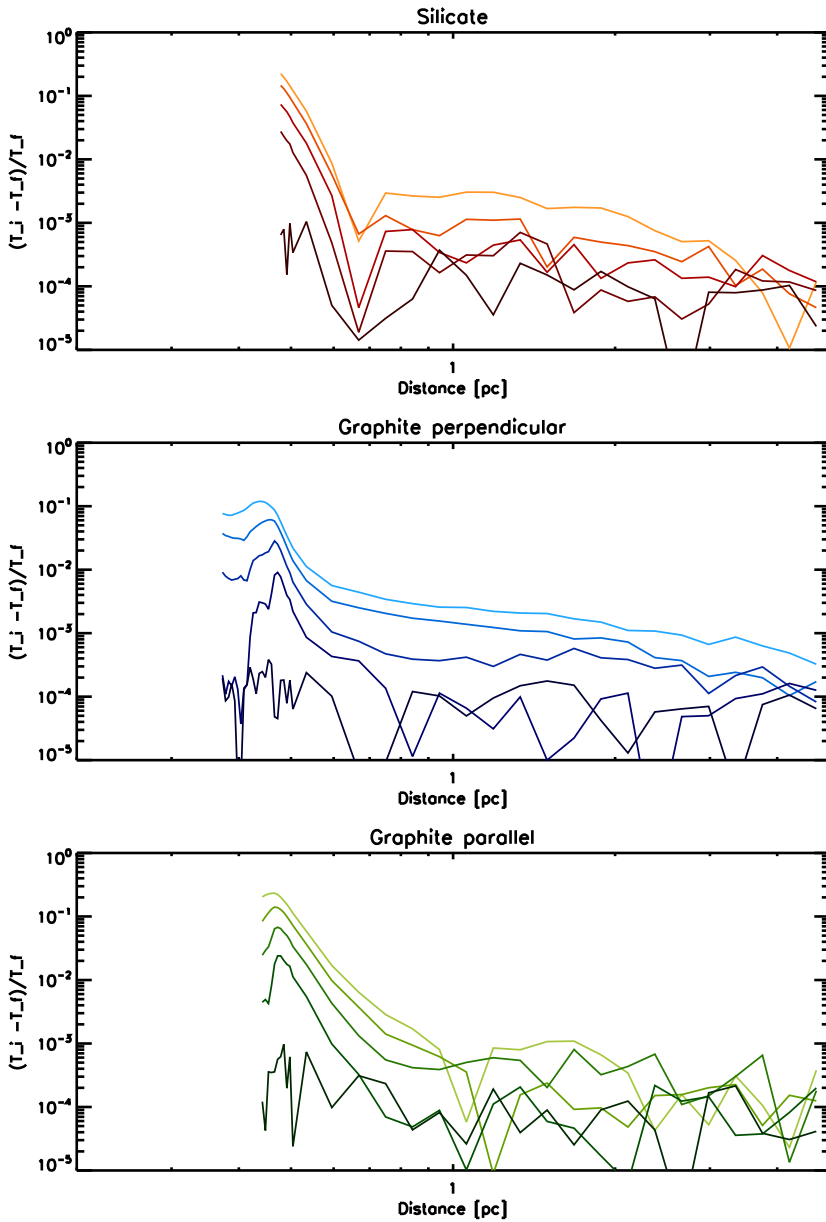
Figure 4.11: *Convergence of the temperature for the three smallest grains. Each line indicate the relative difference after each iteration. The darker the color, the higher the number of iterations.*

cell is completely removed. To accurately estimate the temperature of the system using dust sublimation, we performed an iterative process for which the code several times computed the temperatures and removed the corresponding cells. When the differences between different iterations were below a certain tolerance (we took a value of 5 %), we performed a last computation without removing any dust in the cells to ensure the conservation of energy in the system. To show how our implementation of the dust sublimation works in different situations we show examples of an optically thick and optically thin case. In Fig. 4.10 we show the temperature of the three smallest grains of each species for a spherical shell with $\tau_{9.7} = 10^{-4}$ and $\tau_{9.7} = 8$, respectively. Both shells have an initial inner radius of 0.3 pc and an outer radius of 5 pc. We can observe clearly that in the optically thick case, the temperature rises more quickly and the sublimation radius for the three species are closer than in the optically thin case. We made sure that we had enough cells close to the inner radius to obtain an accurate solution. In Fig. 4.11, we show for the optically thick case, the relative differences between each iteration and our final computation. After a few iterations, the temperature in every cell reaches a relative difference below our tolerance value.

4.9.5. Acceptance levels

For our method we used linear transformations computed for each model to remove the mean values, normalize the variance, and remove correlations. We expect that if our models agree with the observational data, the final distribution of the data points have a zero mean and variance equal to one. To test if this is true for every model, we applied a χ^2-test to the sample mean (μ) and sample variance (s^2) of the normalized measurements,

$$\chi^2 = \left(\frac{\mu}{\sigma_{mean}} \right)^2 + \left(\frac{s^2 - 1}{\sigma_{var}} \right)^2, \tag{4.2}$$

where σ_{mean} and σ_{var} are the computed variance for the sample mean and the sample variance, respectively. These two quantities were computed from the distributions of each model. Although the distribution produced by our models might not be Gaussian distributions, when we combine all of the measurements to compute the final quantities, the resulting distribution should be more less similar to a Gaussian distribution, according to the central limit theorem. Therefore, we used the probability values assigned for the χ^2-distribution to derive the level of acceptance for each model.

To test if our assumptions are valid, we performed a consistency test. We took a particular model and created 200 samples with measurements of 20 simulated objects using sparse (u, v) coverages and simulating uncertainties of 10 %. For each sample
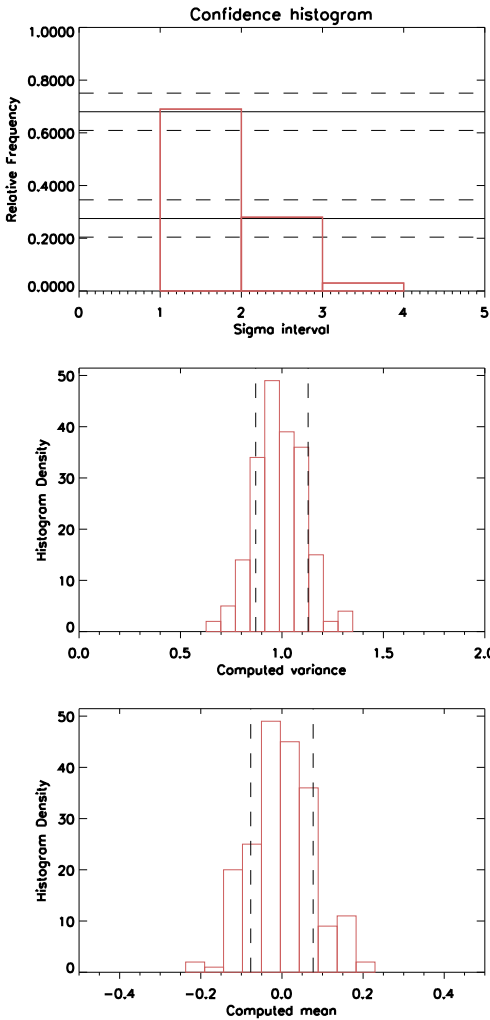
Figure 4.12: *Top) Histogram showing the frequency of our sample in terms of the σ areas. The lines indicate the 68 % and 27.5 %, respectively. The dashed lines give the expected uncertainty for 200 experiments. Center and bottom) Histogram of the sample mean and variance of the normalized measurements for the 200 experiments.*

we applied our test with the model that was used to create the simulated samples. In Fig 4.12 we show the distribution of the sample mean and variance for all the samples. We also show that we can safely build our confidence intervals assuming the probabilities for a normal distribution.

CHAPTER 5

Properties of the dusty clouds of AGNs

N. López-Gonzaga, M. Schartmann, W. Jaffe

In preparation

Abstract

We aim to understand the role of the optical depth, viewing angle and the location of the clouds and determine the relevance of individual cloud properties. First, we investigated the mid-infrared quantities of spherical dust clouds such as the strength of the silicate feature and the spectral index. Then, by locating individual objects in the plane of the spectral index and the strength of the silicate feature, we determined origin of the silicate feature in the real objects. We find that the abscence of a silicate feature in emission is most likely to be caused by large optical depths and obscuration effects. The lack of silicate grains caused by a sublimation effect reduces the silicate feature, but the sublimation of silicate grains is only relevant for clouds with low optical depths and at distances of $< 5\,r_{sub}$. Sublimation effects are negligible if a cloud has an optical depth > 8 at $9.7\,\mu$m. In Type 1 AGNs, the observed shallow silicate feature in emission is caused by having a low amount of clouds at the inner radius. Additionally, the spectral index seems to be strongly connected with the location of the clouds that dominate the infrared emission, the relation of the spectral index with the optical depth of the clouds is less strong. We concluded that the spectral index of Type 1 objects is mostly determined by the average location of the clouds in the dusty environment. Our results suggest that the differences between Type 1 objects are mostly due to a change in the average location of the clouds.

5.1.   Introduction.

Within the Unified Scheme of active galactic nuclei (AGN) apparent differences in the properties of AGNs are interpreted in terms of the viewing angle towards a similar intrinsic underlying structure [Antonucci, 1993; Urry & Padovani, 1995]. In this unified model, an optically thick circumnuclear dusty structure absorbs a significant fraction of the optical/UV luminosity of the active nucleus and re-radiates this energy at infrared wavelengths, giving rise to the characteristic peak in the spectral energy distribution of many AGNs [Sanders et al., 1989]. As a consequence, the observable spectra of the dusty nuclear region of AGNs depends on both the underlying emission sources and the subsequent obscuration and reprocessing of their light by material along the line of sight.

One of the challenges of the unified model has been to reconcile the observed infrared emission with that predicted from the absorbing torus. High complex dusty clumpy models have been developed to give an explanation for the diversity of observed spectra [e.g., Dullemond & van Bemmel, 2005; Hönig et al., 2006; Nenkova et al., 2008a,b; Schartmann et al., 2008; Heymann & Siebenmorgen, 2012; Stalevski et al., 2012]. This models can be effectively used to perform spectral decomposition as they provide accurate estimates for the contribution of the AGN, but when studying specific physical properties of the dusty environment results obtain from these models need to be taken with precaution due to their high degeneracy. While the true shape of the dusty emission is still a matter of debate (e.g., disk wind-like structure or torus-like structure), it might still be possible to extract physical or geometrical information about the dusty structure by independently analyzing some spectral observables.

According to the Standard model of AGNs, Type I objects are typically observed from a dust free line of sight. This means that in Type I objects the clouds with a face directly heated by the AGN should be more visible and self-absorption effects or emission from indirectly heated clouds is probably less relevant compared to Type II objects. Indirectly heated clouds are mostly heated by the diffuse radiation from the surrounding clouds and it was shown by [Nenkova et al., 2008a] that their flux contribution compared to the direct heated clouds can be relatively small. Thus, it is possible to assume that the emission from Type I objects could be mostly determined by the emission from directly heated clouds and therefore the observed radiation might be strongly related to the real cloud density distribution and cloud properties [Kishimoto et al., 2011a]. In principle, if the bulk emission of the dusty environment is strongly determined by the emission from directly heated clouds, we could approximate the properties of the dusty emission with the properties of simple cloud models.

The aim of this work is to analyze the infrared environment of AGNs by using
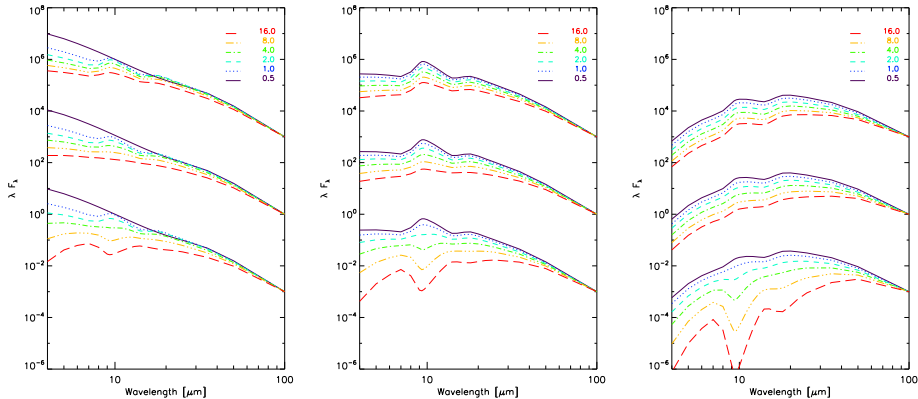
Figure 5.1: *SEDs of the clouds at different distances (Left) r_{sub}, (Center) $5r_{sub}$ and (Right) $25r_{sub}$. The SEDs have been normalized by their flux at $30\,\mu m$. The different colors and lines indicate the optical depth of the cloud. On each plot, the top set of spectra are computed from looking directly at the hot face, the middle set by looking at a side, and the bottom set by looking at the cold face.*

simple but representative models of clouds to describe the observed quantities in the mid-infrared regime, such as the spectral index or the strength of the silicate feature. For this work, the observed properties of the clouds are investigated by changing three parameters: the optical depth, the inclination and the distance to the heating source. The outline of this paper is as follows. In Section 2, we describe the archival sample and the dusty cloud models. The observed mid-IR properties of the clouds are explained in Section 3. In Section 4, the extension of Type I objects is examined motivated by the result of individual clouds. In Section 6, we summarize our results.

5.2. Tracing the mid-infrared emission of Type I objects

5.2.1. Subarcsecond mid-infrared observations

Mid-infrared subarcsecond-resolution observations have provided a better insight of the nuclear dusty structures in AGNs [see, e.g. Asmus et al., 2014; Burtscher et al., 2013, and references therein]. Space instruments typically have better sensitivity and higher spectral resolution than ground telescopes, but with their low spatial resolution contamination by other sources cannot be excluded [see, e.g. Buchanan et al., 2006; Hernán-Caballero et al., 2015]. In order to isolate the infrared emission of the dusty nuclear region and investigate its intrinsic properties, high angular resolution

observations or accurate decomposition of the spectral energy distribution (SED) are
required.

In the following sections, mid-infrared data of a sample of Type 1s will be ana-
lyzed. Single-aperture mid-infrared spectra of the nuclear region of a group of AGNs
was collected from previous work by Hönig et al. [2010] and Burtscher et al. [2013].
The objects were selected mainly due to their available mid-infrared interferometric
observations which resolve the nuclear dusty region. Within the mid-infrared regime,
the acquired spectrum provides two relevant quantities: the strength of the silicate
feature and the spectral index.

To quantify the silicate feature, a common quantity for the strength of the feature
at $9.7\,\mu$m is defined by using the following formula,

$$S_{9.7} = \ln \frac{F_{obs(\lambda)}}{f_{cont}(\lambda)} \tag{5.1}$$

where F_{obs} is the observed flux and F_{cont} the flux of the underlying continuum eval-
uated at wavelength λ. Positive values of $S_{9.7}$ indicate that the silicate feature is in
emission, while negative values indicate absorption feature. To determine the contin-
uum emission from the observed spectrum, it is usually common to fit splines between
several intervals along the spectrum [e.g., Levenson et al., 2007; Sirocky et al., 2008].
While this works well for space observations due to their large wavelength range, the
wavelength range of the N-band (8-$13\,\mu$m) is too narrow to apply such techniques.
Instead, for this work the continuum emission at $9.7\,\mu$m is obtained by doing a linear
interpolation $9.7\,\mu$m using the extreme values of the spectrum (8.5 and $12.5\,\mu$m).

To characterize the temperature or slope of the continuum, the spectral index is
computed for each object by using the formula,

$$\alpha = \frac{\ln\left[\,F_\nu(\nu_1)/F_\nu(\nu_2)\,\right]}{\ln(\nu_1/\nu_2)}, \tag{5.2}$$

where $\nu_1 = 3.66 \times 10^{13}$ Hz and $\nu_2 = 2.4 \times 10^{13}$ Hz which correspond to $\lambda_1 = 8.2\,\mu$m
and $\lambda_2 = 12.5\,\mu$m, respectively.

5.2.2.   Modeling dusty clouds

In this section, the setup and methods for computing the temperature and SEDs
for the individual dusty clouds are presented. Several dusty clouds are modeled
in order to characterize their properties and to investigate possible implications for
the observed AGNs. The numerical computation of the temperature and surface
brightness distribution of the dusty clouds were done using the radiative transfer
code RADMC-3D[1].

---

[1]http://www.ita.uni-heidelberg.de/ dullemond/software/radmc-3d/

Dusty clouds for this work are based on the dusty clouds developed for the 3d torus models of Schartmann et al. [2008]. The clouds are assumed to have spherical shapes defined by the cloud radius a_{cl}. The radius a_{cl} is proportional to its distance d_{cl} from the heating source, $a_{cl} = \beta\,(d_{cl}/1\,\mathrm{pc})$, where β is a constant value ($\beta = 0.2\,\mathrm{pc}$ for this work). The cloud is homogeneously filled with dust and the total amount of dust is determined by the total optical depth at $9.7\,\mu\mathrm{m}$. For this work a range from optical thin to optically thick clouds is covered.

The dust grains are assumed to be spherical with a size distribution described by the typical power law $n(a) \propto a^{-3.5}$ [Mathis et al., 1977]. This size distribution is the same throughout the whole system. The mixture of dust is a standard galactic composition of 53% astronomical silicates and 47% graphite For clouds close to the sublimation radius, the sublimation of grains implies removing a a certain quantity of the grains and as a consequence the composition of the grains might differ in certain regions of such clouds. The optical properties have been derived on the basis of Mie scattering using the Mie scattering algorithm published by Bohren & Huffman [1983].

Additionally to varying the optical depth, each cloud is modeled at different distances, $d_{cl} = 1, 5, 25, 75\,r_{sub}$, where r_{sub} is the sublimation radius of the largest graphite of the dust mixture.

Finally, the heating source has an SED formed by a broken power law, characteristic to the accretion disk in AGNs [Hönig et al., 2006; Manske et al., 1998]:

$$\lambda F_\lambda \approx \begin{cases} \lambda & \lambda < 0.03\,\mu\mathrm{m} \\ \mathrm{constant} & 0.03\,\mu\mathrm{m} \leq \lambda \leq 0.3\,\mu\mathrm{m} \\ \lambda^{-3} & 0.3\,\mu\mathrm{m} < \lambda. \end{cases} \tag{5.3}$$

5.3. Results

Spherical dusty clouds with a mixture of silicates and graphites were simulated at several distances and optical depths according to the description given in the previous section. The sublimation of dust grains was implemented by removing the dust grains that reached their sublimation temperature in the same way as it was done in Chapter 4. In the following subsections the properties of the dusty clouds will be examined with more detail.

5.3.1. The spectral energy distribution

Fig. 5.1 shows the SED for clouds with different optical depths and relative distances at three different inclinations[2]. One clear characteristic is that the slope of

---

[2]The angle ϕ for the inclination is defined as the angle between the line of sight and the line that connects the heating source with the center of the cloud. The three inclinations are defined as, a
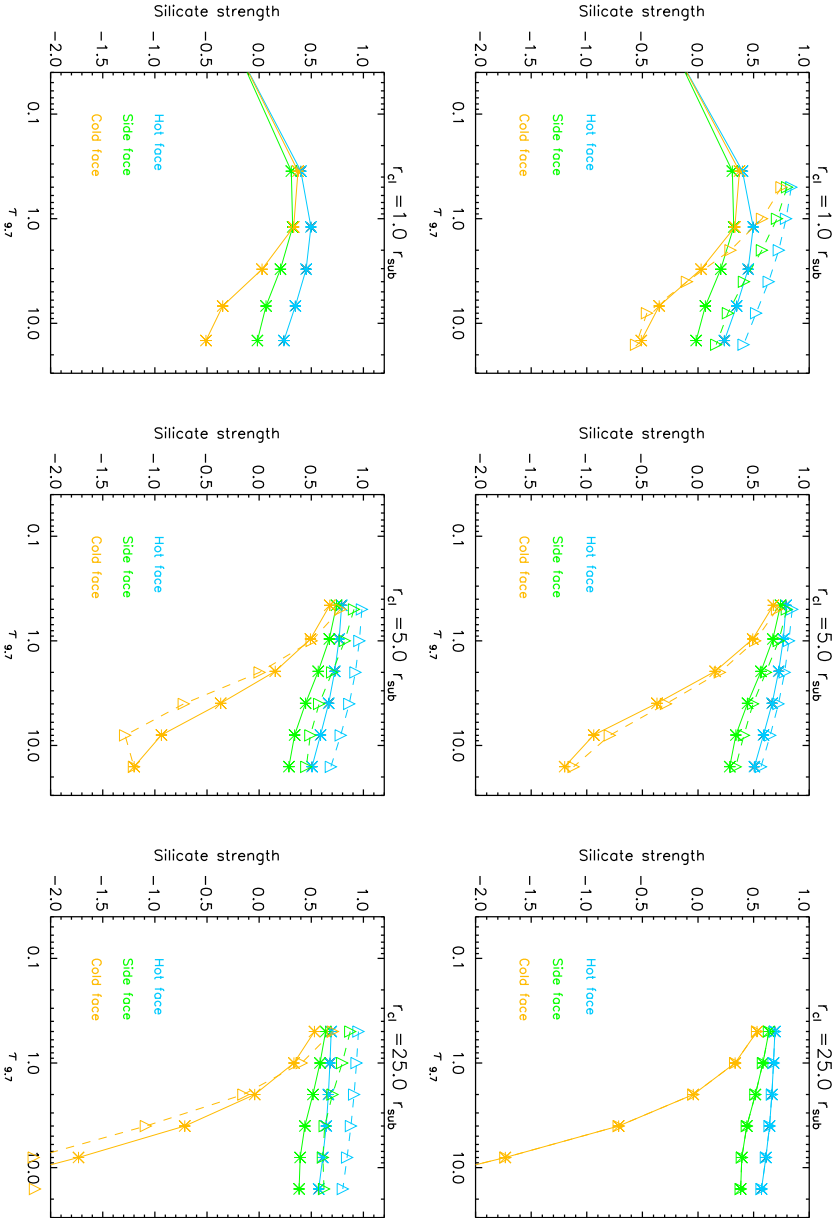
Figure 5.2: *The observed silicate strength as a function of the location of the cloud, the optical depth and inclination. The colors indicate the different lines of sight. (Top row) The quantities traced by the solid lines are computed including sublimation effects, while for the dashed lines we assume an arbitrary sublimation temperature. (Bottom row) In this case the quantities traced by the dashed lines are computed using a pure silicate mixture of grains, while the dashed lines are computed with our standard grain mixture. Both were computed including sublimation effects.*

the curves depends greatly on their relative distance from the central heating source. In general, the closer the clouds are to the central source, the bluer the spectrum will be due to the higher temperatures reached by the directly heated face.

Aside from the relative distance, the optical depth and inclination also play a role in the determination of the SED, especially for clouds at small distances where the temperature differences between the hot and cold face become quite large for high optical depths and inclinations. The temperature inside optically thin clouds is determined by the radiation field of the heating source, where the infrared radiation emitted by the dust manages to escape along every direction. For optically thick clouds, the temperature is highest at the directly heated face and drops quickly inside the cloud.

The silicate feature in emission is the largest for optically thin clouds at intermediate radius ($\approx 5\,r_{sub}$). Clouds close to the sublimation radius do not produce large emission features due to the absence of silicates caused by sublimation effects, while for clouds at larger radii the silicate feature in emission is not so strong due to a contrast effect. In the later case, if the continuum emission is dominated by cold emission then by increasing the optical depth the continuum emission of the cold emission will become higher than the total flux of the silicate feature in emission and wash out the strength of the silicate feature. The increasing temperature gradient caused by the optical depth determines the strength of the observed silicate feature and the transition from the silicate feature in emission to absorption can be linked to the inclination angle. In the following subsection the behavior of the silicate feature will be explained as well as the consequences caused by the implementation of the sublimation temperature.

Typical mid-infrared spectra of Seyfert Type 1 galaxies do not show prominent silicate features in emission [see Hönig et al., 2010; Alonso-Herrero et al., 2011; Burtscher et al., 2013]. This means that without including any further complexity due to multiple clouds, the mid infrared spectra of Seyfert Type 1s could only be explained by hot clouds without any silicate grains or high optical depth clouds at intermediate inclinations where neither the hot face or cold face are completely visible.

5.3.2.   Clouds and the sublimation of grains

Simulations of clouds implementing the sublimation temperature were developed and compared with simulations without implementing the sublimation temperature. Switching off the implementation of the sublimation can also be seen as using dust grains with an infinite sublimation temperature. The analysis of this section is fo-

---

direct view of the hot face at $\phi = 0°$, a side view at $\phi = 90°$ and a view towards the back of the cloud at $\phi = 180°$.

cused towards the strength of the silicate feature since this is the most visible difference between the two approaches.

In the top row of Fig. 5.2 we show the silicate strength as a function of the optical depth for clouds at various distances implementing the sublimation temperature (solid lines) and with an arbitrary sublimation temperature (dashed lines). For both implementations, increasing the optical depth enhances the differences in the silicate strength between the hot face ($\phi = 0°$) and the cold face ($\phi = 180°$). As the angle of the sight-line changes from a view of the hot face towards the cold face, the temperature gradient changes from an increasing gradient towards the sight-line (producing an emission feature) to a decreasing gradient (producing an silicate in absorption).

Differences due to sublimation effects are stronger for clouds located close to the heating source and become negligible for clouds at distances larger than $5\,r_{sub}$. At large distances the radiation is not sufficient enough to allow the grains reaching their sublimation temperature. For clouds located at small distances, the silicate feature in emission is in general lower for clouds with sublimation than for clouds without sublimation of the grains. For clouds at a distance of $1\,r_{sub}$ and low optical depths, the density of graphites is not sufficient enough to shield the silicates from the radiation of the heating source and prevent the silicates from sublimating. In such clouds, a large fraction if not all of the silicates in the exposed layers will therefore sublimate. For clouds with large optical depths, the graphites absorb most of the emission at the exposed layers and prevent the silicates from a direct exposure of the radiation. Increasing the optical depth of the clouds reduces the thickness of the layer where the silicates are sublimated and therefore differences between models with and without the sublimation effects become negligible for large optical depths. This is clearly observed in the top row of Fig. 5.2, the difference in the strength of the silicate feature is almost a factor of 8 at low optical depths, while it is only a factor of ≈ 1.3 for optical depths values around $\tau_{9.7} = 16$. Not implementing the sublimation effects in dusty torus simulations is only justified as long as the optical depth of the clouds is $\gtrsim 8$ at $9.7\,\mu$m

5.3.3.   Graphites and the silicate feature

While the real dust mixture is not yet fully determined it is always assumed that it resembles the mixture of the interstellar medium. As explained in the previous section, graphite grains are important to prevent the silicate grains from sublimating at relative distances where if the silicates where alone they would not survive. To investigate further if the graphites grains play an important role in determining the strength of the silicate feature, simulations using pure silicate grain clouds were developed and compared to dusty clouds with the standard mixture. In both cases the sublimation has been implemented.
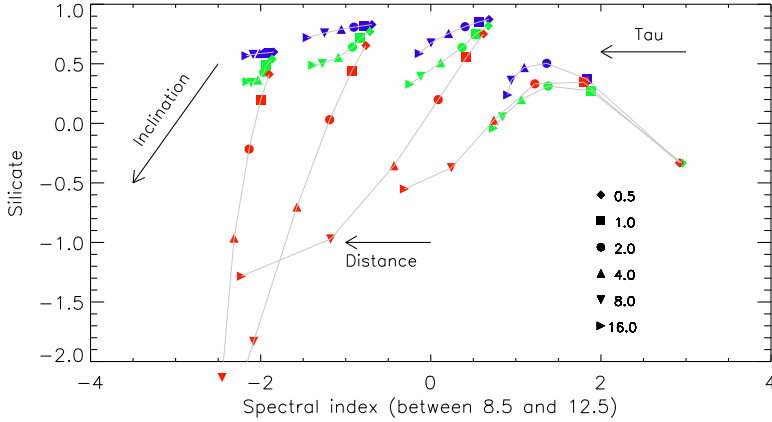
Figure 5.3: *Strength of the silicate feature and the spectral index for directly heated clouds. The color of the symbols indicate the value of the inclination, blue for lines of sight towards the hot face, green for a view of the side of the cloud and red for a view of the back of the cloud. The multiple symbols indicate the optical depth of the cloud. The four different group of curves visible in the plot represent the properties of the clouds at four different distances, from right to left the clouds are located 1, 5, 25, 75 r_{sub} from the central heating source.*

The bottom row of Fig. 5.2 shows the differences between clouds composed of pure silicates (dotted lines) and a clouds with a mixture of silicates and graphites (solid lines) both implenting with the sublimation temperature . Clouds with graphites have slightly lower silicate features in emission than pure silicate clouds but the general trends as a function of the optical depth and inclination are quite similar. This means that the reduction of the silicate feature in emission, for clouds at intermediate distances, achieved by increasing the optical depth is mainly a contrast effect and in a minor degree dependent on the mixture of grains.

The major difference is seen for clouds close to the sublimation radius. In the left bottom plot of Fig. 5.2, the absence of the solid line indicates that pure silicate clouds cannot exist at the sublimation radius of the graphites. Pure silicate grain clouds do not have graphite grains that prevent the silicates from sublimating. This result is relevant to explain the existence of clouds at small distances that could influence the amount of infrared emission produced at shorter wavelengths or to explain the small inner radius obtained from reverberation techniques.
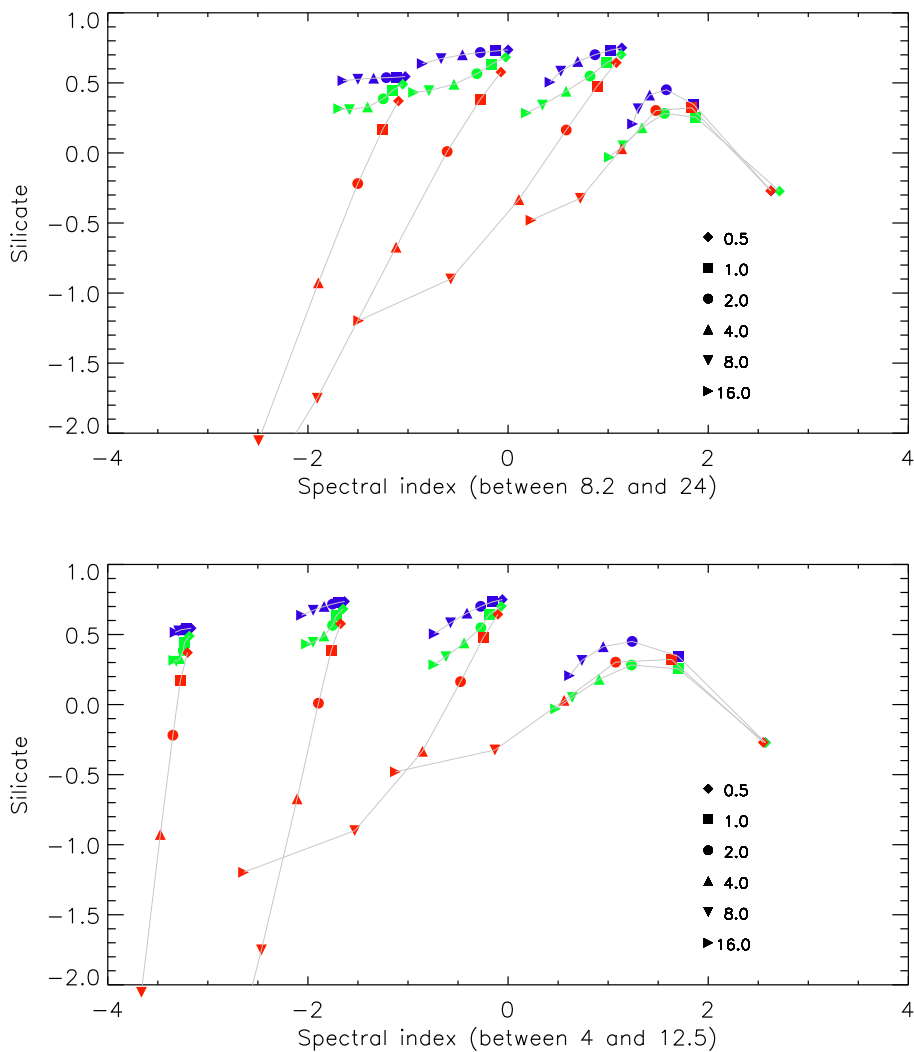
Figure 5.4: *Similar to Fig. 5.3, except that the spectral index is built using different wavelength ranges.*
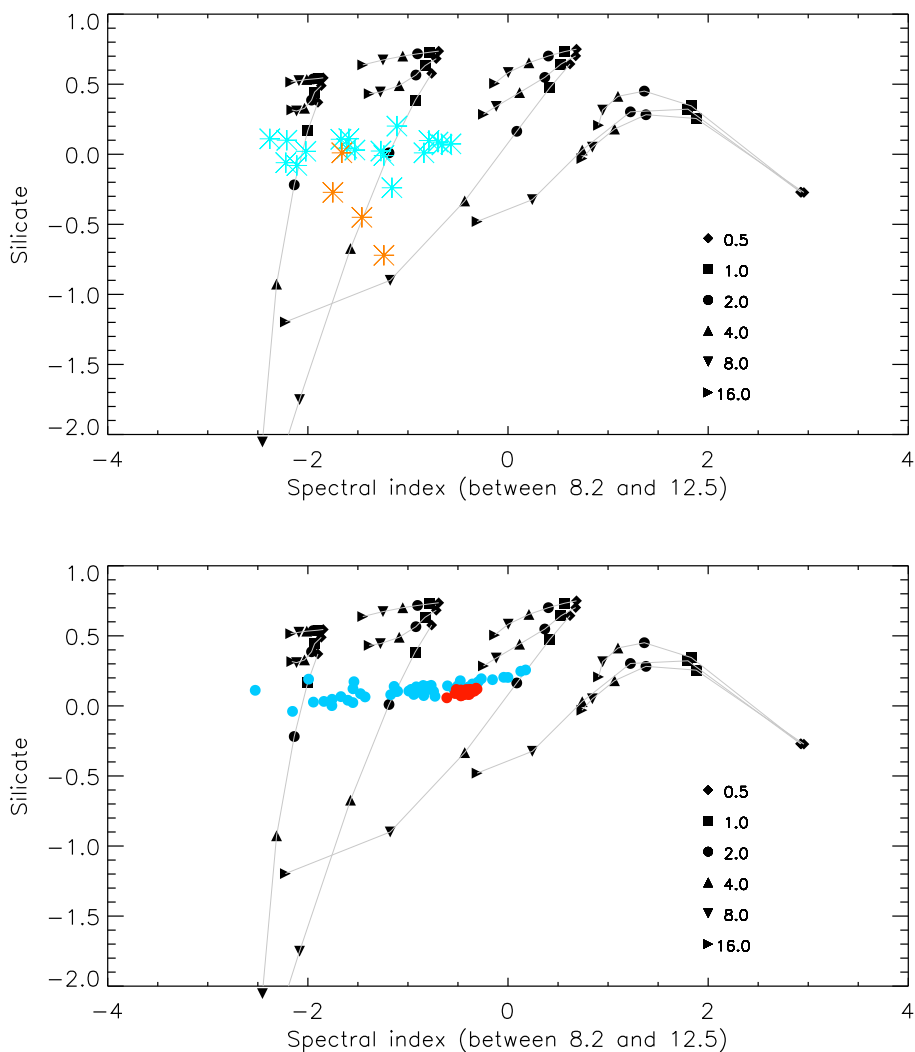
Figure 5.5: *Comparisson between the diagnostic plot and (Top) real data and (Bottom) model. (Top) The observed data is given in color, while the quantities from the modeled clouds are given in black. The color indicates the Seyfert Type of the objects, light blue are Type I objects and orange are Sy1I objects. (Bottom) Model predictions from LGJ15 are given in colored dots. The blue dots are the predictions for Type I objects from their model with a low number of clouds. Red dots are the predictions for Type I objects from a model with a higher number of clouds at the inner radius.*

5.3.4.   Characterizing the emission of directly heated clouds

After analyzing the strength of the silicate feature, the next step is to see if it possible to extract information from observable measurements in order to retrieve properties of the clouds. To do so the spectral index (using the 8.5 and 12.5 μm fluxes) was computed and plotted in Fig. 5.3 against the silicate strength for clouds at different distances, optical depths and inclinations. From Fig. 5.3 it is clear that for direct heated clouds the slope of the spectrum is strongly related to their relative distance from the heating source. The spectral index is higher for clouds closer to the sublimation radius, while it decreases for clouds at large distances.

The line of sight or inclination produces a minor decrease of the spectral index but it has a major impact on the strength of the silicate feature, especially when the optical depth becomes larger. Finally, an increase in the optical depth produces a slightly decrease of the spectral index but it enhances the strength of the silicate feature in absorption for large inclinations. For low inclinations the optical depth lowers the silicate feature in emission only slightly. From Fig. 5.3 it is clear that the spectral index depends greatly on the distance of the clouds while the inclination and optical depth determine the strength of the silicate feature.

For completeness, two additional plots are built using different wavelength ranges when computing the spectral index. Fig. 5.4 shows the diagnostic plot for a spectral index using the flux values at 8.2 and 24 μm and second one using the flux values at 4 and 12.5 μm. Including longer wavelengths does not introduce additional information. A similar behavior is observed for a spectral index using $8.2 - 24\,\mu$m and 8.2 and 12.5 μm. Instead, using shorter wavelengths, in this case 4 μm fluxes, reduces the effect of the optical depth on the spectral index especially at large inclinations, see bottom plot of Fig. 5.4. Additionally, the range of spectral indexes gets broader for the same values of distances. Including L- or M-band information allows to determine a more clear relationship between the spectral index and the location of the clouds.

5.4.   Discussion

5.4.1.   A diagnostic of the extension of Type I objects

The observed quantities for the Type I objects described in Sect. 2 have been plotted against observed quantities of the dusty clouds in Fig. 5.5. No Type 1s in the sample show moderate or strong silicate features in emission or absorption. Only the three Narrow Line Seyfert 1s (Sy1i) show a shallow silicate feature in absorption. In Sy1i objects, the presence of an absorption feature could be intrinsic of the nuclear dusty environment but obscuration due to the host galaxy cannot be ruled out. For example, in the Sy1i objects NGC5506 and MCG-5-23-16 the silicate feature in
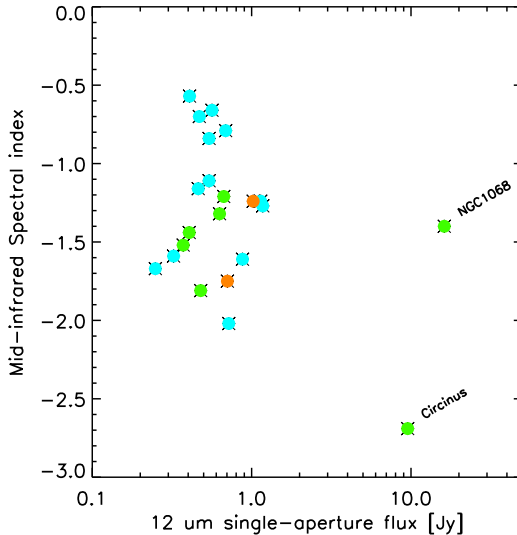
Figure 5.6: *Spectral index versus the 12 μm single-aperture flux. The color of the symbols indicate the Seyfert Type: blue dots are Type 1 objects, green dots are Type 2 objects and orange dots are Sy1i objects.*

absorption could also be explained by the presence of an observed dust lane that extends all the way out to parsec scales.

For the objects shown in the top plot of Fig. 5.5, the distribution of the spectral index goes from a steep spectral index (-2.5) to a flat spectral index (0), while the silicate feature remains almost constant. Using this diagnostic plot the change of the spectral index can be explained by observing clouds at inclinations between $\phi = 90$ and $\phi = 180$ and varying their relative distance. The optical depth could in principle also play a role in the determination of the spectral index but to reproduce the observed spectral indexes extremely large optical depths are required. Therefore, it seems more likely that the change of the spectral index is attributed to a distance effect.

If the emission from each object is indeed determined by the location of the directly heated clouds, then the large dispersion of the spectral index indicates that the bulk of the emission for objects with spectral index close to 0, is generated from clouds at a few sublimation radii $(\sim 5\,r_{sub})$, while the emission from objects with steep spectral index comes from clouds at larger distances $(> 25\,r_{sub})$, making them more extended than the objects with a higher spectral index.

5.4.2.   Torus models

The explanation of the spectral index given in the previous subsection using single clouds might provide a quick diagnostic for the extension of Type I objects. In reality the dusty environment of AGNs is more complex than just a simple cloud. But to
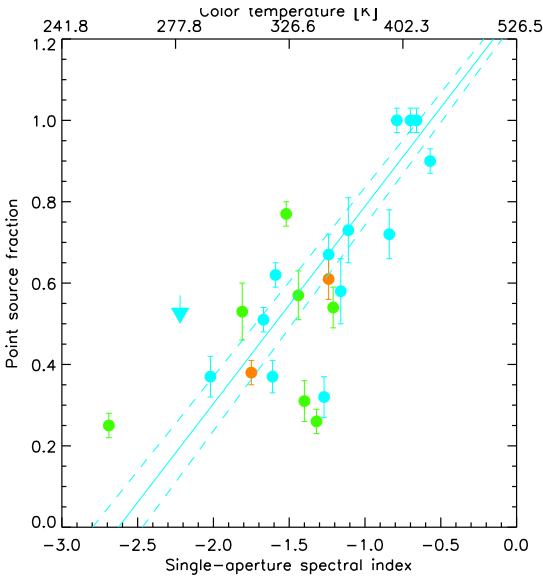
Figure 5.7: *Point source fraction of the rescaled objects (see text for additional information) against single-aperture spectral index. The color of the symbols indicate the Seyfert Type: blue dots are Type 1 objects, green dots are Type 2 objects and orange dots are Sy1i objects. The blue solid line represents the best linear fit to the objects, excluding Type II objects. The dashed lines delimit the 1-σ area of the best linear fit.*
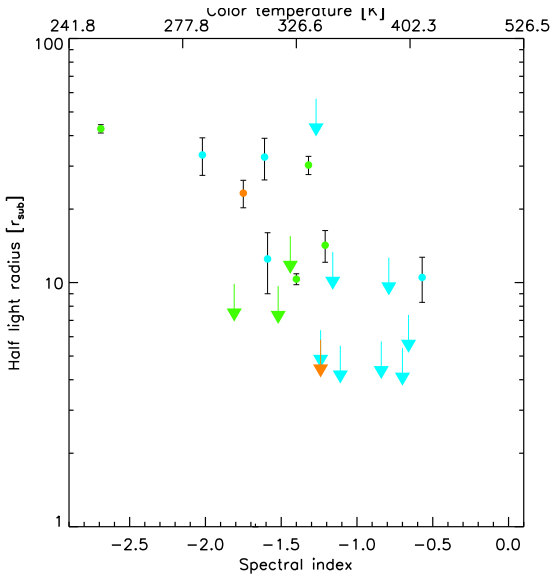
Figure 5.8: *Half-light radius obtained from mid-infrared interferometry against spectral index. The color of the symbols are the same as in Fig. 5.7. The arrows indicate the upper limits for the half-light radius.*

gain trust in the diagnostic plot, it is possible to use more complex clumpy torus geometries and observe where they fall in the diagnostic plot.

Using clumpy torus models, Lopez-Gonzaga & Jaffe (2015; submitted, hereafter LGJ15) recently tried to reproduce the mid-infrared interferometric observations of a sample of AGNs. According to their results, several Type II and Type I objects could share similar properties and could be described with a densely populated clumpy torus model as described by the standard model of AGNs. But a reasonable fraction of Type I objects could have an intrinsic different structure. In order to explain observations from a subset of Type I objects a clumpy environment with a lower density of clouds at the inner radii and with a limited amount of clouds had to be used.

The two best fit models used in LGJ15 have been plotted in the bottom plot of Fig. 5.5 against the diagnostic plot using a number of lines of sight that correspond to Type I objects. The torus model with a higher number of clouds at the inner radius has a steeper radial distribution of the clouds towards the center and the SED is expected to be dominated by clouds located at a few sublimation radius. The spectral index distribution produced by this model (red circles in Fig. 5.5) is in good agreement with clouds at around $5\,r_{sub}$ from the diagnostic plot. Since the inner environment of this model is filled more densely, the differences caused by the random location of the clouds are quite small, and therefore the distribution of spectral index is quite narrow. The spectral index distribution from the model with a small number of clouds in the inner regions (blue circles) has a larger spread of values due to the stochastic location of the clouds, with directly heated clouds dominating at several distances. Therefore, we expect that the objects with a lower spectral index are more extended and dominated by cooler dust emission.

5.4.3. Resolving the nuclear dusty emission

According to Fig. 5.3, the distribution of the spectral index is mostly determined by the location of the clouds rather than an obscuration effect. Objects with a low spectral index are more extended since they are dominated by clouds at larger distances, while objects with large spectral indexes are dominated by small clouds closer to the inner radius. In order to test this statement, we briefly examine mid-infrared interferometric observations.

Interferometric observations [e.g. Burtscher et al., 2013] provide sufficient angular resolution to (partially) resolve the dusty environment of AGNs. But still, even at the longest current baseline lengths (≈ 120m) it is not yet possible to resolve the mid-infrared emission at distances close to the sublimation radius. However it is possible to quantify the unresolved emission of the object. It is expected that objects with significant contribution from clouds at small distances have a large unresolved frac-

tion. Burtscher et al. [2013] determined the contribution of this unresolved emission (point source fraction) for a sample of objects and concluded that the point source fraction does not follow a clear trend with luminosity.

Since the subset of object taken from [Burtscher et al., 2013] do not form a complete sample, possible biases can appear when considering statistical distributions. To address the question of possible bias, the spectral index together with the $12\,\mu$m flux is plotted in Fig. 5.6. Although for this work only Type 1 and 1i objects are analyzed, Type 2 objects are included in the figures for comparisson. In Fig. 5.6 most of the objects have similar mid-infrared fluxes, except for the two brightness objects NGC1068 and Circinus. Although the subset of Type Is is small we can observe from Fig. 5.6 that the we have an almost similar number of objects at low and high values for the spectral index. Since no clear dependence is observed with respect to the $12\,\mu$m single-aperture flux, we assume that possible bias due to the flux-limited selection are not too strong.

Here we review the point source fraction and analyze to investigate possible explanations for the unresolved emission. Measures of resolution depend strongly on the source distance and intrinsic size which is in turn related to the source luminosity. To account for these effect we 'rescale' each source following the procedure described on LGJ15. We rescaled the object so that their $12\,\mu$m single-aperture flux matches a value of 1 Jy. This is achieved by artificially 'moving' the source further or closer to us. The baseline length of each measurement has to be multiplied by a factor of $\sqrt{F_{tot}}$, where F_{tot} is the single-aperture flux at $12\,\mu$m. To have the same maximum resolution for every object, only rescaled baselines with a length of less than 80 m are considered before calculating the point source fraction. For most of the objects the point source fraction computed using this rescaling is in agreement with the values of Burtscher et al. [2013], but for some objects such as Circinus or NGC1068 the point source fraction changes significantly.

In Fig. 5.7, the point source fraction as a function of the spectral index is shown for the objects from [Burtscher et al., 2013]. Type 2 objects are also included for comparisson. In general, there is a good agreement with the previous statement; unresolved objects are warmer than well resolved objects. The best linear fit obtained using the data of Type 1 and 1i objects is $f_{pt} = (0.48 \pm 0.02)\alpha + (1.27 \pm 0.026)$, where α is the single-aperture spectral index in the N-band. This relationship can in principle be used to determine future observing targets for the second-generation interferometric instrument MATISSE [Lopez et al., 2008] and get an approximation of the resolution needed to resolve the infrared emission.

A direct evidence that the spectral index is strongly related to the extension of the torus could come from information about the size of the resolved emission. An estimate for a single size that characterizes the nuclear light distribution of the mid-

infrared emission can be obtained from the interferometric half-light radius. This is the radius where the interferometric visibility drops to half of the value of the total emission. The corresponding values for the objects are taken from Burtscher et al. [2013]. The half-light radius in terms of the sublimation radius for the available objects is shown in Fig. 5.8 together with their respective spectral index. Type II objects are again included just for comparisson. While the trend is less clear than for the point source fraction, it is possible to observe that objects with the lowest extensions have spectral indexes greater than -1.3, while objects with an spectral index lower than -1.5 are clearly more extended.

While the dusty environment of AGNs could be quite complex it has been shown that the mid-infrared emission is strongly related to the average location of the clouds and that Type I objects have torus with multiple extensions, which cannot be explained by just an inclination effect as stated by the Unified Model of AGNs. In the classical image of the standard model, it is expected that the emission of Type I objects should be less extended than Type IIs; since the inner regions of the dusty structure are more exposed for Type Is than for Type IIs. This is true for some objects of our sample, but for some of the Type I objects the extension is significantly large even larger that for Type II objects.

5.5. Conclusions

In this work the clumpy environment of AGNs is analyzed by using spherical dusty clouds which are the basic blocks for building complex dusty torus models. The properties of spherical dusty clouds are studied with emphasis on the silicate feature and the spectral index. The analysis of the single clouds suggest that there should be a clear relation of the spectral index with the location of the clouds. This statement was later investigated using mid-infrared observations of AGNs. The conclusions from this work can be summarized as follows,

- The silicate feature in emission produced by a spherical cloud can be reduced by an inclination effect, increasing the optical depth of the cloud or by the sublimation of the silicate grains. Although the most efficient mechanism is achieved by changing the inclination.

- Increasing the optical depth of the clouds reduces the silicate feature due to a contrast effect. This effect is stronger for clouds at small distances and it is not an intrinsic property of clouds with graphites in the dust mixture.

- Sublimation effects are only relevant for clouds at distances lower than $5\,r_{sub}$, where r_{sub} is the sublimation radius of graphites with a size of $0.25\,\mu$m. The

sublimation of grains become less efficient for large optical depths ($\tau_{9.7} > 16.$), above this value neglecting the implementation of the sublimation is justified.

- The spectral index of AGNs is more related to the extension of the dusty torus than with the optical thickness. AGNs with bluer spectra are dominated by clouds close to the sublimation radius and are therefore less extended.

- Type I objects could have a broad range of extensions, going from compact objects or extended objects with dusty clouds at larger radii.

CHAPTER 6

The dormant mid-infrared environment of the Seyfert Type II NGC1068

N. López-Gonzaga, F. Bauer, K. R. W. Tristram, D. Asmus, A. Marinucci, L. Burtscher,
G. Matt, D. Stern, F. A. Harrison

Abstract

Recent *NuSTAR* observations (in 2015) revealed X-ray variability on the nucleus of NGC 1068. Using interferometry, we aim to detect possible variability changes in the mid-infrared environment as a possible response of the dusty torus to the observed X-ray changes. We make a direct comparison between similar (u, v) points observed before and during the X-ray variations. The average correlated fluxes and differential phases are compared to detect a possible change from the nuclear 2 pc emission. The correlated flux ratios and differential phase differences of measurements before and during the X-ray variation show no significant change over a period of 10 years with minor variations of at most 10 %. Our finding that the mid-infrared environment of NGC1068 has remained unchanged for the last 10 years and even after a recent transient change in the X-rays suggest that the X-ray variation seen by NuSTAR measurements is due to X-ray emission piercing through the dusty region.

6.1.   Introduction.

The galaxy NGC1068, at a distance of $\approx 14.4\,\mathrm{Mpc}$ is typically referred to as a prototype Seyfert II galaxy. It has been intensively studied for many years, providing broad support for the AGN unification theory [Antonucci, 1993; Urry & Padovani, 1995]. Optical polarization observations of this object revealed for the first time the broad-line emission in Type II AGNs and provided evidence for the existence of a circumnuclear dusty region, usually referred to as the 'torus' [Antonucci & Miller, 1985; Miller et al., 1991].

The central engine in AGNs produces X-ray/Optical/UV emission that is absorbed and re-emitted in the infrared at slightly larger scales by circumnuclear dust, giving rise to a pronounced peak in the spectral energy distribution of many AGNs [Sanders et al., 1989]. The mid-infrared environment of NGC 1068 shows high complexity and asymmetries at different scales. Early high spatial resolution adaptive optics studies revealed the existence of infrared extended emission, elongated in the north-south direction and unresolved in the east-west direction [Bock et al., 1998, 2000; Tomono et al., 2001; Galliano et al., 2005b]. The parsec-sized circumnuclear dust structure was first resolved by Jaffe et al. [2004] using mid-infrared ($\lambda = 8 - 13\,\mu\mathrm{m}$) interferometric observations from the MID-Infrared Interferometric Instrument [MIDI, Leinert et al., 2003] at the European Southern Observatory's (ESO) Very Large Telescope Interferometer (VLTI) located on Cerro Paranal in Chile. Subsequent work by Raban et al. [2009] and López-Gonzaga et al. [2014] reported additional MIDI observations with more extensive (u, v) coverage, which allowed them to investigate the structure of the inner regions of the obscuring disk with greater detail. According to the modeling done by López-Gonzaga et al. [2014], the mid-infrared environment can be decomposed in three distinct components: 1) a 1.35×0.45 parsec hot component ($\sim 800\,\mathrm{K}$) at a position angle (PA) of $-42\,°$, co-linear with the H_2O megamaser disk [Greenhill et al., 1996] and associated with the inner funnel of the obscuring disk [Raban et al., 2009]; 2) a $\sim 3 \times 2$ parsec warm nuclear component ($\sim 300\,\mathrm{K}$) considered an extension of the nuclear hot dust; 3) a $\sim 13 \times 4$ warm ($\sim 300\,\mathrm{K}$) extended component located ~ 7 parsec north of the hotter nuclear disk. This extended component emits about $40\,\%$ and $60\,\%$ of the total flux at $8.5\,\mu\mathrm{m}$ and $12\,\mu\mathrm{m}$ respectively.

In the X-ray regime, the emission is also quite complex. NGC1068 has been extensively studied at X-ray wavelengths over the past two decades [see e.g. Guainazzi et al., 1999; Matt et al., 1997; Wang et al., 2012; Bauer et al., 2015] and is considered the best case of a heavily Compton-thick AGN [$N_H > 10^{25}\,\mathrm{cm}^{-2}$, Matt et al., 2000]. Using *NuSTAR* [Harrison et al., 2013] observations, with unprecedented sensitivity above $\sim 8\,\mathrm{keV}$ and a full energy range of $3 - 79\,\mathrm{keV}$, and previous X-ray data, Bauer et al. [2015] found that the observed X-ray emission of NGC1068 was consistent with
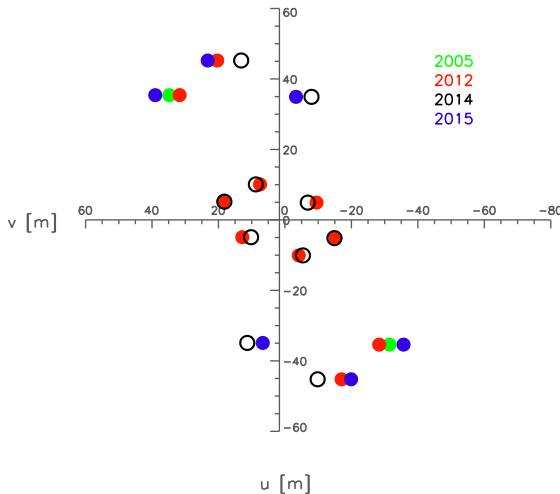
Figure 6.1: *(u, v) coordinates of the data points observed in 2015. Data points with similar (u, v) coordinates as the 2015 data obtained at different time periods where collected from the archive and are shown with different colors.*

being constant over all past observations at $<10\,\mathrm{keV}$ (with less than $\sim 10\,\%$ variance) and $>10\,\mathrm{keV}$ (with less than $\sim 30\,\%$ variance). The best fit model for the combined *NuSTAR*, *Chandra*, *XMM-Newton*, and *Swift* BAT spectra spanning a decade in time is a multi-component reflector of: 1) a $\approx 10^{25}\,\mathrm{cm}^{-2}$ nuclear ($< 2\,\mathrm{arcsec}$) cold reflector consistent with torus reflection; 2) a $\approx 10^{23}\,\mathrm{cm}^{-2}$ nuclear cold reflector possibly from tenuous material in the vicinity of photoionized clouds; and 3) a $\approx 5 \times 10^{24}\,\mathrm{cm}^{-2}$ host galaxy ($> 2\,\mathrm{arcsec}$) cold reflector consistent with distant reflection from large scale clouds.

6.1.1. X-ray variability

More recently, Marinucci et al. [2016] presented results from a monitoring campaign from 2014/2015 using *NuSTAR* and *XMM-Newton* observations to look for possible variability in the reflection component (Fe Kα 6.4 keV line and ~ 30 keV Compton hump). The strength of Fe Kα line, measured with the *XMM-Newton* data, was found to be constant to within statistical errors. However, *NuSTAR* observations show a transient excess of $32 \pm 6\,\%$ above 20 keV.

The variability is somewhat unexpected, given the model provided by Bauer et al. [2015] and previous variability constraints. According to [Marinucci et al., 2016], the most plausible explanation is a decrease on the total absorbing column of at least $\Delta \mathrm{N}_H \simeq 2.5 \times 10^{24}\,\mathrm{cm}^{-2}$, which permitted the nuclear radiation to pierce through the patchy nature of the torus clouds. Variations lasting for a $\sim$tens of days, such as the one observed for NGC1068, suggest that the X-ray absorbing clouds detected are likely dusty [Markowitz et al., 2014] and therefore we could look for any response in the infrared that may reveal more about this sudden changes. For an absorption

variability effect we would not expect to observe an increase in the mid-infrared flux, as the $>10\,\mathrm{keV}$ change is due to shifting clumps of Compton-thick material, contrary to a luminosity increase scenario where we would expect to see an increase of the infrared flux or a change in the structure of the dusty region.

A response of the torus to any variability coming from the accretion disk should first be seen in the most compact component and should be evident. Because variations in the hot component could be washed out by the dominating flux of the larger mid-infrared components, we focus our attention on interferometric observations to prove a variability change. Thanks to the high resolution mid-infrared observations with MIDI, especially at intermediate baseline lengths $(30-40\,\mathrm{m})$ where the infrared emission from sub-parsec structures is marginally resolved and the large scale emission of a few parsecs size is over-resolved. In this paper we present new mid-infrared interferometric observations of NGC1068 and investigate possible variations in the mid-infrared in order to interpret the observed X-ray variations. The outline of the paper is as follows, Sect. 6.2 describes the interferometric observations, data reduction and calibration. The reduced data is analyzed and discussed in Sect. 6.3. And finally, our conclusions are presented in Sect. 6.4.

6.2.   Mid-infrared interferometric observations

Interferometric measurements were obtained with the instrument MIDI at the ESO's VLTI. The MIDI instrument is a two beam Michelson interferometer that operates in the N band (8 to $13\,\mu$m) and combines the light from two telescopes; a pair of 8.2 meter Unit Telescopes (UTs) or a pair of 1.8 meter Auxiliary Telescopes (ATs). The main interferometric observables obtained by MIDI are the correlated flux spectra and the differential phases[1], which are obtained from the interference pattern generated by the two beams. For our observations we used the low resolution NaCl prism with spectral resolution $R \equiv \lambda/\Delta\lambda \sim 30$ to disperse the light of the beams.

Observations with intermediate AT baselines were requested and observed during the nights of January, 10, 20, and 23, 2015 using Director's Discretionary Time (DDT). We additionally include published data and unpublished observations from our previous campaigns that include observations taken with similar (u, v) points observed contemporaneously with the period of X-ray variation and as well as years before. The unpublished measurements were carried out on the nights of September, 21, 26, and 30, 2014, and November, 17, 2014, using Guaranteed Time Observations

---

[1]In the remainder of this paper we use *correlated* fluxes rather than *visibilities*, which are defined as the correlated flux divided by the total or *photometric* flux. In the mid-infrared, the difficulties of measuring photometric fluxes against the fluctuations of the bright sky favor the use of correlated fluxes. The differential phases are identical to the *true* interferometric phases except that the constant and linear dependencies of phase on wavenumber $k \equiv 2\pi/\lambda$ have been removed.

NIGHT	BASELINE INFORMATION					CORRELATED FLUX						DIFFERENTIAL PHASE	
	Name	BL [m]	P.A. [°]	u [m]	v [m]	Average values [Jy] $F_{8.5\mu m}$	$F_{10.5\mu m}$	$F_{12\mu m}$	Epoch ratios $8.5\mu m$	$10.5\mu m$	$12\mu m$	Amplitude [°]	Epoch difference [°]
2012-09-24	B2C1	10.5	28.3	-5.0	-9.2	4.2 ± 0.4	5.5 ± 0.3	9.8 ± 0.6	1.0 ± 0.1	1.0 ± 0.1	1.0 ± 0.1	46.0 ± 9.5	8.0 ± 15.6
2014-09-26	"	11.1	33.3	-6.1	-9.2	4.4 ± 0.2	5.6 ± 0.3	10.1 ± 0.6				53.9 ± 6.1	
2005-11-13	U2U3	43.3	40.9	28.4	32.5	3.6 ± 0.5	1.6 ± 0.2	4.0 ± 0.3	1.2 ± 0.1	0.9 ± 0.1	1.0 ± 0.1	-42.9 ± 6.8	7.5 ± 11.7
2012-09-20	G1I1	41.4	38.4	25.7	32.5	3.4 ± 0.2	1.5 ± 0.1	3.9 ± 0.2				-59.2 ± 10.7	
2015-01-10	"	45.6	44.6	32.0	32.5	3.5 ± 0.2	1.4 ± 0.1	4.8 ± 0.2				-43.5 ± 5.5	
2007-10-07	E0G0	15.2	71.8	14.4	4.7	7.1 ± 0.9	6.5 ± 0.6	11.3 ± 1.1	0.9 ± 0.2	0.9 ± 0.1	1.0 ± 0.2	-4.5 ± 7.8	1.7 ± 13.9
2014-09-26	A1C1	15.0	71.5	14.2	4.7	7.1 ± 0.7	6.2 ± 0.5	10.3 ± 1.0				-2.9 ± 6.1	
2012-09-19	I1K0	44.5	21.1	-16.0	-41.5	2.5 ± 0.3	0.9 ± 0.1	3.2 ± 0.1	1.0 ± 0.1	1.2 ± 0.2	1.0 ± 0.2	23.1 ± 19.7	5.7 ± 24.6
2014-11-17	"	42.6	13.4	-11.1	-41.5	2.7 ± 0.5	1.1 ± 0.1	3.2 ± 0.5				27.7 ± 10.7	
2015-01-23	"	45.4	24.0	-18.5	-41.5	2.9 ± 0.1	1.0 ± 0.1	3.6 ± 0.1				9.9 ± 3.3	
2012-09-26	A1B2	10.0	116.9	-8.9	4.5	5.2 ± 1.1	3.1 ± 0.6	7.3 ± 0.9	1.0 ± 0.2	1.1 ± 0.3	0.8 ± 0.3	-14.8 ± 8.7	5.4 ± 16.7
2014-09-26	"	8.6	121.7	-7.3	4.5	4.4 ± 0.4	3.3 ± 0.3	7.5 ± 0.4				-9.5 ± 8.0	
2014-09-30	H0I1	33.1	165.5	8.3	-32.0	3.4 ± 0.4	1.8 ± 0.1	5.3 ± 0.3	1.0 ± 0.1	1.0 ± 0.1	1.0 ± 0.1	30.1 ± 6.6	2.3 ± 9.3
2015-01-20	"	32.2	176.0	2.2	-32.0	3.8 ± 0.4	1.7 ± 0.1	5.4 ± 0.4				27.8 ± 2.7	

Table 6.1: *Averaged observed interferometric quantities for different baseline configurations. Name: Baseline configuration, BL: Projected baseline length, P.A.: Position angle, u,v : (u,v) coordinates.*

(GTO). A log of the observations and instrument setup can be found in Appendix A. The published data was taken from López-Gonzaga et al. [2014].

6.2.1. Data reduction and Calibration

As calibrators, either HD10380 and HD18322 were observed close in airmass to the target with $\Delta(\sec z) \leq 0.3$. We have applied the techniques developed during the MIDI AGN Large Program [Burtscher et al., 2012] to plan our observing strategy, data reduction process, and analysis of the data. Single-aperture observations and fringe searches were avoided to save time.

The reduction of the data was performed with the interferometric data reduction software *MIDI Interactive Analysis and Expert Work Station* [MIA+EWS[2], Jaffe, 2004] which implement the method of coherent integration for MIDI data. Calibration of the correlated fluxes was computed by dividing the correlated fluxes of the target by those of the calibrator and multiplying by the known flux of the calibrator. For HD10380 and HD18322 we used the spectral template of Cohen et al. [1999]. Following the stacking strategy of Burtscher et al. [2013], fringe tracks on NGC1068 were reduced together when they were less than 30 min apart and were calibrated with the same star

6.3. Results

In total, 19 independent (u, v) points measured under good weather conditions were reduced and calibrated, plus 17 independent (u, v) points with similar (u, v) coordinates to the new data were included from the previous published data presented by López-Gonzaga et al. [2014]. In order to obtain estimates of the correlated fluxes and differential phases with good signal-to-noise ratio, we followed the approach of López-Gonzaga et al. [2014] where we binned the individual (u, v) points if they were within $2\,\mathrm{m}$ in distance for short baseline lengths $(5-15\,\mathrm{m})$ and within $8\,\mathrm{m}^3$ for intermediate baselines $(30-40\,\mathrm{m})$. We divided all our binned measurements into 6 groups with similar (u, v) coordinates. Fig. 6.1 shows the (u, v) coordinates of the grouped data points for different epochs while our average estimates are summarized in Table 6.1. The table includes the baseline information for each group and year,

---

[2]EWS is available for download from:
http://home.strw.leidenuniv.nl/~jaffe/ews/index.html.

[3]For intermediate baselines $(30-40\,\mathrm{m})$ we extend the range up to $8\,\mathrm{m}$ due to the limited amount of observations, this binning is still justified as most of the emission observed with such resolutions comes from the hot compact component (with size $20 \times 6\,\mathrm{mas}$) which is unresolved or marginally resolved at intermediate baselines. Previous $30-40\,\mathrm{m}$ UT data showed that (u, v) points within 8m apart in distance measure always the same spectra within the computed uncertainties López-Gonzaga et al. [2014]
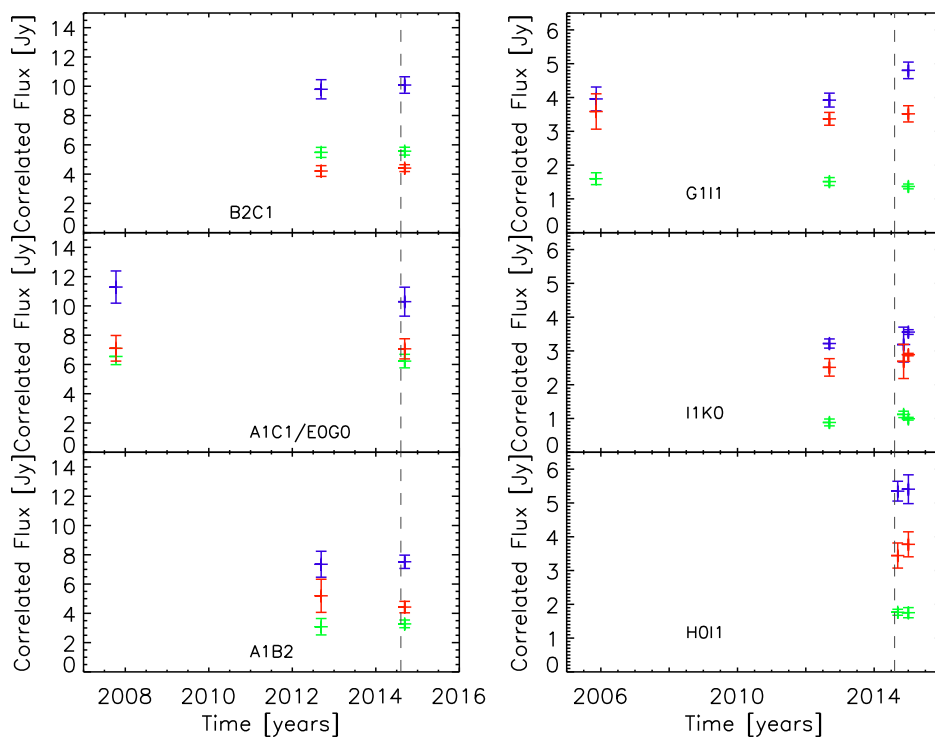
Figure 6.2: *Average correlated fluxes for different epochs grouped by their baseline configuration. The points on each frame have similar (u, v) coordinates. The color of the symbols indicate the wavelength: Fluxes at $12\,\mu$m are in blue, $10.5\,\mu$m are in green and $8.5\,\mu$m are in red. The dashed line marks the time of the reported X-ray variations.*
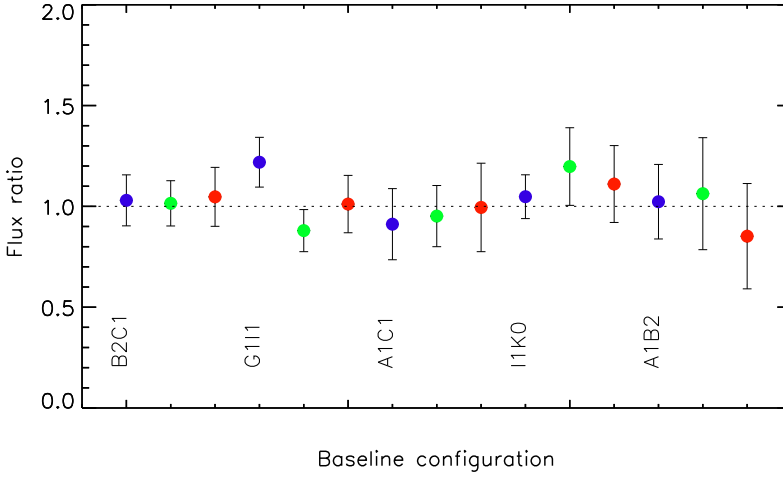
Figure 6.3: *Correlated flux ratios between average measurements from before and during the X-ray variations for each baseline and wavelength. The color of the symbols are the same as in Fig. 6.2. The dotted line indicates a ratio equal to one, i.e. no variation.*

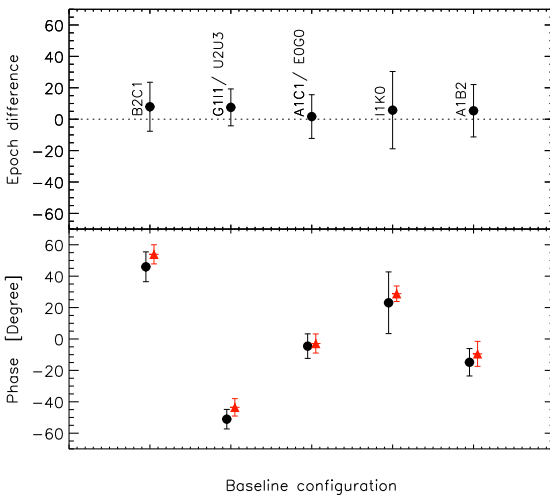**Figure 6.4:** *Variations in the amplitude of the differential phase. Top) Differential phase difference between average measurements from before and after the X-ray variation for each baseline configuration. The dotted line indicates a ratio equal to one. Bottom) Amplitude of the differential phase before (black circles) and after (red triangles) the X-ray variation for each baseline.*

the average correlated flux at 8.5, 10.5, and $12.0\,\mu m$ and the mean amplitude of the differential phase. Fig. 6.2 shows the average correlated fluxes for each group as a function of time.

Due to the limited amount of interferometric data we cannot model our measurements with complex models or even with Gaussian distributions unless we take many assumptions. Instead, we perform a direct comparison of the observed quantities on each baseline. For each baseline and observed quantity ($F_{8\mu m}$, $F_{10.5\mu m}$, $F_{12\mu m}$, and $\Delta\phi$), we compute two distinct average quantities, one using measurements before the reported increase on the X-rays (before September 2014) and the second one including observations after the increased X-rays (contemporaneous or after September 2014). We then compute the ratios of the quantities for the two epochs of each baseline with their respective uncertainties using propagation of errors. The only (u, v) coordinate where we cannot make a comparison between the two epochs is for the baseline H0I1, since we only have measurements after the variation in X-rays. In Figure 6.3 we show the ratios for the correlated fluxes for each baseline at different wavelengths. Additionally, we show in Fig. 6.4 the average amplitude of the differential phases, as well as their respective ratios between the two epochs.

The correlated fluxes show consistent behavior with no change during both periods. If we assume no changes from the bigger components of the nuclear dust of NGC 1068, then possible changes in flux should be detected by all the baselines reported in this work. We also do not expect to detect a change in the size of the hot component since this component is mostly unresolved with the baselines used for this work. By taking the mean and the standard deviation from all the flux ratios we obtain an average value for the flux ratio of 1.03 ± 0.06, 1.02 ± 0.07 and 0.96 ± 0.08 for 8.5, 10.5 and $12.0\,\mu m$, respectively. So possible variations could be at most of 8% of the total flux, which is still consistent with was measured before by López-Gonzaga et al. [2014] for the period where NGC 1068 did not exhibit a change in X-rays. The differential phases are also consistent with no change over the full measurement period. The total change in the phases for the two different periods is about $5.6 \pm 7.4\,^\circ$. The similar differential phases measured during different periods not only support the existence of the phases, but it also shows that no clear changes have occurred in the last 10 years.

The constant behavior in the infrared emission of the nuclear region of NGC 1068 suggest that the observed change in the X-ray regime is unlikely to be due to an intrinsic change in the luminosity of the central accretion disc. Due to the shutdown of the instrument MIDI, the nuclear emission of NGC 1068 cannot be further monitored to monitor. But further variations of the nuclear mid-infrared emission should be detected in the future with the second-generation instrument MATISSE[Lopez et al., 2008]. With no significant change in the mid-infrared emission, it is more likely that

the increase in X-ray flux could be explained as escaping emission through the patchy nature of the torus clouds or that the X-ray increase is not related to any variation in the thermal emission of the accretion disc.

6.4.   Conclusions

Mid-infrared interferometric observations were obtained and analyzed in order to investigate possible variations in the infrared emission of the nuclear dusty region of NGC 1068. Based on the analysis of the correlated fluxes and the differential phases we can conclude that the nuclear mid-infrared environment of NGC 1068 has remained unchanged for a period of almost 10 years, with variations in the flux of at most 8 %, even when variability changes in the X-ray regime were observed. Our results support the idea of Marinucci et al. [2016], that it is most likely that the observed flux increase in the X-rays is due to the clumpy nature of the dusty region where the X-ray emission has managed to pierce through. It might also possible that the origin of the X-ray variation may not be related to the accretion process, although the strength of the X-ray variation, in terms of X-ray luminosity seems impossible to explain by any process other than the AGN.

6.5.   Appendix

6.5.1.   Log of observations

Time	St	BL [m]	PA [°]	Air	OK?	Gframes	ctime	Δ am
2012-09-20: I1K0								
08:42:47	1	44	20	1.2	1	6402	08:50:09	0.1
09:03:58	0	44	22	1.2	1	5918	08:50:09	0.1
09:07:27	1	44	22	1.2	1	5075	09:18:18	0.1
09:11:03	0	44	22	1.2	1	5690	09:18:18	0.1
2014-09-26: B2C1								
05:11:03	0	9	14	1.2	1	6094	05:16:05	0.1
05:23:14	1	9	16	1.2	1	11442	05:29:53	0.1
05:35:11	0	9	18	1.2	1	11472	05:29:53	0.0
2014-09-26: A1C1								
06:06:26	1	14	71	1.1	1	11459	06:13:05	0.1
06:18:14	0	15	71	1.1	1	11505	06:13:05	0.0
2014-09-26: B2C1								
08:17:43	1	11	33	1.2	1	7438	08:24:04	0.1
08:29:31	0	11	33	1.2	1	11525	08:24:04	0.1
2014-09-26: A1B2								
08:56:40	0	9	119	1.3	1	11385	08:51:02	0.1
09:08:35	0	8	120	1.3	1	11332	09:03:05	0.1
09:37:40	0	7	124	1.4	1	5684	09:25:12	0.2
2014-09-30: H0I1								
09:03:30	0	33	165	1.3	1	7335	08:55:52	0.2
09:07:37	1	33	165	1.4	1	11267	09:15:35	0.1
09:24:03	0	32	168	1.4	1	14392	09:15:35	0.2
09:44:28	0	32	172	1.5	0	1678	09:37:27	0.2
2014-11-17: I1K0								
03:28:04	0	42	12	1.1	1	6623	03:19:57	0.1
03:31:52	0	42	12	1.1	1	6723	03:40:02	0.1
03:54:32	1	42	15	1.1	1	6855	04:06:28	0.1
03:58:21	1	43	15	1.1	1	5963	04:06:28	0.1
04:14:09	0	43	17	1.1	1	3817	04:06:28	0.1
2015-01-10: G1I1								
02:00:53	0	46	45	1.3	0	-1	01:45:36	0.1
02:11:32	0	46	45	1.3	1	11255	02:20:01	0.1
03:22:15	1	44	43	1.7	1	11406	03:34:07	0.2
03:49:18	0	43	41	2.0	1	9336	03:34:07	0.4
2015-01-11: G1I1								
02:22:06	0	46	45	1.4	0	2484	02:05:42	0.2
2015-01-20: D0H0								
00:56:01	0	62	72	1.2	0	-1	01:40:14	0.0
2015-01-20: H0I1								
02:22:37	0	32	172	1.5	1	9407	02:05:21	0.3
02:59:54	0	32	179	1.9	1	9872	02:41:20	0.4
2015-01-23: G1I1								
00:36:39	0	46	45	1.2	0	-	-	-
00:53:51	0	46	45	1.2	0	-	-	-
2015-01-23: I1K0								
01:24:31	0	45	24	1.3	1	11348	01:15:33	0.2

Table 6.2: *Log of observations: NGC1068. The columns are: Time of fringe track observation; St Stacked with the following observation (yes:1, no:0); BL projected baseline length; PA position angle; Air Airmass of fringe track; OK? Goodness of observation (good:1, bad:0); Gframes Number of good frames; Ctime Time of the calibrator fringe track observation; Δ am Difference in airmass with calibrator.*

SUMMARY

In this thesis, I have studied the nuclear environment of active galaxies by examining the structure of the dusty material that acts as an obscuring entity and coexists with the gas that might be responsible for injecting the fuel into the Super Massive Black Hole's accretion disc. By analyzing high angular resolution infrared observations, we have determined the dust geometry, composition and temperature profile. We first focused on the prototypical Seyfert type 2 galaxy, NGC 1068. We used mid-infrared (MIR) interferometric observations to reveal the large scale $(5-10\,\mathrm{pc})$ geometry of the nuclear dusty environment with the aim of finding a connection between the inner hot disc [Jaffe et al., 2004; Raban et al., 2009] and the surrounding environment. Since current MIR interferometric observations do not include true phase information, we analyzed and modeled the chromatic phases measured by the instrument MIDI together with the correlated fluxes and recovered a model image of the nuclear infrared region. We found that the infrared emission is highly asymmetric and that about $60-70\,\%$ of the emission at $12\,\mu\mathrm{m}$ originates from a large diffuse component located close to the walls of the ionization cone. Unlike the previous idea that most of the emission had to come from a disc-like structure tracing the classical dusty torus, the largest fraction of the nuclear infrared emission of NGC 1068 does not contribute to the equatorial emission.

Due to its proximity, NGC 1068 has been the focus of many studies. While considered a prototypical Seyfert galaxy, the nuclear environment of this active galactic nucleus (AGN) shows some peculiarities: a central hot disc unaligned with the jet axis, the high asymmetry in the MIR environment, and a bending jet at large scales. This object is a great laboratory to investigate the physical mechanisms present in the cores of AGNs. As an example, shocks observed along the narrow line region (NLR) of NGC 1068 should be investigated to determine their relevance as a heating mechanism.

The peculiarities observed in NGC 1068 could be associated with intrinsic properties of individual objects. However some general properties might be shared between AGNs of the same type. In order to learn more about the morphology of the dusty region, we performed an analysis of a set of local galaxies to trace the dominant direction of the infrared emission. Due to the inhomogeneous mapping of the interferometric measurements we were only able to identify elongated shapes in five

Seyfert objects and in all elongated objects the major axis of the emission is closer to the polar axis than the equatorial axis. An improvement of the (u, v) coverage will double the number of detections and increase the significance of our statistics. By finding only polar elongations in our AGN sample it is reasonable to assume that this characteristic is a common feature present in Seyfert galaxies. It is worth noting that, although the elongation is closer to the polar axis, the sample shows offsets of $20-30°$ with respect to the polar axis. This could be interpreted as asymmetric emission similar to the one present in the core of NGC 1068 and Circinus [Tristram et al., 2014], probably caused by an inhomogeneous distribution of the dusty clouds.

7.1.   Disk vs winds

As discussed in Chapter 2 and 3, the dominant infrared emission of the observed Seyfert objects seems to have a preferential direction towards the polar axis. Many infrared studies, involving spectral information only, typically ignore this polar emission. Studies of MIR interferometric observations suggest that the dusty emission is composed by a disc-like structure and a dominant extended polar emission. Such morphologies are observed with great detail in the nucleus of NGC 1068 (see Chapter 2) and the Circinus galaxy [Tristram et al., 2014]. Two current explanations for polar emission are the following: 1) the dust is located along the ionization wall of a geometrically thick extended torus-like structure, and 2) the origin of the polar emission is due to a dusty wind surrounding the narrow line region. Both explanations seem to attribute the emission to dust around the ionization cone.

Most probably, MIR observations alone cannot differentiate between both scenarios. Therefore, if we want to solve the puzzle of the polar emission an effort to combine multiple observational techniques and multi-wavelength information should be carried out. Kinematic information of the nuclear region is also required to analyze the velocity profiles of the gas at the inner parsecs. A detailed analysis of line emission at sub-arcsecond scales will help to distinguish between a wind, a torus-like structure or a combination of both. Additional observations from sub-millimeter wavelengths providing information about the cold dust can set constrains on the extension of the torus. Mid-infrared sizes indicate that the emission of the warm dust must originate at most at a few tens of the sublimation radius. Recent sub-millimeter observations of NGC 1068 [García-Burillo et al., 2014] and Circinus [Hagiwara et al., 2013] using ALMA arrays revealed a relatively low amount of cold emission, with almost no indication of extended emission, suggesting again a compact size for the dusty region. The compact size along the equatorial direction would seem to favor the wind-like emission, as a geometrical extended torus would produce cold emission that would be detectable at ALMA bands. This should be carefully examined by

future observations and proper modeling.

7.2. The standard AGN model in the era of high-resolution infrared observations

Two of the main questions of this thesis are: 1) what is the morphology of the dusty region, and 2) how similar or different are AGNs. To try to answer this, we have statistically analyzed a set of Seyfert galaxies to test the validity of the standard model of AGNs. In many studies, the spectral energy distribution (SED) of individual galaxies is fitted with theoretical SEDs, obtained from clumpy torus models, to extract physical properties of the clumpy torus. Unfortunately, the models used for this task are quite degenerate and fitting only the SEDs cannot completely determine the structure of the torus. Therefore, we have investigated the similarities of Seyfert galaxies in Chapter 4 by combining infrared interferometric observations with radiative transfer clumpy models. Because of current limitations of infrared interferometric measurements, we use a probabilistic approach rather than a direct fit of each object. This method ignores the alignment of the emission with the polar axis, but it does include significant geometrical information (for example, sizes and shapes). We show that subsets of type 1 and type 2 objects are better described with models having different properties, with the main difference being the volume fraction that the dust occupies. A line of sight effect or multiple random realizations of clouds are not able to explain all the observed differences between both types.

The existence of intrinsically different type 1 objects is also supported by the correlation of the observed mid-infrared temperature with the location of the clouds (see Chapter 5). The results described in Chapter 4 are consistent with the idea that type 2 objects have a larger covering fraction and might therefore be preferentially drawn when selected in the mid-infrared [Elitzur, 2012].

This is a first step into statistical studies that makes use of the highest angular resolution MIR data available up to now. The approach we took is not unique and many assumptions still need to be improved, but it does provide a first step for combining single-aperture and interferometric data that are relevant for finding an explanation to the observed MIR emission in AGNs.

To confirm the existence of intrinsically different type 1 objects and to obtain more information about the dusty region of AGNs, the number of objects observed with interferometry should be increase at least by a factor of two. Studies with future interferometric instruments should aim to collect multi-wavelength visibilities of a large set of objects and with different resolutions.

7.3. Dusty torus models

Simple geometrical models are useful to give a general representation of the infrared emission of AGNs but the complexity of the dusty environment requires a more detailed and more physically based model to explain the different observed features. An important challenge for radiative transfer continuous or clumpy models is to reproduce the observed features presented and discussed in this thesis, such as the polar elongated emission at parsec scales, the lower filling factors of dust and the diverse locations of the bulk emission in the mid-infrared.

Recent hydrodynamical AGN models are already going in this direction. Hydrodynamical models already provide a first approximation to the polar elongation [Schartmann et al., 2014]. Therefore the next step is to make a proper match between high resolution images and model images directly obtained from hydrodynamical simulations or models using more realistic physical constrains.

The future study of the dusty nuclear emission of AGN must be investigated from three different sides. Firstly, near- and mid-infrared interferometric observations with adequate mappings will allow astronomers to obtain a better image of the shape and morphology of the dusty environment. Secondly, obtaining multi wavelength polarimetric information will keep revealing information obtained from indirect light otherwise not observed due to obscuration. Combining polarimetric information with high resolution images will provide more insight on the structure of the dusty environment. Thirdly, models need to be modified to explain the polar emission observed with interferometry. Current knowledge obtained with the classical torus models (clumpy or continuous) should be tested to verify their validity.

The number of objects where we are currently able to disentangle the structure of the dusty region is relatively low. The future of infrared observations of the dusty region of AGN will have a progress with the arrival of new instruments. The second generation of instruments for the Very Large Telescope Interferometer (VLTI), GRAVITY in the near-infrared and MATISSE in the mid-infrared will provide the necessary tools to investigate the hot and warm dust by providing high resolution images in the K, L, M and N band. In addition, the Atacama Large Millimeter Array (ALMA) will provide information about molecular lines and the amount of cold dust in AGNs. In the later future, telescopes such as the James Webb Space Telescope and the E-ELT will add further contribution to the field, providing infrared spectra with unprecedented sensitivity and resolution and the opportunity to observe in the Q-band with the instrument METIS. Although the field of AGNs will have a boost once the second generation of infrared interferometric instruments come online, the major step will be reached once we have an ALMA-like facility operating in the infrared regime.

Bibliography

A. Alonso-Herrero, L. Colina, C. Packham, et al., 2006. *ApJ*, 652:L83–L87.

A. Alonso-Herrero, C. Ramos Almeida, R. Mason, et al., 2011. *ApJ*, 736:82.

R. Antonucci, 1993. *ARA&A*, 31:473–521.

R. R. J. Antonucci, 1984. *ApJ*, 278:499–520.

R. R. J. Antonucci & J. S. Miller, 1985. *ApJ*, 297:621–632.

D. Asmus, P. Gandhi, S. F. Hönig, et al., 2015. *MNRAS*, 454:766–803.

D. Asmus, P. Gandhi, A. Smette, et al., 2011. *A&A*, 536:A36.

D. Asmus, S. F. Hönig, P. Gandhi, et al., 2014. *MNRAS*, 439:1648–1679.

R. Barvainis, 1987. *ApJ*, 320:537–544.

F. E. Bauer, P. Arévalo, D. J. Walton, et al., 2015. *ApJ*, 812:116.

T. Beckert, T. Driebe, S. F. Hönig, et al., 2008. *A&A*, 486:L17–L20.

J. J. Bock, K. A. Marsh, M. E. Ressler, et al., 1998. *ApJ*, 504:L5.

J. J. Bock, G. Neugebauer, K. Matthews, et al., 2000. *AJ*, 120:2904–2919.

C. F. Bohren & D. R. Huffman, 1983. *Absorption and scattering of light by small particles.*

M. A. Bransford, P. N. Appleton, C. A. Heisler, et al., 1998. *ApJ*, 497:133–162.

C. L. Buchanan, J. F. Gallimore, C. P. O'Dea, et al., 2006. *AJ*, 132:401–419.

G. R. Burbidge, 1961. *Nature*, 190:1053–1056.

L. Burtscher, W. Jaffe, D. Raban, et al., 2009. *ApJ*, 705:L53–L57.

L. Burtscher, K. Meisenheimer, W. Jaffe, et al., 2010. *PASA*, 27:490–495.

L. Burtscher, K. Meisenheimer, K. R. W. Tristram, et al., 2013. *A&A*, 558:A149.

L. Burtscher, G. Orban de Xivry, R. I. Davies, et al., 2015. *A&A*, 578:A47.

L. Burtscher, K. R. W. Tristram, W. J. Jaffe, et al., 2012. In *Society of Photo-Optical Instrumentation Engineers (SPIE) Conference Series*, volume 8445 of *Society of Photo-Optical Instrumentation Engineers (SPIE) Conference Series*.

M. Cohen, R. G. Walker, B. Carter, et al., 1999. *AJ*, 117:1864–1889.

R. I. Davies, L. Burtscher, D. Rosario, et al., 2015. *ApJ*, 806:127.

P. Deroo, H. van Winckel, T. Verhoelst, et al., 2007. *A&A*, 467:1093–1101.

A. Dorodnitsyn, G. S. Bisnovatyi-Kogan, & T. Kallman, 2011. *ApJ*, 741:29.

A. Dorodnitsyn, T. Kallman, & D. Proga, 2015. *ArXiv e-prints*.

C. P. Dullemond & I. M. van Bemmel, 2005. *A&A*, 436:47–56.

F. Eisenhauer, G. Perrin, W. Brandner, et al., 2011. *The Messenger*, 143:16–24.

M. Elitzur, 2012. *ApJ*, 747:L33.

M. Elmouttie, R. F. Haynes, K. L. Jones, et al., 1998. *MNRAS*, 297:1202–1218.

M. Elvis, B. J. Wilkes, J. C. McDowell, et al., 1994. *ApJS*, 95:1–68.

I. N. Evans, H. C. Ford, A. L. Kinney, et al., 1991. *ApJ*, 369:L27–L30.

E. A. Fath, 1909. *Lick Observatory Bulletin*, 5:71–77.

A. Feltre, E. Hatziminaoglou, J. Fritz, et al., 2012. *MNRAS*, 426:120–127.

T. C. Fischer, D. M. Crenshaw, S. B. Kraemer, et al., 2013. *ApJS*, 209:1.

S. C. Gallagher, M. M. Abado, J. E. Everett, et al., 2013. *ArXiv e-prints*.

E. Galliano, D. Alloin, E. Pantin, et al., 2005a. *A&A*, 438:803–820.

E. Galliano, E. Pantin, D. Alloin, et al., 2005b. *MNRAS*, 363:L1–L5.

J. F. Gallimore, S. A. Baum, & C. P. O'Dea, 1996. *ApJ*, 464:198.

J. F. Gallimore, S. A. Baum, & C. P. O'Dea, 2004. *ApJ*, 613:794–810.

P. Gandhi, H. Horst, A. Smette, et al., 2009. *A&A*, 502:457–472.

S. García-Burillo, F. Combes, A. Usero, et al., 2014. *A&A*, 567:A125.

I. Georgantopoulos & A. Akylas, 2010. *A&A*, 509:A38.

I. S. Glass, 1997. *Ap&SS*, 248:191–198.

G. L. Granato & L. Danese, 1994. *MNRAS*, 268:235.

D. Gratadour, Y. Clénet, D. Rouan, et al., 2003. *A&A*, 411:335–342.

D. Gratadour, D. Rouan, L. M. Mugnier, et al., 2006. *A&A*, 446:813–825.

L. J. Greenhill, C. R. Gwinn, R. Antonucci, et al., 1996. *ApJ*, 472:L21.

M. Guainazzi, G. Matt, L. A. Antonelli, et al., 1999. *MNRAS*, 310:10–20.

M. Haas, R. Siebenmorgen, E. Pantin, et al., 2007. *A&A*, 473:369–376.

Y. Hagiwara, M. Miyoshi, A. Doi, et al., 2013. *ApJ*, 768:L38.

F. A. Harrison, W. W. Craig, F. E. Christensen, et al., 2013. *ApJ*, 770:103.

L. G. Henyey & J. L. Greenstein, 1941. *ApJ*, 93:70–83.

A. Hernán-Caballero, A. Alonso-Herrero, E. Hatziminaoglou, et al., 2015. *ApJ*, 803:109.

L. Hernández-García, O. González-Martín, I. Márquez, et al., 2013. *A&A*, 556:A47.

F. Heymann & R. Siebenmorgen, 2012. *ApJ*, 751:27.

S. F. Hoenig, 2013. *ArXiv e-prints*.

S. F. Hönig, T. Beckert, K. Ohnaka, et al., 2006. *A&A*, 452:459–471.

S. F. Hönig & M. Kishimoto, 2010. *A&A*, 523:A27.

S. F. Hönig, M. Kishimoto, R. Antonucci, et al., 2012. *ApJ*, 755:149.

S. F. Hönig, M. Kishimoto, P. Gandhi, et al., 2010. *A&A*, 515:A23.

S. F. Hönig, M. Kishimoto, K. R. W. Tristram, et al., 2013. *ApJ*, 771:87.

H. Horst, W. J. Duschl, P. Gandhi, et al., 2009. *A&A*, 495:137–146.

H. Horst, P. Gandhi, A. Smette, et al., 2008. *A&A*, 479:389–396.

H. Horst, A. Smette, P. Gandhi, et al., 2006. *A&A*, 457:L17–L20.

K. Ichikawa, C. Packham, C. Ramos Almeida, et al., 2015. *ApJ*, 803:57.

K. Ichikawa, Y. Ueda, Y. Terashima, et al., 2012. *ApJ*, 754:45.

W. Jaffe, K. Meisenheimer, H. J. A. Röttgering, et al., 2004. *Nature*, 429:47–49.

W. J. Jaffe, 2004. In *Society of Photo-Optical Instrumentation Engineers (SPIE) Conference Series*, editor W. A. Traub, volume 5491 of *Society of Photo-Optical Instrumentation Engineers (SPIE) Conference Series*, page 715.

K. G. Jansky, 1933. *Nature*, 132:66.

F. Kemper, W. J. Vriend, & A. G. G. M. Tielens, 2004. *ApJ*, 609:826–837.

A. L. Kinney, H. R. Schmitt, C. J. Clarke, et al., 2000. *ApJ*, 537:152–177.

M. Kishimoto, 1999. *ApJ*, 518:676–692.

M. Kishimoto, S. F. Hönig, R. Antonucci, et al., 2009a. *A&A*, 507:L57–L60.

M. Kishimoto, S. F. Hönig, R. Antonucci, et al., 2011a. *A&A*, 536:A78.

M. Kishimoto, S. F. Hönig, R. Antonucci, et al., 2011b. *A&A*, 527:A121.

M. Kishimoto, S. F. Hönig, K. R. W. Tristram, et al., 2009b. *A&A*, 493:L57–L60.

M. Köhler & A. Li, 2010. *MNRAS*, 406:L6–L10.

J. H. Krolik & M. C. Begelman, 1988. *ApJ*, 329:702–711.

A. Laor & B. T. Draine, 1993. *ApJ*, 402:441–468.

C. Leinert, U. Graser, F. Przygodda, et al., 2003. *Ap&SS*, 286:73–83.

N. A. Levenson, J. T. Radomski, C. Packham, et al., 2009. *ApJ*, 703:390–398.

N. A. Levenson, M. M. Sirocky, L. Hao, et al., 2007. *ApJ*, 654:L45–L48.

B. Lopez, P. Antonelli, S. Wolf, et al., 2008. In *Society of Photo-Optical Instrumentation Engineers (SPIE) Conference Series*, volume 7013 of *Society of Photo-Optical Instrumentation Engineers (SPIE) Conference Series*.

B. Lopez, S. Lagarde, W. Jaffe, et al., 2014. *The Messenger*, 157:5–12.

N. López-Gonzaga, L. Burtscher, K. R. W. Tristram, et al., 2016. *ArXiv e-prints*.

N. López-Gonzaga, W. Jaffe, L. Burtscher, et al., 2014. *A&A*, 565:A71.

D. Lutz, R. Maiolino, H. W. W. Spoon, et al., 2004. *A&A*, 418:465–473.

V. Manske, T. Henning, & A. B. Men'shchikov, 1998. *A&A*, 331:52–60.

D. Maoz, 2007. *MNRAS*, 377:1696–1710.

F. Marin, 2014. *MNRAS*, 441:551–564.

A. Marinucci, S. Bianchi, G. Matt, et al., 2016. *MNRAS*, 456:L94–L98.

A. G. Markowitz, M. Krumpe, & R. Nikutta, 2014. *MNRAS*, 439:1403–1458.

R. E. Mason, E. Lopez-Rodriguez, C. Packham, et al., 2012. *AJ*, 144:11.

S. Mateos, F. J. Carrera, A. Alonso-Herrero, et al., 2016. *ArXiv e-prints*.

J. S. Mathis, W. Rumpl, & K. H. Nordsieck, 1977. *ApJ*, 217:425–433.

G. Matt, A. C. Fabian, M. Guainazzi, et al., 2000. *MNRAS*, 318:173–179.

G. Matt, M. Guainazzi, F. Frontera, et al., 1997. *A&A*, 325:L13–L16.

T. A. Matthews & A. R. Sandage, 1963. *ApJ*, 138:30.

K. Meisenheimer, K. R. W. Tristram, W. Jaffe, et al., 2007. *A&A*, 471:453–465.

J. S. Miller, R. W. Goodrich, & W. G. Mathews, 1991. *ApJ*, 378:47–64.

R. Mor, H. Netzer, & M. Elitzur, 2009. *ApJ*, 705:298–313.

A. Müller, J.-U. Pott, S. Morel, et al., 2010. In *Society of Photo-Optical Instrumentation Engineers (SPIE) Conference Series*, volume 7734 of *Society of Photo-Optical Instrumentation Engineers (SPIE) Conference Series*.

F. Müller Sánchez, R. I. Davies, R. Genzel, et al., 2009. *ApJ*, 691:749–759.

F. Müller-Sánchez, M. A. Prieto, E. K. S. Hicks, et al., 2011. *ApJ*, 739:69.

C. G. Mundell, P. Ferruit, N. Nagar, et al., 2009. *ApJ*, 703:802–815.

C. G. Mundell, A. S. Wilson, J. S. Ulvestad, et al., 2000. *ApJ*, 529:816–831.

H. Mutschke, B. Begemann, J. Dorschner, et al., 1998. *A&A*, 333:188–198.

M. Nenkova, Ž. Ivezić, & M. Elitzur, 2002. *ApJ*, 570:L9–L12.

M. Nenkova, M. M. Sirocky, Ž. Ivezić, et al., 2008a. *ApJ*, 685:147–159.

M. Nenkova, M. M. Sirocky, R. Nikutta, et al., 2008b. *ApJ*, 685:160–180.

D. A. Neufeld, P. R. Maloney, & S. Conger, 1994. *ApJ*, 436:L127.

G. Neugebauer, J. B. Oke, E. E. Becklin, et al., 1979. *ApJ*, 230:79–94.

R. Nikutta, M. Elitzur, & M. Lacy, 2009. *ApJ*, 707:1550.

M. Orienti & M. A. Prieto, 2010. *MNRAS*, 401:2599–2610.

C. Packham, J. T. Radomski, P. F. Roche, et al., 2005. *ApJ*, 618:L17–L20.

E. A. Pier & J. H. Krolik, 1992. *ApJ*, 401:99–109.

E. A. Pier & J. H. Krolik, 1993. *ApJ*, 418:673.

A. Poncelet, C. Doucet, G. Perrin, et al., 2007. *A&A*, 472:823–831.

A. Poncelet, G. Perrin, & H. Sol, 2006. *A&A*, 450:483–494.

A. Poncelet, H. Sol, & G. Perrin, 2008. *A&A*, 481:305–317.

J.-U. Pott, A. Müller, I. Karovicova, et al., 2012. In *Society of Photo-Optical Instrumentation Engineers (SPIE) Conference Series*, volume 8445 of *Society of Photo-Optical Instrumentation Engineers (SPIE) Conference Series*.

D. Raban, B. Heijligers, H. Röttgering, et al., 2008. *A&A*, 484:341–345.

D. Raban, W. Jaffe, H. Röttgering, et al., 2009. *MNRAS*, 394:1325–1337.

J. T. Radomski, R. K. Piña, C. Packham, et al., 2003. *ApJ*, 587:117–122.

C. Ramos Almeida, N. A. Levenson, A. Alonso-Herrero, et al., 2011. *ApJ*, 731:92.

C. Ramos Almeida, N. A. Levenson, J. M. Rodríguez Espinosa, et al., 2009. *ApJ*, 702:1127–1149.

G. Reber, 1944. *ApJ*, 100:279.

J. Reunanen, M. A. Prieto, & R. Siebenmorgen, 2010. *MNRAS*, 402:879–894.

D. Rouan, F. Lacombe, E. Gendron, et al., 2004. *A&A*, 417:L1–L4.

D. Rouan, F. Rigaut, D. Alloin, et al., 1998. *A&A*, 339:687–692.

E. E. Salpeter, 1964. *ApJ*, 140:796–800.

D. B. Sanders, E. S. Phinney, G. Neugebauer, et al., 1989. *ApJ*, 347:29–51.

M. Schartmann, A. Burkert, M. Krause, et al., 2010. *MNRAS*, 403:1801–1811.

M. Schartmann, K. Meisenheimer, M. Camenzind, et al., 2005. *A&A*, 437:861–881.

M. Schartmann, K. Meisenheimer, M. Camenzind, et al., 2008. *A&A*, 482:67–80.

M. Schartmann, K. Meisenheimer, H. Klahr, et al., 2009. *MNRAS*, 393:759–773.

M. Schartmann, K. Wada, M. A. Prieto, et al., 2014. *MNRAS*, 445:3878–3891.

M. Schmidt, 1963. *Nature*, 197:1040.

M. Schweitzer, B. Groves, H. Netzer, et al., 2008. *ApJ*, 679:101–117.

C. K. Seyfert, 1943. *ApJ*, 97:28.

G. A. Shields, 1974. *ApJ*, 191:309–316.

R. Siebenmorgen, M. Haas, E. Pantin, et al., 2008. *A&A*, 488:83–90.

R. Siebenmorgen, F. Heymann, & A. Efstathiou, 2015. *ArXiv e-prints*.

M. M. Sirocky, N. A. Levenson, M. Elitzur, et al., 2008. *ApJ*, 678:729–743.

V. M. Slipher, 1917. *Proceedings of the American Philosophical Society*, 56:403–409.

L. Spitzer, Jr. & W. C. Saslaw, 1966. *ApJ*, 143:400.

M. Stalevski, J. Fritz, M. Baes, et al., 2012. *MNRAS*, 420:2756–2772.

D. Stern, 2015. *ApJ*, 807:129.

M. Suganuma, Y. Yoshii, Y. Kobayashi, et al., 2006. *ApJ*, 639:46–63.

O. G. Taranova & V. I. Shenavrin, 2006. *Astronomical and Astrophysical Transactions*, 25:233–237.

R. Terlevich & J. Melnick, 1985. *MNRAS*, 213:841–856.

D. Tomono, Y. Doi, T. Usuda, et al., 2001. *ApJ*, 557:637–645.

K. R. W. Tristram, L. Burtscher, W. Jaffe, et al., 2013. *ArXiv e-prints*.

K. R. W. Tristram, L. Burtscher, W. Jaffe, et al., 2014. *A&A*, 563:A82.

K. R. W. Tristram, K. Meisenheimer, W. Jaffe, et al., 2007. *A&A*, 474:837–850.

K. R. W. Tristram, D. Raban, K. Meisenheimer, et al., 2009. *A&A*, 502:67–84.

K. R. W. Tristram & M. Schartmann, 2011. *A&A*, 531:A99.

K. R. W. Tristram, M. Schartmann, L. Burtscher, et al., 2012. *Journal of Physics Conference Series*, 372(1):012035.

C. M. Urry & P. Padovani, 1995. *PASP*, 107:803.

G. van der Wolk, P. D. Barthel, R. F. Peletier, et al., 2010. *A&A*, 511:A64.

B. Vollmer, T. Beckert, & R. I. Davies, 2008. *A&A*, 491:441–453.

K. Wada, 2012. *ApJ*, 758:66.

J. Wang, G. Fabbiano, M. Karovska, et al., 2012. *ApJ*, 756:180.

G. Weigelt, K.-H. Hofmann, M. Kishimoto, et al., 2012. *A&A*, 541:L9.

G. Weigelt, M. Wittkowski, Y. Y. Balega, et al., 2004. *A&A*, 425:77–87.

A. S. Wilson & J. S. Ulvestad, 1983. *ApJ*, 275:8–14.

M. Wittkowski, P. Kervella, R. Arsenault, et al., 2004. *A&A*, 418:L39–L42.

L. Woltjer, 1959. *ApJ*, 130:38.

E. Xanthopoulos, A. H. C. Thean, A. Pedlar, et al., 2010. *MNRAS*, 404:1966–1983.

Y. B. Zel'dovich, 1964. *Soviet Physics Doklady*, 9:195.

C. Zier & P. L. Biermann, 2002. *A&A*, 396:91–108.

Samenvatting

In sommige sterrenstelsels, wordt het licht afkomstig uit miljarden sterren die samen een sterrenstelsel vormen overschaduwt door het licht uit het centrum. Het spectrum van het centrale gebied verschilt van het spectrum van sterren en de emissie is sterk op alle golflengten. Een sterrenstelsel waarvan het centrum een enorme hoeveelheid energie uitstraalt wordt een actieve sterrenstelsel genoemd en de kernen van actieve sterrenstelsels krijgen de naam van actieve galactische kernen (AGNs).

Het is al lang beseft dat de kern van een AGN uit een superzwaar zwart gat bestaat, van bijvoorbeeld 10^8 zonsmassa of meer, dat gas en stof aantrekt. Gas wervelt rond deze superzware zwarte gaten in een schijf, een zogenoemde accretieschijf, voordat het gas wordt opgeslokt. De gravitatie-energie die vrijgemaakt wordt tijdens de accretie op een zwart gat is een efficiënt proces voor het omzetten van materie tot energie. De meeste sterrenstelsels hebben in superzware zwarte gaten in hun centra, maar deze hoeven niet actief te zijn, wat bijvoorbeeld het geval is in onze Melkweg.

AGNs zijn ingedeeld in meerdere klassen, waarvan de belangrijkste zijn: 1) de Seyfert melkwegstelsels, die alhoewel ze een bescheiden lichtsterkte hebben, het best bestudeerd zijn omdat ze over het algemeen niet ver van ons vandaan zijn; 2) de quasars, die ontzetend helder zijn en bijzonder talrijk zijn op grote afstanden (roodverschuiving van ≈2). Ongeveer 10 % van de quasars hebben een sterke radiostraling, ook wel radio-luid genoemd, de rest zijn radio-rustig. De sterkte van de radiostraling wordt over het algemeen geassocieerd met een gecollimeerde relativistische uitstroom of een jet, of met regio's waar een jet interactie heeft met omringende materiaal. Tenslote zijn er de blazars die worden gezien als we recht in de jet van een actieve kern kijken.

Ondanks hun verschillen vertonen sommige AGNs ook gelijkenissen met elkaar. Om een eenvoudige uitleg van de diversiteit van waargenomen spectra voor AGNs vast te stellen, werd ongeveer 20 jaar geleden een standaard model voorgesteld. In dit model delen alle AGNs dezelfde eigenschappen. Dat betekent dat ze allemaal dezelfde verwarmingsmechanismes hebben maar hun waargenomen verschillen, zoals de aanwezigheid of afwezigheid van brede emissielijnen en UV/optische emissie, wordt bepaald door een verduisteringseffect.

Het stof is een van de belangrijkste onderdelen van de unificatietheorie van AGNs. In de striktste versie van deze theorie wordt de kern van een AGN omsingeld door een optisch dikke stoftorus en AGNs zijn in principe hetzelfde object maar waargenomen vanuit verschillende zichtlijnen. Wanneer de kern direct is waargenomen noemen we

ze type 1 objecten en als de nucleus geblokkeerd is door het stof noemen we ze type 2.

Direct bewijs voor de aanwezigheid van een stoftorus komt door waarnemingen in het infrarood. De UV, röntgen- en radiostraling komen rechtstreeks uit de centrale regio's rond het zwarte gat, maar het infrarode straling echter niet. Het optisch en UV licht van de accretieschijf wordt geabsorbeerd en vervolgens opnieuw uitgestraald door wolken van gas en stof die de centrale kern omringen.

Om de waargenomen infrarood continuüm emissie, spectroscopie en de infrarood-beelden van AGNs goed te kunnen interpreteren, hebben we een goed begrip nodig van de absorptie en emissie-eigenschappen van het kernomringende stof. De belang-rijkste factoren bij het begrijpen van de structuur en het aard van AGNs omvatten de bepaling van de geometrie van de nucleaire stoftorus en verduisteringseigenschap-pen van het kernomringende stof. Tevens wordt een nauwkeurige kennis vereist van de extinctie-eigenschappen van het stof om te kunnen corrigeren voor de stofsver-duistering en de intrinsieke optische/ultraviolet spectrum van de kern te kunnen reconstrueren en de fysieke omstandigheden van het stof dichtbij de kern te onthul-len.

Dit proefschrift

In dit proefschrift heb ik de nucleaire omgeving van actieve sterrenstelsels bestu-deerd door te onderzoeken wat de structuur is van de stofwolken rond een AGN. Wij profiteren van de relevante informatie verkregen via de infrarood interferometrische waarnemingen om de geometrie en de eigenschappen van de stoffige omgeving te ver-kennen. Door het analyseren van hoge resolutie infrarood waarnemingen hebben we de stofgeometrie, samenstelling en temperatuurprofiel bepaald. Hier volgt een korte samenvatting van de inhoud van elke hoofdstuk in dit proefschrift.

In **hoofdstuk 2** gebruiken we mid-infrarood interferometrische waarnemingen om de grootschalige $(5-10\,\text{pc})$ geometrie van de nucleaire stoffige omgeving te bepalen en een verbinding tussen de binnenste hete schijf en de externe omgeving te vinden. De analyse is gebaseerd op een grote hoeveelheid interferometrische metingen van het sterrenstelsel NGC 1068 die verkregen zijn met behulp van de Very Large Telescope Interferometer op Paranal en het instrument MIDI . We analyseren en modelleren de interferometrische metingen zorgvuldig en reconstrueren een model van de nucle-aire infrarode omgeving. We vinden dat de infraroodstraling sterk asymmetrisch is en dat ongeveer $60-70\,\%$ van de $12\,\mu\text{m}$ emissie afkomstig is van een grote diffuse component dichtbij de wanden van de ionisatiekegel. In tegenstelling tot de huidige modellen, waarin de hoogste percentage van de emissie het schijfachtige structuur van de klassieke torus moet traceren, is een groot deel van de nucleaire infrarode

emissie van NGC 1068 niet afkomstig uit de equatoriale omgeving.

In **hoofdstuk 3** analyseren we mid-infrarood interferometrische waarnemingen van 23 objecten om te onderzoeken of er polaire emissie aanwezig is. Vorige studies van individueel waargenomen objecten, zoals NGC 1068 en Circinus, hebben laten zien dat er nucleaire polaire emissie aanwezig is in plaats van de verwachte equatoriale emissie geproduceerd door een torusachtig object. We onderzoeken ons vermogen om langgerekte vormen te identificeren ten opzichte van de (u, v) dekking en de kwaliteit van onze waarnemingen. Vanwege de inhomogeniteit van de interferometrische waarnemingen, hebben wij alleen langgerekte vormen geïdentificeerd in vijf Seyfert objecten en vrijwel cirkelvormige emissie in twee andere objecten. In de langwerpige objecten is de hoofd-as altijd dichterbij de pool-as dan de equatoriale-as. Een langgerekte polaire emissie steunt het idee van een stoffige windomgeving in plaats van de klassieke torusachtige structuur.

In **hoofdstuk 4** presenteren we een statistische analyse van een steekproef van AGN met als doel om meer te leren over de algemene eigenschappen van hun nucleaire stoffige omgeving. Mid-infrarood interferometrische waarnemingen verkregen met het instrument MIDI missen de ware fase-informatie. Zonder de fase-informatie is het moeilijk of zelfs onmogelijk om beeldreconstructietechnieken toe te passen. Als alternatief, gebruiken we de beelden uit 3-dimensionale torusmodellen om informatie over de stoffige omgeving te extraheren. We zien dat de verschillen in type 1 en 2 objecten te complex zijn om alleen aan verduisteringseffecten of statistische variaties van de wolken toe te wijzen. In plaats daarvan zijn we wel in staat om elke Seyfert type afzonderlijk te verklaren. Het grootste verschil tussen beide ligt in de fractie van het volume ingenomen door het stof. Onze bevindingen suggereren dat tenminste twee mogelijke families van type 1 objecten bestaan, hoewel een continue overgang tussen verschillende type 1 objecten ook mogelijk is.

In **hoofdstuk 5** analyseren we in detail de mid-infrarode emissie van stofwolken om meer te leren over de rol van de optische dikte, de relatieve locatie van de wolken en de verduisteringseffecten. Door het analyseren van het mid-infrarood spectraalindex $(8 - 12{,}5\,\mu\text{m})$ en de pieksterkte van het silicaatemissie kunnen we een verklaring geven voor de waargenomen verschillen in type 1 AGNs. We vinden een verband tussen de spectraalindex en de gemiddelde ligging van de wolken. Onze resultaten suggereren dat de waargenomen verschillen in type 1 spectra worden veroorzaakt door variaties in de verdeling van de wolken.

In **hoofdstuk 6** onderzoeken we of er een signaal in het infrarode emissie geproduceerd wordt als gevolg van een recente variabiliteit van een röntgenbron in de kern van NGC 1068. De mid-infrarood interferometrische signalen waargenomen voor en tijdens de röntgenbron variantie vertoonden geen duidelijke veranderingen. Dit suggereert dat de mid-infrarood omgeving van NGC 1068 geen veranderingen ondervonden heeft in de laatste tien jaar en dat de röntgenbron variatie gezien door *NuStar* metingen uitgelegd kan worden door het doordringen van röntgenstraling door de stofwolken.

RESUMEN

La emisión producida en la región central de algunas galaxias excede la emisión total de las miles de millones de estrellas que conforman dicha galaxia. El espectro observado de dichas regions centrales, cuyo tamaño es de unos cuantos parsecs, es diferente al espectro que típicamente se observa en las estrellas y la emisión es muy brillante en todas las longitudes de onda. A las galaxias cuya región central emite una cantidad extremadamente alta de energía se les denomina Galaxias activas y las regiones centrales de dichas galaxias activas son llamados núcleos activos de galaxias (AGNs por sus siglas en ingles).

Los núcleos de los AGNs están conformados por un agujero negro supermasivo, con masas típicas del orden de 10^8 masas solares, que acreta gas y polvo. El gas circula en forma de espiral alrededor del agujero negro formando un disco, denominado disco de acreción, antes de que el gas sea tragado por el agujero negro. El mecanismo de acreción en un agujero negro es un proceso eficiente para convertir la materia en energía. La mayoría de las galaxias tienen un agujero negro supermasivo en sus centros pero este no necesariamente tiene que estar activo, como sucede en nuestra Via Lactea.

Los núcleos activos de galaxias estan divididos en diferentes clases, de los cuales los mas relevantes son: 1) Las galaxias Seyfert, que a pesar de tener luminosidades moderadas son las mejores estudiadas ya que éstas se encuentran relativamente cerca de nosotros; 2) Los cuásares tienen luminosidades muy altas y en general son mas abundantes a distancias lejanas, es decir, a corrimientos al rojo mayores a dos. Alrededor del 10 % de los cuásares muestran emisión prominente en radio, los cuales se denominan como objctos radio-fuertes, el resto son radio-debiles. La fuerza de la emisión en radio es por lo general asociada a el flujo relativista colimado o con regiones donde existe una interacción del jet con la materia que lo rodea. Finalmente, los blazares son AGNs cuyo jet apunta directamente al observador.

A pesar de sus diferencias algunos AGNs también muestran similitues entre sí. Hace aproximadamente unos 20 años se propuso un esquema de unificación con el fin de encontrar una explicación simple a la diversidad de los espectros observados de los AGNs. En dicho esquema todos los AGNs comparten las mismas propiedades. Esto significa que todos deben tener el mismo mecanismo de calentamiento pero las diferencias observadas, tales como la presencia o ausencia de líneas anchas de emisión o la emisión continua en el óptico y ultravioleta, son atribuidas a un efecto de inclinación.

El polvo es uno de los principales componentes dentro de la teoría de la unificación de los AGNs. En la versión más estricta de ésta teoría, la región nuclear de un AGN está rodeada por un toro de polvo ópticamente grueso. Este toro determina el tipo de AGN dependiendo de la linea de visión por donde se observa. Los objetos tipo 1 se denominan si el núcleo se observa directamente y objetos tipo 2 si el núcleo es bloqueado por el polvo.

Evidencia directa de la existencia de éste toro de polvo proviene de las observaciones en el infrarrojo. La emisión de altas energías y la emisión en radio proviene directamente de las regiones centrales que rodean al agujero negro pero la emisión en el infrarrojo es generada de manera indirecta. La emisión óptica y ultravioleta producida por el disco de acreción es absorbida y subsecuentemente emitida por las nubes de gas y polvo que rodean al disco de acreción.

Para poder interpretar de mejor manera la emisión continua en el infrarrojo, la información proporcionada por la espectroscopía y las imagenes en el infrarrojo de los AGNs, necesitamos tener un buen conocimiento de los mecanismos de absorción y emisión del polvo. Los factores determinantes para el entendimiento de la estructura y el origen de los AGNs incluyen la determinación de la geometría del toro y las propiedades de extinción del polvo. También es necesario tener un conocimiento exacto de las propiedades de extinción del polvo para poder efectuar una corrección del oscurecimiento ocasionado por el polvo con el fin de reconstruir el espectro óptico y ultravioleta intrínseco del núcleo y poder determinar las condiciones físicas del ambiente cercano al núcleo.

Éste trabajo

En ésta tesis he estudiado el entorno nuclear de galaxias activas al investigar la estructura del las nubes de polvo que rodean al AGN. Para esto hemos aprovechado la información proporcionada por las observaciones interferométricas en el infrarrojo para explorar la geometría y las propiedades de la región con polvo. Mediante el análisis de las observaciones infrarrojas de alta resolución angular hemos determinado la geometría de la estructura de polvo, composición química y el perfil de temperatura. Acontinuación presentamos un breve resumen del contenido de cada capítulo.

En el **capítulo 2** utilizamos observaciones interferométricas en el infrarrojo medio para develar la geometría a grandes escalas ($5-10$ pc) del ambiente nuclear conformado por el polvo con el fin de encontrar una conexión entre el disco interior caliente y el medio que lo rodea. El análisis ésta basado en una gran cantidad de mediciones interferométricas de la galaxia NGC 1068 obtenidas utilizando el Interferómetro del Very Large Telescope en el Observatorio de Paranal y el instrumento MIDI. En éste

capítulo analizamos y modelamos las mediciones interferométricas cuidadosamente y reconstruimos una imagen de la región nuclear en el infrarrojo. Encontramos que la emisión infrarroja es altamente asimétrica y que alrededor del $60-70\,\%$ de la emisión en $12\,\mu$m proviene de una gran componente difusa situada a lo largo de las paredes del cono de ionización. A diferencia de los modelos actuales, en los cuales la mayor parte de la emisión en el infrarrojo proviene de una estructura en forma de disco la cual traza el clásico toro de polvo, en NGC 1068 la mayor parte de la emisión infrarroja nuclear no contribuye a la emisión ecuatorial.

En el **capítulo 3** analizamos observaciones interferométricas en el infrarrojo medio de 23 objetos con el fin de investigar si la emisión polar está presente en dichos objetos. Previos estudios de objetos individuales, tales como NGC 1068 y la galaxia Circinus, han mostrado la existencia de emisión nuclear polar en lugar de la emisión ecuatorial producida por una estructura toroidal. En este capítulo investigamos nuestra capacidad para identificar formas elongadas en función de la cobertura del plano (u, v) y la calidad de nuestras observaciones. Debido a la inhomogéneidad de las mediciones interferométricas sólo hemos podido identificar formas elongadas en cinco objetos Seyfert y emisión casi circular en otros dos objectos. En los objetos elongados, la dirección del eje mayor se encuentra por lo general más cerca del eje polar que del eje ecuatorial. Una emisión polarmente elongada apoya la idea de en los AGNs exista un viento de polvo en lugar de la estructura toroidal clásica.

En el **capítulo 4** se presenta un análisis estadístico de una muestra de AGNs con el objetivo de incrementar nuestro conocimiento sobre las propiedades generales del ambiente nuclear conformado por el polvo. Observaciones interferométricas en el infrarrojo medio obtenidas con el instrumento MIDI carecen de información acerca de la fase del número complejo. Sin información sobre la fase es difícil o incluso imposible aplicar técnicas de reconstrucción de imágenes. Como alternativa, utilizamos imágenes producidas a partir de modelos tridimensionales del toro de polvo con el fin de recuperar información sobre el ambiente nuclear. Hemos encontrado que las diferencias en objetos tipo 1 y tipo 2 son demasiado complejas para poder ser atribuidas unicamente a efectos de inclinación o variaciones estadísticas de las nubes. Sin embargo, hemos sido capaces de explicar cada tipo Seyfert por separado. La mayor diferencia entre los dos tipos se encuentra en la fracción de volumen ocupado por el polvo. Nuestros hallazgos sugieren que se necesitan al menos dos posibles familias de objetos tipo 1, aunque no podemos descartar que exista una transición continua entre dichos objetos.

En el **capítulo 5** analizamos en detalle la emisión en el infrarrojo medio de las nubes de polvo con el fin de aprender más sobre la relevancia del espesor óptico, la

ubicación relativa de las nubes y la inclinación con respecto al observador. Al analizar el índice espectral del infrarrojo medio ($8-12.5\,\mu$m) y la amplitud del pico de emisión de los silicatos hemos sido capaces de proporcionar una explicación para las diferencias observadas en los objetos tipo 1. Encontramos que existe una correlación entre el índice espectral y la ubicación media de las nubes. Nuestros resultados sugieren que las diferencias observadas en los espectros de objetos tipo 1 son causadas por las variaciones en la distribución de las nubes.

Finalmente, en el **capítulo 6** investigamos la existencia de alguna señal en el infrarrojo producida como consecuencia de un evento reciente de variabilidad en los rayos X proveniente de la región nuclear de NGC 1068. Las señales interferométricas en el infrarrojo medio observadas antes y durante las variaciones de rayos X no muestran cambios claros. Esto sugiere que el entorno del infrarrojo medio de NGC 1068 se ha mantenido constante durante los últimos 10 años. Nuestras mediciones interferométricas apoyan la idea de que la variación de rayos X, detectada por *NuSTAR*, es debido al escape de los rayos X a través de las nubes que conforman la región nuclear.

Curriculum vitæ

"No estudio por saber más, sino por ignorar menos."
"I don't study to know more, but to ignore less."
— Sor Juana Ines de la Cruz

I was born on July 11, 1986 in Nezahualcoyotl, Estado de México, in México. In 1998, we moved to Wageningen, The Netherlands where I attended middle school and part of high school. After almost five years in The Netherlands, we returned to México where I completed high school.

In 2009, I graduated with a Bachelor's degree in Physics from the Universidad Nacional Autonoma de México (UNAM). After graduation, I began my Master's degree in Astronomy at UNAM with Dr. William H. Lee Alardin. During my time there, I did research in theoretical Astrophysics, specifically on the study of the dynamics of accretion disc around compact objects. I completed my Master's thesis, "Dynamics of accretion disks: Effects of self-gravity and viscosity" in 2011 and graduated with honors.

In November 2011, I moved to The Netherlands and began my doctoral research at Leiden Observatory, working with Prof. dr. Walter Jaffe. My project gave me the opportunity to work with the Very Large Telescope at Paranal Observatory in Chili, where I participated in the acquisition of observations using the infrared interferometric instrument MIDI. My thesis work has focused on analyzing and modeling infrared interferometric data of Active galactic nuclei. During my PhD, I presented my work at international conferences in the Netherlands, Belgium, France, Germany, the United Kingdom, and the United States.

Published

- Revealing the large nuclear dust structures in NGC 1068 with MIDI/VLTI
  López-Gonzaga, N., *Jaffe, W., Burtscher, L., Tristram, K. R. W., & Meisenheimer, K. 2014, A&A, 565, A71*

- Mid-infrared interferometry of Seyfert Galaxies: Challenging the Standard Model
  López-Gonzaga, N. *& Jaffe, W. 2015, A&A, in press*

- Mid-infrared interferometry of 23 AGN tori: On the significance of polar-elongated emission
  López-Gonzaga, N., *Burtscher, L., Tristram, K. R. W., Meisenheimer, K. & Schartmann, M. 2016, A&A, in press*

Submitted

- The dormant mid-infrared environment of the Seyfert Type II NGC1068
  López-Gonzaga, N., *Bauer, F., Tristram, K. R. W., Asmus, D., Burtscher, L., Marinucci, A., Matt, G., Stern, D. & Harrison, F. A. 2016, submitted to A&A*

In preparation

- Properties of the dusty clouds of AGNs
  López-Gonzaga, N., *Jaffe, W. & Schartmann, M., in prep*

Acknowledgements

"And in the end, it's not the years in your life that count.
It's the life in your years."
— Abraham Lincoln

It has been an honor for me to had the opportunity to work at Leiden Observatory for the last four and a half years. I feel very lucky to have come to The Netherlands, but more lucky to have met great persons. This thesis would not have been possible without the guidance, help and encouragement of many people and therefore I would like to write a few words to express my gratitude to them.

I would like to thank all my co-authors and close collaborators who have provided me with helpful comments and brought new ideas to improve my thesis. Klaus, Konrad and Marc, it was always a pleasure to work with you and you substantially contributed to the work presented here. Leonard, your support, help, and ideas were fundamental to this thesis and its completion. I am very thankful for all the talks that we had and I appreciate all the times that you took parts of your weekends to discuss and read my drafts. I learned a lot working along your side and I hope we have more collaborations in the future. To all the members of the MIDI Science group thanks a lot for the feedback and interesting questions. Xander, your suggestions, guidance and motivation were of great help to finish the thesis. Thank you for keeping me in the right path.

I would like to acknowledgement CONACyT for all the support they have provided me during my master and PhD, without them my career in science would not have been possible.

Susana, I would like to thank you for supporting and encouraging me during our stay in The Netherlands. Without your constant love and support I would have not been able to succeed in completing this thesis. Your personality, courage and commitment are admirable. You have been my source of inspiration during all these years.

My parents are the greatest example that I have in my life. I have always looked up to their accomplishments and aimed to match them. Thank you for introducing me to the world of science and for helping me to reach all my goals. I owe a huge debt of gratitude to them. Sacni and Aaron, thank you for always being ready to

help me. You are always present in my thoughts and I am lucky to have such a great sister and brother. Thank you to my grandparents for all their love and for teaching me the value of hard work. To my in-laws, who gave me a warm welcome since I met them. I know it was not easy for them to see Susana leave and so I am grateful for their motivation and thoughts.

A big thanks to all the people at the Leiden Observatory for making it a unique and multicultural professional environment. The observatory in Leiden will always have a special significance for me. Tjarda and Carmen, you were the first two persons that I met at the observatory and our friendship has grown much since then. I am very happy to have shared many important moments together and I am sure we will share even more in the future. It is an honor for me to have you as my paranymphs. Lucie, thank you for always being such a nice person with us and for motivating us to do new things. I will always remember the excellent dinners that you organized. Guilherme, it was always great to have a chat with you and I learned a lot from you during your stay in Leiden. I am very happy we met you. Thank you to my office mates over the years, Julia, Willem, Mayuresh, Alex, Dan. It was great to talk to you and I wish you all the best in your future.

My stay in The Netherlands would not have been as great as it was without all the amazing persons that I met. Davide, Simona, Jose, Martha, Liliana, Ainil, Yuri, Emilio, Silvia, Paula, Edwin, Tjibaria, Gráinne, Santiago, Alan, Heather, Marco, Matia, Irene, Alex, Thomas, Carl, Tiffany, and Kateryna, I am very thankful for all the great chats and reunions that we had. Over the past years, I had the pleasure of getting to know some wonderful people, both in and out of the university. Thanks to my non-astronomer friends Rosa, Marlen, Jeroen, Ysabel, Jessica, Alexandra, Fred, Angela, Sven, Marlene, Wouter for all the wonderful times that we spend together.

A special thanks to Alexa Jaffe-Klusman for opening the doors of her house to us. We will always remember the first Dutch New year that we spend together. We enjoyed all the times that we had dinner together and we are very thankful for providing us with one very important Mexican tool, *el molcajete*. Virginia, you have been a wonderful person with us and I am thankful for all your support. Thank you for reading and correcting my thesis. Karen and Luis, I am very thankful to you for supporting me during my first months in The Netherlands.

My gratitude to all my advisors, friends and teachers from the past, who continue to have a strong impact on me.